FLUORESCENCE-FORCE SPECTROSCOPY AT THE SINGLE MOLECULE LEVEL

BY

RUOBO ZHOU

DISSERTATION

Submitted in partial fulfillment of the requirements
for the degree of Doctor of Philosophy in Physics
in the Graduate College of the
University of Illinois at Urbana-Champaign, 2012

Urbana, Illinois

Doctoral Committee:

Assistant Professor Aleksei Aksimentiev, Chair
Professor Taekjip Ha, Director of Research
Professor Paul Selvin
Professor John D Stack

Abstract

During the past decade, various powerful single-molecule techniques have evolved and helped to address important questions in life sciences. As the single molecule techniques become mature, there is increasingly pressing need to maximize the information content of the analysis in order to be able to study more complex systems that better approximate *in-vivo* conditions. Here, we develop a fluorescence-force spectroscopy method to combine single-molecule fluorescence spectroscopy with optical tweezers. Optical tweezers are used to manipulate and observe mechanical properties on the nanometer scale and piconewton force range. However, once the force range is in the low piconewton range or less, the spatial resolution of optical tweezers decreases significantly. In combination with fluorescence spectroscopy, like single molecule Förster (or fluorescence) resonance energy transfer (FRET) whose detectable distance range is approximately 3-10 nm, we are able to observe nanometer fluctuations and internal conformational changes in a low-force regime. The possibility to place fluorescent labels at nearly any desired position and a sophisticated design of the experiment increases the amount of information that can be extracted in contrast to pure mechanical or fluorescence experiments. We demonstrate the applications of this method to various biological systems including: 1) to measure the effect of very low forces on the nanometer scale conformational transitions of the DNA four-way (Holliday) junction; 2) to dissect protein diffusion and dissociation mechanisms on single stranded DNA, 3) to calibrate FRET-based *in-vivo* force sensors and 4) to study mechanical unfolding of single proteins. The results could not have been obtained with fluorescence or force measurement alone, and clearly demonstrates the power and generality of our approach. Finally, we show that self-quenching of two identical fluorophores can be used to detect small conformational dynamics corresponding to sub-nanometer distance changes of single molecules in a FRET-insensitive short range (< 3 nm), extending the detectable distance range of our fluorescence-force spectroscopy method.

To my family

Acknowledgements

I would like to thank my advisor, Taekjip Ha for his guidance throughout my graduate study. His creativity, profound insight, and endless enthusiasm for scientific research were inspirational.

I would also like to thank Professors Aleksei Aksimentiev, Paul Selvin, and John Stack for serving on my committee, and offering constructive criticism and comments.

Sungchul Hohng trained me to independently carry out single-molecule experiments. Chirlmin Joo, Rahul Roy, Hamza Balci and Michelle Nahas helped me with experiments when I started my first research project in the lab. Michael Brenner synthesized several constructs to make stretching peptides/proteins using fluorescence-force spectroscopy possible.

Reza Vafabakhsh, Jiajie Diao, Gwangrog Lee, Michael Schlierf, Hye Ran Koh, Hajin Kim, Matt Comstock, Jeehae Park, Kyung Suk Lee, Prakrit Jena, Sinan Arslan and Ankur Jain were wonderful labmates and constant sources of technical assistance and valuable discussions. Sua Myong, Salman Syed, Xinghua Shi, Jaya Yodh, Cheng Liu, Ibrahim Cisse Seongjin Park, Sultan Doganay, Jungmin Joo, Seongjin Park and Burak Okumus, Peter Cornish, Tae-Young Yoon, Maria Sorokina, Eli Rothenberg, Yuji Ishitsuka and Benjamin Leslie have energized the lab and my spirits all the time.

Jichuan Zhang, Jingyi Fei, Thuy Ngo, Xuefeng Wang, Lanying Zeng, Kyu Young Han, James Adrian, Christopher Thibodeaux and Divya Srinivasan have been inspirational newcomers to our lab.

I heartily thank Alexander Kozlov, Timothy Lohman, Sergey Korolev, Simone Kunzelmann, Martin Webb, Jin Inoue, Tsutomu Mikawa, James Keck, Anne-Cecile Declais, Alasdair Freeman and David Lilley who have been excellent collaborators and enjoyable to work with.

Finally, I thank all my friends and family members in helping me achieve success and fulfilling my dreams.

Table of Contents

Chapter 1
Introduction

1.1 Single Molecule Fluorescence and FRET

1.1.1 Fluorescence and Jablonski Diagram

As the rapid development of various fluorescence molecules (or fluorephores) and new fluorescence techniques, fluorescence microscopy has become the mainstream method in biology to directly observe the biomolecules functioning in variety of biological processes. The fudenmental principle of fluorescence can be described in a Jablonski diagram (Figure 1.1A) [1]. After the molecule absorbs a photon of certain wavelengths supplied by an external source (for example, a laser), its electronic energy state changes from a singlet ground state (S_0) to an excited electronic singlet state (S_1). Within the S_0 or S_1 state, there are multiple of vibrational energy levels with Line G representing the lowest energy state and thin lines 1 to 3 representing the higher energy state. The absorbed photon should have an energy that corresponds to the energy difference between the S_0 state and the S_1 state of the molecule. The absorbance occurs very quickly and on the order of 10^{-15} seconds. Once the absorption is accomplished, the most likely pathway for the molecule to dissipate the energy and return to the ground state is first to relax to the lowest vibrational energy level of the S_1 state through a non-radiative process known as internal conversion, taking typically on the order of 10^{-14} -10^{-11} seconds. From there, the molecule can emit a photon and relax to a S_0 state (10^{-9}-10^{-7} seconds), immediately after which it eventually relaxes to the lowest energy state of the S_0 state through internal conversion. The energy lost during internal conversion process results in an emitted photon with lower energy than that of the absorbed photon, leading to a red-shifted spectrum for the emission compared to the absorption spectrum of the molecule (referred to as the Stokes shift [2]).

Another pathway for the molecule to return to the ground state is through intersystem crossing, converting the molecule from the excited singlet state (S_1) to an excited triplet state (T_1). This requires the electron to change its spin multiplicity which is weakly allowed and takes 10^{-8}-10^{-3} seconds. Once in the T_1 state, the molecule may either relax to the ground state by a radiative process (called phosphorescence; Figure 1.1A) or a non-radiative process (such as collisional quenching, and fluorescence resonance engergy transfer as we discuss in the next section; Figure 1.1B).

1.1.2 Förster (or Fluorescence) Resonance Energy Transfer (FRET)

Förster (or Fluorescence) Resonance Energy Transfer (FRET) is a non-radiative energy transfer from an electronic excited energy state of a fluorescent molecule (termed donor) to another neighboring fluorescent molecule (termed acceptor) via a dipole-dipole interaction, converting the acceptor molecule to its excited energy state such that the acceptor can emit fluorescence (Figure 1.1B) [3-5]. The extent of energy transfer depends on the separation distance between the donor and the acceptor, the spectral overlap between the donor emission and acceptor absorption and the relative orientation of the donor and acceptor dipoles. FRET efficiency, *E*, is a measure of how much the energy transferred from the donor to the acceptor (Figure 1.2) and is given by

$$E = \frac{1}{1 + \left(\frac{R}{R_0}\right)^6} \qquad (1.1)$$

where R is the separation between the donor and the acceptor, and R_0 is known as Förster radius which is a constant for a set of FRET pair under identical conditions and is given by

$$R_0 = \left[(8.785 \times 10^{17})\Phi^D \kappa^2 n^{-4} J(\upsilon)\right]^{\frac{1}{6}} \quad nm \qquad (1.2)$$

where Φ^D is the donor quantum yield in the absence of the acceptor, n is the refractive index of the medium and κ is the orientation factor for the dipole-dipole interaction. κ^2 ranges between 0 (when dipoles are perpendicular) to 4 (when the dipoles are aligned) and is estimated to be 2/3 for a pair of freely rotating dipoles. $J(\nu)$ is the integral of the spectral overlap between the donor emission and the acceptor absorption.

1.1.3 Single Molecule Fluorescence and Single Molecule FRET

In the past two decades, fluorescence techniques have been extended to observe biological processes at the single molecule level under biologically relevant conditions.

These single molecule studies involve detecting structural and conformational changes of the proteins or nucleic acids and investigating the protein-nucleic acid interactions by using the fluorescence localization; fluorescence quenching; polarization response; and FRET [6,7]. In contrast to conventional ensemble methods, single-molecule methods can look at a biological system when it is out of equilibrium and hence allow us to explore the heterogeneity among molecules and detect the transition and intermediate states which are otherwise hidden in ensemble measurements [8,9].

Although conventional fluorescence microscopy and other imaging methods have been used to observe biological processes, there is a light diffraction limit which is about half wavelength of the visible light itself (several hundreds of nanometers). However, the size of a biomolecule is typically about several nanometers. To push the spatial resolution limit so that we can observe the motion or the structure dynamics of a single biomolecule, single molecule FRET (smFRET) detection was first achieved in 1996 [10] and later became a mainstream technique in the biology field because of its ability to detect the conformational change of individual molecules or mutual interactions in the nanometer distance range at the single molecule level.

Organic fluorophores (such as Cyanine and Alexa fluorophores) are typically utilized in the smFRET experiments, because they are typically bright, small-sized, water-soluble, easily conjugated to proteins and/or nucleic acids and possess stable photo-physical characteristics. In this thesis, two FRET pairs were selected in all the experiments presented: 1) Cy3(donor)-Cy5(acceptor) pair and 2) Alexa555(donor)-Cy5(acceptor) pair. Cy3 and Alexa555 can both be excited by a 532nm solid-state laser and emit fluorescence (emission peak at ~ 570 nm). When in close proximity to Cy3 or Alexa555, Cy5 can emit fluorescence through FRET. In practice, estimated FRET efficiency, E, can be calculated by,

$$E = \frac{I_A}{I_A + I_D} \qquad (1.3)$$

where I_A and I_D are the emission intensities of the acceptor and the donor respectively.

Many previous reviews have intensively described the instrumentation by which one can perform a single molecule FRET experiment [9,11,12]. Briefly, there are two kinds of commonly used microscopy for single molecule FRET experiments: 1) Confocol microscopy and 2) Total internal reflection (TIR) microscopy (Figure 1.3). In confocal microscopy, the excitation laser beam (532 nm laser in our case) is focused onto the coverslip surface where the fluorescently labeled biomolecules are immobilized. A sample chamber consists of a microscope coverslip and a microscope slide and is filled with an imaging buffer that mimics the biologically relevant conditions. A 100-µm pinhole is placed in the detection path to eliminate out-of-focus signal. The Cy3 and Cy5 signals were split and collected by two avalance photodiodes (APDs). Only one point (a few hundred nanometers in focus diameter) on the sample plane is imaged at one time. Therefore, to obtain a sample image containing multiple biomolecules, a peizo stage is used to raster scan the sample in the x-y plane (Figure 1.3A). In TIR microscopy, the excitation is achieved by total internal reflection of the excitation light at the slide-buffer interface (Figure 1.3B). The fluorescently labeled biomolecules are immobilized on the slide surface inside the sample chamber and are exposed to the evanescence field (~a few hundred nanometers in depth) induced by TIR to produce fluorescence. An electron multiplying charged couple device (EM-CCD) is used for imaging. A slide area (75 µm × 75 µm) can be imaged onto a 8.2 mm × 8.2 mm CCD chip at one time. Cy3 and Cy5 signals from a same slide area (75 µm × 37 µm) are split and imaged side by side on the CCD (Figure 1.3B).

1.2 Optical Tweezers for Single Molecule Studies[*]

1.2.1 Introduction to Optical Tweezers

A dielectric bead whose size is typically in the range of ~ 0.2 – 5 µm was first found capable to be trapped by a gradient force near the focus of a high-power laser beam in 1986[13]. This technique is known as optical tweezers and has been widely employed in studying motor proteins[14-17], nucleic acid mechanics[18-20], DNA packing motors[21,22], protein folding and unfolding[23-25], protein-protein interaction[26], and protein-nucleic acid interaction[27-29] at the single-molecule level. To minimize heating of the sample and laser-induced damage to the biomolecule attached to the bead, a near-infrared wavelength (e.g.,

---

[*] The content in this section has been published as a paper:
Brenner, M. D., Zhou, R. & Ha, T. Forcing a connection: impacts of single-molecule force spectroscopy on in vivo tension sensing. *Biopolymers* **95**, 332-44 (2011).

830, 980, 1064 nm) laser is typically used [30]. In a typical optical tweezers experiment, the biomolecule (e.g., nucleic acids, proteins), or the biological complex of interest is tethered between a bead and a stiff surface through DNA handles. By gradually moving the surface away from the bead, mechanical tension is applied through the DNA handles to the biomolecule (or the biological complex). The bead trapped by optical tweezers usually serves as a Hookean spring and has a linear elasticity with a stiffness (k) ranging from 0.005 to 1 pN nm^{-1}. The stiffness of the optical trap depends on the laser power, the size of the bead and the change in refractive index between the bead and the aqueous medium, resulting in a typical accessible force range of 0.1-100 pN[31].The applied force (F) can be determined by $F = k\,x$, where x is the deflection of the bead from the trap center. For detecting the deviation of the bead from the center of the trapping laser beam, the scattered light from the bead is collected and sent onto a quadrant photodiode or a position-sensitive photodetector[30]. It has been shown directly by single molecule experiments that biochemical reactions can be influenced by applied force [32]. Not only can optical tweezers provide a manipulation tool to apply forces to a biomolecule, but it is also possible to detect the conformational dynamics of single biomolecules through the force spectroscopy. In recent years, optical tweezers have achieved angstrom spatial resolution (the magnitude of a single base-pair length of DNA) to follow the steps of biological motors moving on their track [33-35].

1.2.2 Other Single Molecule Force Methods

Besides optical tweezers, many other single-molecule force methods have been developed to probe the intermolecular forces generated by biomolecules through binding energies between individual ligand-receptor pairs and the response of biomolecules to applied mechanical tension during the past few decades. The most commonly used techniques for these purposes include glass microneedles, atomic force microscopy (AFM), the biomembrane force probe (BFP), magnetic tweezers, optical tweezers, and flow-induced stretching. In a typical single-molecule experiment, the biomolecule or the biological complex under investigation is tethered between a flexible force transducer and a stiff surface or substrate. By gradually moving the surface/substrate away from the force transducer, mechanical tension is applied through the tethers to the biomolecule(s), with the applied forces commonly determined by the recorded variation of the force transducer's position. Similarly, if the complex generates force between the two tethering points, the force can be detected by the force transducer. Similar to the trapped bead in optical tweezers, the force transducer usually serves as a Hookean spring and has a linear elasticity with a stiffness (k) ranging from 10^{-6} to10^{5} pN nm^{-1}. The force (F) can be determined by $F = k\,x$, where x represents the deflection of the transducer. A softer (less stiff) force transducer allows for higher sensitivity, meaning it can detect smaller forces. The typical, accessible force range with these techniques is 10^{-2}-10^{4} pN with an experimental time resolution ranging from 1-100 milliseconds [36-38], which is sufficient for biologically relevant studies with a variety of systems including, for example, DNA replication and recombination[39-41]. Various single-molecule force techniques utilize different types of force transducers, and these differences help in making these techniques complementary yet distinct in the types of biological systems each can address. While some of the single-molecule techniques discussed in the following sections have drawbacks such as being time-consuming and thus low-throughput, there is currently no other way to ascertain biomolecular forces *in vitro* that can be used as calibration for force determination in the cell at the single-molecule level [42].

1.2.2.1 Glass Microneedles

A biomolecule of interest can be attached between a soft glass microneedle and a stiff needle or surface, as shown in Figure 1.4A. If the soft needle (i.e., the force transducer) is thin enough , a stiffness of 10^{-3}-1 pN nm^{-1} can be achieved to detect molecular forces [37]. The stiff needle or surface is moved away from the soft needle, applying forces of 10-10^{3} pN. For determining the force applied, the soft needle is directly imaged to determine its deflection. This technique was first used to measure the sliding force between doublet microtubules in flagella,[43] and for measurement of bond disruption between two actin monomers in an actin filament as well as myosin migration force along actin filaments [44]. Alternatively, an optical fiber can act as the soft needle, and this approach was used to study the elasticity of single dsDNA molecules [45]. The light emitted from the end of the soft optical fiber is projected onto a position-sensitive photodetector which allows for precise determination of the force transducer's bending geometry.

1.2.2.2 Atomic Force Microscopy (AFM)

AFM replaces the soft glass needle with a flexible cantilever characterized by a stiffness range between 1-10^5 pN nm^{-1}.[37,38] A complete AFM probe consists of a cantilever with an attached sharp tip (nanometer in size) at its free end, and the biomolecule of interest is attached between the tip and a stiff surface (Figure 1.4B). Forces between ~5 and 10^3 pN can be applied to the biomolecule by moving the stiff surface with a piezoelectric stage. For force calibration, a laser beam is reflected off the back plane of the cantilever onto a position-sensitive photodetector for determination of cantilever deflection by forces applied through the tip. AFM was hereby employed to stretch individual biomolecules including chromatin fibers [46], proteins [47,48],nucleic acids [46,49], and to elegantly measure the energy landscape of ligand-receptor interactions[50]. Because the force required to break covalent bonds [51] is much larger than the binding force between ligands and receptors, researchers are able to covalently link ligands to the AFM tip and the cognate receptor to a stiff surface for measurement of the adhesion force between single ligand-receptor pairs [52,53]. The first single-molecule measurements of the ligand-receptor recognition force was performed for biotin- avidin pairs by AFM [54,55].

1.2.2.3 Biomembrane Force Probe (BFP)

The BFP technique is based on the micropipette aspiration (MPA) method originally developed to study the elastic properties of cell membranes and intercellular adhesion forces [56]. MPA was first used to study cell membrane elasticity by observing membrane tension as a function of the suction pressure applied by a micropipette (tip opening diameter: < 1 μm – 10 μm) in contact with the cell [57]. Evans and coworkers utilized a red blood cell (RBC) as the force transducer whose membrane stiffness is flexibly controllable by micropipette suction, and a functionalized bead can be chemically attached to the RBC as a surface probe (Figure 1.4C) to determine the distance between the bead and membrane surfaces from the interference fringe pattern between unscattered light and light scattered from the bead [58,59]. This combination of

RBC and bead composes the BFP. This method has been widely used to study the interactions between cell-surface receptors and its cognate ligands.[58] The ligands are on the surface of the bead attached to the RBC, and the receptors are on the surface of a vesicle. Both the RBC and vesicle are held by a glass micropipette. If the density of the ligands and receptors are low enough, the bond between a single ligand-receptor pair can be formed when the vesicle containing receptors is brought in contact with the bead covered with ligands. The interaction between a single ligand-receptor pair can be studied by then moving the vesicle away from the bead. A biomolecule or a biological complex can be attached between the BFP and a second bead or a vesicle, both of which are held by a micropipette. The forces exerted can be determined from the deformation of the RBC, typically ranging from 10^{-2} to 10^{3} pN. S.E. Chesla and coworkers developed this method to study the 2D receptor-ligand binding kinetics by measuring the adhesion probability depending on contact duration between receptor and ligand and surface density of the receptor/ligand.[60]

1.2.2.4 Magnetic Tweezers

Instead of trapping a bead by a gradient force near the focus of a laser, magnetic tweezers traps a bead in the magnetic field (Figure 1.4D). Pioneering work with magnetic tweezers involved the study of the elastic response of single dsDNA molecules[61], including stretching of nucleosomal DNA[62]. Magnetic field gradients generated by permanent magnets or electromagnets are used to exert forces between 10^{-3}–10^{2} pN on magnetic beads attached to biomolecules of interest[38]. The detectable forces are the smallest among all the force techniques (as small as 10^{-3} pN) because of a very soft force transducer (the magnetic bead) in magnetic tweeezers with the stiffness typically ranging between 10^{-3} -10^{-6} pN nm^{-1}. Another advantage in magnetic tweezers assays is the capability to apply torque to surface-tethered biomolecules due to the preferential orientation of the beads which rotate in the magnetic field. The torque applied by magnetic tweezers can generate supercoils in surface-tethered dsDNA[63] and extensions of the technique have included probing protein-nucleic acid interactions. Examples include the study of DNA uncoiling by a topoisomerase[64], DNA scrunching by a RNA polymerase during transcription[65], and DNA unzipping by DNA helicases[66,67].

1.2.2.5 Flow-Induced Stretching

Liquid flow has been a simple method for stretching long pieces of DNA attached at one end to a surface immobilized biomolecule and to a magnetic bead at the free end (Figure 1.4G) [61]. The scattered light from the bead is imaged using a darkfield microscope with a high-resolution charge-coupled device (CCD) camera at 0.5–2 Hz, and the flow-induced force exerted on the biomolecule through the DNA handle can be calculated from the mean-square displacement of the DNA-tethered bead [68]. One advantage of the method is high-throughput data acquisition, since observation of many simultaneously stretched biomolecules is possible. Van oijen and coworkers use this technique to study bacteriophage λ DNA digestion by λ exonuclease[69] and the mechanism of DNA synthesis at a replication fork [40].

1.3 Single Molecule Forces in Biology

1.3.1 Nucleic Acid Mechanics

As single-molecule force techniques mature, the simplest studies remain those elucidating the mechanical properties and folding kinetics of naked DNA/RNA molecules. Direct measurements of the length of extension of single DNA molecules as a function of force, generating force-extension curves, offers insight about the biopolymer properties and provide tests for elasticity theories such as the worm-like chain (WLC) and freely-jointed chain models [70]. Knowledge of these properties sets the stage for more bio-functional experimental assays in nucleic acid polymer physics, such as studying DNA supercoiling transitions using both magnetic [63] and optical tweezers [71] as mentioned previously. Additionally, the determination of mechanical melting energies of complementary DNA strands upon applied force [72,73], as well as the unzipping force of DNA and RNA hairpins, are established applications of single-molecule force techniques [19,20,74,75].

1.3.2 Protein Folding and Unfolding

The adoption of specific 3-D conformations upon folding determines protein function in often mechanically stressful environments [76]. Single-molecule force measurements provide tools to unfold individual proteins mechanically rather than through chemical or thermal means. Comparison between chemical denaturation and applied mechanical tension suggests a similar energy barrier, and transition state, to unfolding of immunoglobulin domains promoted by either technique [48]. As applied force increases, the protein unfolding pathway may be divided into three stages: 1) inter-domain hinge motion; 2) domain deformation and unfolding; and 3) secondary structure denaturation (e.g., α-helices, β-sheets) [76]. The first mechanical unfolding experiments were performed on the modular protein titin using AFM and optical tweezers; and the foce-extension curves for an unfolded polypeptide were described by the WLC model [23,24,47]. Intermediate conformational states could be observed along the protein unfolding pathway, contributing to a picture of a protein folding energy landscape [77].

1.3.3 Protein-Protein Interactions

Ligand-receptor interactions are essential cellular processes controlled by a complex array of intra and intermolecular forces. The recognition forces between streptavidin and biotin or their analogs were the first to be measured as being one of the strongest non-covalent interactions in nature [55,78]. Adhesion forces between many antigen/antibody pairs and ligand/membrane receptors have been measured with certain constant loading rate, or pulling speed [51,53,60,79]. Rupture forces of soluble *N*-Ethylmaleimide-sensitive fusion attachment protein receptor (SNARE) complexes, the protein complexes that mediate membrane fusion, were also investigated by AFM, revealing dissociation kinetics and the sequence of interactions by the SNARE complex important for exocytosis[80,81]. Recently, MPA and BFP were used to study the interaction between a T-Cell receptor and its antigenic peptide-major histocompatibility complexes [82].

These types of single-molecule pulling measurements are often not at equilibrium, and the measured interaction forces vary broadly for the same ligand/receptor pair depending on the loading rate [50,83]. The same is true when applying unfolding force to a protein or a nucleic acid hairpin structure; however, equilibrium thermodynamic parameters such as the free energy can still be obtained from non-equilibrium measurements [84]. To this end, the development of dynamic force spectroscopy has been instrumental in exploring the loading rate effects on ligand-receptor interactions [83]. The observed force may also vary depending on the measurement technique. For example, single talin molecules were unfolded at lower forces using magnetic tweezers than with AFM, which may be due to differences in the length of time the force is applied [85].

1.3.4 Forces Generated by Protein Motors

Using single-molecule force spectroscopy, we can perform tug of war with single protein motors to determine the minimum stall force for preventing ATP-dependent protein translocation. A variety of protein motors have been investigated, including the motor proteins myosin [14,86] kinesin [15-17] and dynein [87] moving on the cytoskeleton, DNA translocases,[29] RNA and DNA polymerases translocating a DNA template [27,28], DNA packaging motors [21,22] and a promotor of branch migration of a DNA 4-way (Holliday) junction [39] (summarized in Table 1.1). Clearly, protein motors generate a range of forces measurable with various force techniques. The ability to detect forces exerted on biomolecules can provide important insights into the effects of mechanical tension at the cellular level, and incorporation of additional reporter methods such as fluorescence extends the capabilities of the current force-sensing techniques.

1.4 Figures and Tables

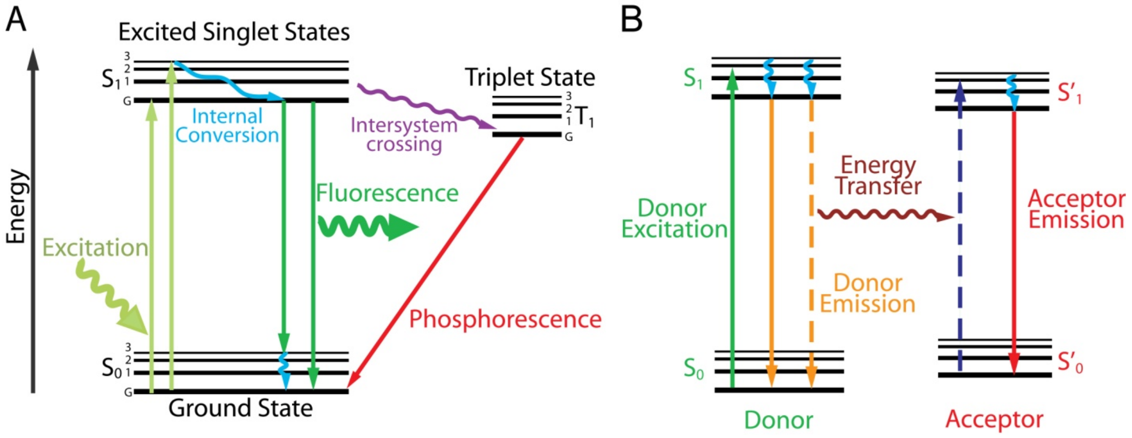

Figure 1.1 (A) A Jablonski diagram depicting the energy levels of a fluorescent molecule. S_0 represents ground state. S_1 and T_1 represent the singlet and triplet excited states respectively. The multiple black lines represent multiple vibrational energy levels within each primary energy state. (B) An energy diagram for fluorescence resonance energy transfer between two fluorescent molecules (donor and acceptor molecules).

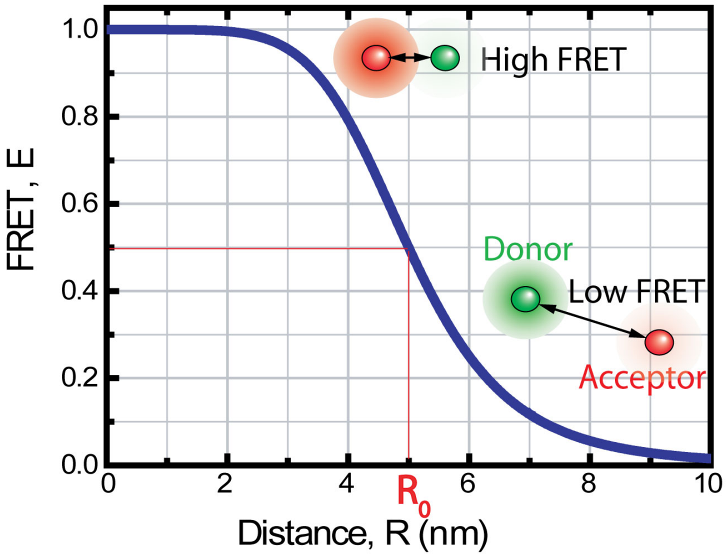

Figure 1.2 FRET Efficiency as a function of the separation distance (R) between the donor (the green circle) and the accepter (the red circle). for a R_0 =5 nm. At $R=R_0$, E=0.5. In the distance range of 3-8 nm, FRET is sensitive enough to report the distance change between the donor and the acceptor.

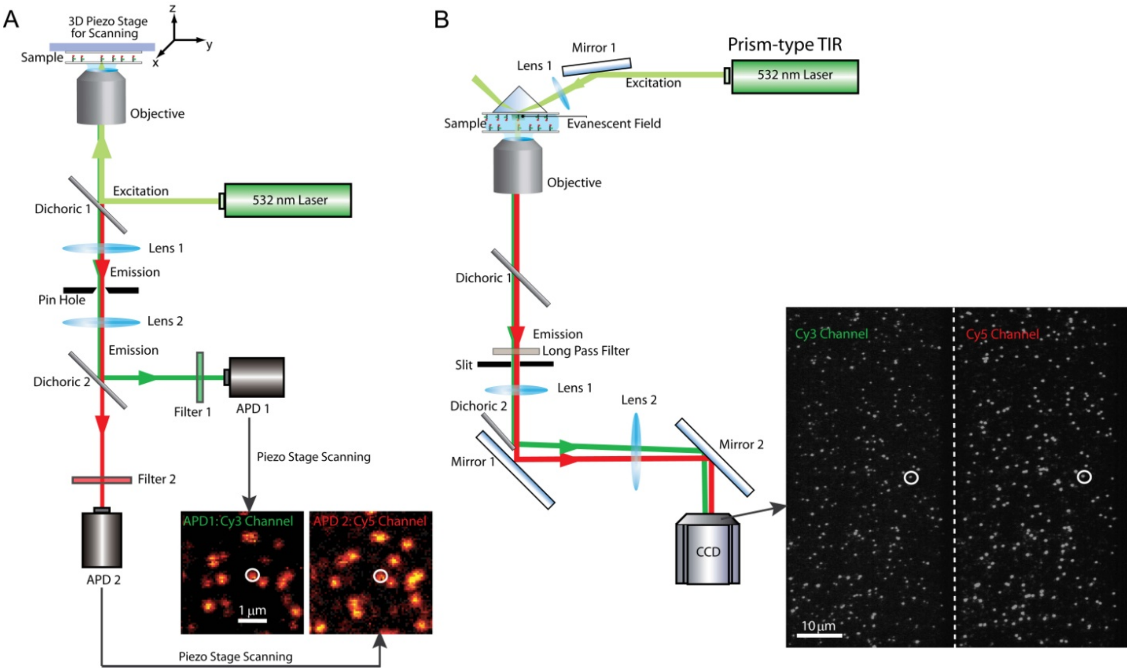

Figure 1.3 (A) Optical scheme for confocal microscopy with typical images of surface-immobilized single biomolecules carrying a Cy3 and a Cy5 fluorophore. The images were obtained by scanning the sample stage in x-y plane while recording the photon counts using two avalanche photodiodes (ADPs; one for Cy3 signal and the other for Cy5 signal). (B) Optical scheme for total internal reflection (TIR) microscopy with a typical dual-channel EM-CCD image of surface-immobilized single biomolecules carrying a Cy3 and a Cy5 fluorophore. The white circles identify the Cy3 and Cy5 images from a same biomolecule.

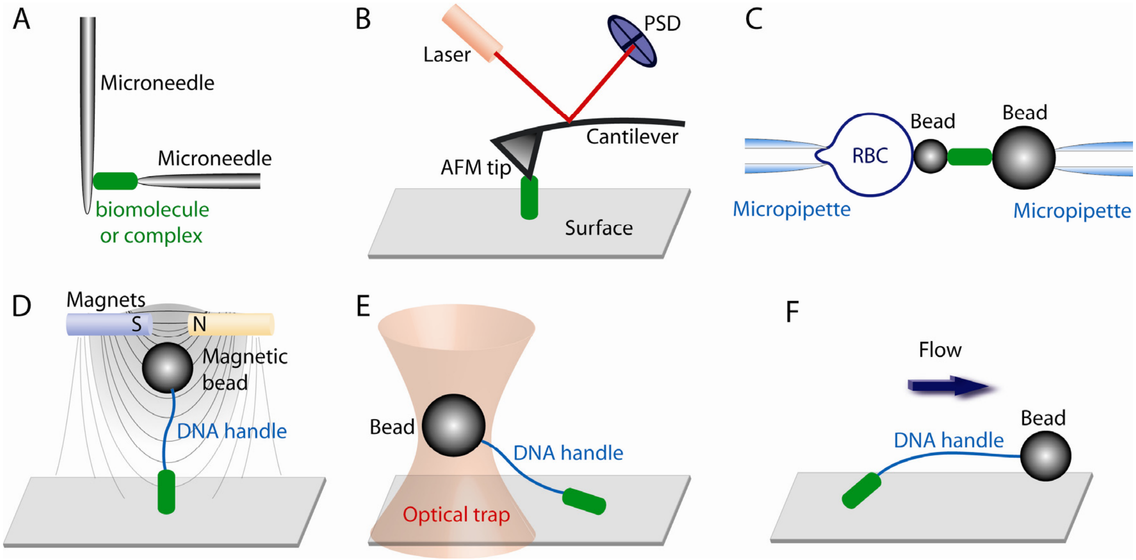

Figure 1.4 Schematic of single molecule force spectroscopy techniques (not to scale). (A) Glass microneedles, (B) atomic force microscopy (AFM), (C) biomembrane force probe (BFP), (D) magnetic tweezers, (E) optical tweezers, and (F) flow-induced stretching. The shape in green represents the biomolecule or the complex (e.g., ligand-receptor and protein/DNA complex) under tension. The force transducers are a soft microneedle, a AFM tip, a red blood cell (RBC) with attached bead, a magnetic bead trapped in a magnetic field, a bead trapped in an optical field, and a bead in a flow field from (A) to (F), respectively. To apply force, one end of the molecule of interest is attached to the force transducer, and the other end is attached to a stiff object or a surface, and the stiff object or the surface is moving away from the force transducer.

Description	Force (pN)	Measuring techniques	References
Force to break a covalent bond	$\sim 10^3$	AFM	51
Force to unzip DNA/RNA	9-20	Glass microneedles Optical tweezers	19,72,73,84
Average stall force of cytoskeletal motor proteins (Myosin, Kinesin and Dynein)	3-7	Optical tweezers Glass microneedles	14-17,86
Average stall force of DNA translocases (RNA/DNA polymerase, FtsK)	25-40	Optical tweezers Magnetic tweezers	27-29,88 39 21
Average stall force of DNA junction branch migration motor protein (RuvAB)	25	Magnetic tweezers	39
Average stall force of Phage Φ29 for DNA package	57	Optical tweezers	21
The force to disrupt the bond between two actin monomers	108±5	Glass microneedles	44
The force to disrupt fibronectin-integrin-cytoskeleton linkage	2	Optical tweezers	89,90
Adhesion force between biotin-strepavidin	160±20	AFM	55,78
Typical adhesion force range between a cell-surface-receptor (intergrins, cadherins, selectins) and its cognate ligand	~5-300	AFM, BFP, Flow-induced stretching, Optical tweezers	52,79,91
Typical adhesion force range for antigen/antibody pairs	~10-500	AFM, BFP, Optical tweezers	52,79,91
Unfolding force of a protein domain (titin)	30-300	AFM, optical tweezers	23,24,47

Table 1.1 Biological forces measured using single-molecule force methods *in vitro*

Chapter 2
Single Molecule Fluorescence-Force Spectroscopy †

2.1 Introduction

As mentioned in Chapter 1, optical tweezers and single molecule FRET are two mainstream techniques used in the field of single molecule biophysics study. However, with the fluorescence method alone, one can not apply forces or manipulate the biomolecules. On the other hand, with the force method alone, one has to apply relatively high forces to achieve high spatial resolution to detect conformational changes of a single biomolecule through the force spectroscopy [92]. At weak forces, the flexible tether connecting the mechanical probe to the biological molecule is not fully stretched and therefore cannot transmit small movements. Additionally, conformational change detection with a force method alone is limited only to one vector which is defined by the two tethering positions of the biomolecule. By combining single molecule force and fluorescence methods (termed Fluorescence-Force Spectroscopy), one can obtain detailed information about the conformation or the location of the biomolecule using single molecule fluorescence while having the capability of manipulating the biomolecule using optical tweezers at the same time. The force applied to the biomolecule can be arbitrary low because FRET can now report the conformational changes of the biomolecule instead of following the bead displacement in the optical tweezers experiment. The fluorescence probes (Cy3, Cy5, Alexa555, etc) can be positioned at different desired locations on the biomolecule or the biological complex to probe the dynamics along various vectors, which increases the sophistication of the experimental design and maximizes the information content of the acquired data.

---

† This work in Chapter 2 has been published as papers:

- Zhou, R., Schlierf, M. & Ha, T. Fluorescence-force spectroscopy at the single-molecule level. *Methods Enzymol* **475**, 405-426 (2010)
- Hohng, S., Zhou, R. et al. Fluorescence-force spectroscopy maps two-dimensional reaction landscape of the holliday junction. *Science* **318**, 279-283 (2007).

Although the marriage of the two techniques is useful, it has not become reality until recently because of the existence of two major technical barriers: 1) a typical trapping laser has the intensity roughly 15 orders of magnitude greater than that emitted by a single fluorophore, which obviously obscure the relatively weak fluorescence signal; 2) The high flux trapping and position detection lasers can reduce markedly the lifetimes of the single fluorophore through unwanted two-photon excitation of dyes or other destructive photochemical mechanisms [93-98]. Recently, we showed that with the combination of an optical tweezers setup and a single-molecule FRET confocal microscope the complex energy landscape of Holliday junctions could be studied in detail [99]. In the sections below, we give an overview of the experimental setup that allows this hybrid instrument to study not only Holliday junction dynamics but also other nucleic acid mechanics and even protein-nucleic acid interactions. We anticipate that fluorescence-force experiments can significantly extend the knowledge and understanding of essential reactions in living cells.

2.2 Instrument Overview

2.2.1 Optical Scheme of the Hybrid Instrument

In this section we briefly describe the hybrid instrument that we have developed to combine the surface-coupled optical tweezers and a confocal microscope. Figure 2.1A illustrates schematically the optical scheme of the combined instrument. The combined optical trapping and single-molecule confocal fluorescence instrument is built around a commercial inverted microscope (IX71, Olympus) equipped with a three-dimensional piezo stage (P-527.3CL, Physik Instrumente). The piezo stage is used for the precisely positioning and movement of the sample chamber. The infrared (IR) trapping laser beam (1064 nm, 800 mW, Spectra-Physics, Excelsior-1064-800-CDRH) is coupled through the back port of the microscope, while the fluorescence excitation laser beam (532 nm, 30 mW, World StarTech) is directionally controlled by a two-dimensional piezo-controlled steering mirror (S-334K.2SL, Physik Instrumente) and coupled through the right side port (Figure 2.1A). The beams are combined via a dichroic mirror (D2: 780DCSPXR; Chroma) into an oil-immersion objective (UPlanSApo, 100×, NA = 1.4, Olympus). The intensity profile of the trapping laser in the back focal plane of the condenser

(Achromat/Aplanat, NA = 1.4, Olympus) is imaged onto a quadrant photodiode (QPD; UDT SPOT/9DMI) to detect the deviation of the trapped bead position from the optical trap center. The applied force The Cy3 and Cy5 emission signals are isolated from the reflected infrared light (F3: HNPF-1064.0-1.0, Kaiser) and are band-pass filtered (F1: HQ580/60m, F2: HQ680/60m, Chroma) before imaged onto two APDs, respectively. In order to image the surface-tethered beads before trapping them, the bright-field image of the trapped beads is imaged onto a video-rate CCD camera (GW-902H, Genwac) at the eye piece of the microscope. A detailed description of the calibration for the optical trapping part is given in the following section *Optical Tweerzers in the Hybrid Instrument* (Section 2.3) and further details on the fluorescence excitation and detection are given in the corresponding section *Confocal Microscope in the Hybrid Insturment* (Section 2.4).

2.2.2 Experimental Scheme for Fluorescence-Force Spectroscopy

Figure 2.1B shows a not-to-scale cartoon of the experimental scheme for fluorescence-force spectroscopy where optical trapping and smFRET measurement are combined simultaneously. As mentioned in Chapter 1, the lifetime of the single fluorophore used for FRET measurement (Cy3, Cy5, etc) is strongly reduced by a nearby IR trapping laser. In order to overcome this limiting factor, one might either choose alternating excitation and IR trapping beams for a temporal separation or a relatively large spatial separation. Our setup is built such that we use a long DNA spacer for the large spatial separation of the excitation laser beam and the trapping laser beam. Conveniently, the DNA from the lambda phage (Promega) with a length of 48502 base pairs (bp) provides a natural long DNA. λ-phage DNA adopts either a circular from or a linear form that has two complementary 12 nucleotide (nt) single-stranded overhangs (termed *cos*-site) . A complementary short DNA oligonucleotide modified with digoxigenin (Integrated DNA Technologies, Inc. Coralville, IA, USA) is annealed to one of the 12 nt overhang of the λ-DNA and provides the possibility to specifically attach the λ-DNA to anti-digoxigenin coated beads (1 μm in diameter). The other λ-DNA overhang is attached to biomolecule(s) of interest as illustrated in Figure 2.1B. The biomolecule(s) can be tethered to the surface via a specific biotin–neutravidin interaction. In the simplest case, the biomolecule of interest is a nucleic acid construct. Since both the λ-DNA and beads tend to interact non-specifically with the coverslip surface, it is crucial to ensure optimal surface passivation, especially if unlabeled and/or labeled proteins are added to the assay. The section *Sample Preparation* in this chapter gives a detailed description of DNA and protein labeling, surface passivation, anti-digoxigenin coated bead preparation and the final sample chamber assembly protocols. In order to avoid non-specific interactions between the trapped bead and the surface, the IR trapping laser focus is chosen to be approximately 250-500 nm above the surface, while the focus of the exciation laser was set to align with the coverslip surface. We have successfully used this method to map the reaction energy landscape of a DNA four-way (Holliday) junction structure[100], to calibrate a FRET-based *in-vivo* force sensor [101], and to study SSB/DNA interactions [102].

2.3 Optical Tweezers in the Hybrid Instrument

2.3.1 Determination of the Bead Trapping Height

A critical factor for surface tethered, combined fluorescence-force assays is the z-height difference between the focus of the excitation (or confocal) laser beam and the focus of the trapping laser beam. When the surface-tethered bead is trapped (Figure 2.1B and Figure 2.2A), one does not want the bead trapping height (or trapped bead height) to be too small, since then the bead might interact with the coverslip surface and a large measurement error is induced from the precision of the trap stiffness determination because the hydrodynamic drag on the bead strongly depends on the the trapped bead height. On the other hand, the oil immersion objective does not allow deep trapping in solution due to spherical aberrations [103]. Furthermore, in the case of deep trapping there are necessary corrections on the actual pulling force since the angle between the surface tether point and the tether at the bead is no longer close to zero ($\cos(\varphi) \approx 1$) and the changes of the bead trapping height at different applied forces become significant. In order to determine the bead trapping height, the focus of the confocal beam needs to be preset on the surface of the coverslip such that the diameter of the reflected light spot of the confocal laser detected at the eyepiece CCD camera can be minimized while the coverslip surface is being imaged. The trapping height here is defined as the distance along *z*-axis from the coverslip surface to the bottom of the trapped bead, when the confocal beam is focused. This is also the working height in an actual experiment. To determine the bead trapping height, we use a similar approach described by Lang and coworkers [104]. First, a freely floating bead in 10 mM Tris-HCl, pH 8.0 (buffer A) is trapped. After the confocal beam is focused, the cover slip surface together with the sample chamber is raised by the piezo-electric stage as illustrated in Figure 2.2A, while recording the sum signal of the QPD. Similar to Ref.[104], the voltage is initially constant, showing only small oscillations, while when the bead touches the surface, the voltage is first rising and then shows a strong drop (Figure 2.2B). The point where the QPD voltage suddenly starts to rise is recorded as the point when the bead touches the surface. Since this approach depends on the actual focusing of the surface and the Brownian motion of the bead in the trap, this procedure is repeated several times, until a Gaussian distribution of the average bead height above the surface is obtained. Figure 2.2C shows such an experimentally obtained Gaussian distribution with an average height of ~390 nm. The distribution width mainly originates from two sources, the focal point determination and the Brownian motion of the bead. Due to a planar interface between two mismatched indices of refraction, e.g., between the coverslip and the aqueous medium (buffer A in this case), the measured trapping height has to be corrected by a factor [103] such that $z_{real} = 0.82 \cdot z_{measured} = 0.82 \times 390 nm \approx 320 nm$.

The real bead height is therefore in our case 320 nm and is used in the following calibration procedures.

2.3.2 Position Detector Calibration

In the following steps, we describe the calibration of the QPD, the device we use to detect the bead position (i.e. the displacement of the trapped bead in the *xy* plane from the trap center) when a force is applied. Since the position of the bead is imaged in the back focal plane of the condenser on the QPD, a calibration of the QPD signal is required. The beads are immobilized on the coverslip non-specifically by putting the beads in buffer B (10 mM Tris-HCl, pH 8.0, 20-50 mM $MgCl_2$). This ensured that beads close to the coverslip surface tend to stick strongly through electrostatic interactions. To begin the QPD calibration process, a stuck bead is found and the confocol beam is focused on the surface (Figure 2.3A). Then the stuck bead is elevated with the surface along *z*-axis by the amount of z_{real} determined from the previous section so that the stuck bead is brought to the bead trapping height for an actual expereiment. Then the relation of the position of the bead to the trapping beam is determined by raster scanning the stuck bead with the piezo stage in the *xy* plane through the trapping beam at that elevated *z*-position, while recording the QPD signals. The QPD is a four-element photodiode array providing four voltage signals (A, B, C and D) that depend on the amount of laser light within each element area (Figure 2.3B). For the position detection purpose, the four values are converted to *V*1 and *V*2. The *V*1 signal is composed of *((A+B) – (C+D))/(A+B+C+D)*, while *V*2 = *((A+D)-(B+C))/(A+B+ C+D)*. Similar to Lang *et al.* the back focal plane signals V1 and V2 of a stuck bead are taken at various positions to the center of the trapping beam (Figure 2.3C) [104]. A fifth order polynomial function is fitted to the QPD signals, $x = \sum_{i,j=0}^{5} a_{ij} V1^i V2^j$, $y = \sum_{i,j=0}^{5} b_{ij} V1^i V2^j$, in order to obtain a relation between the displacement of the bead from the trap center in the *xy* plane (*x*, *y*) and (*V*1, *V*2) signals of the QPD. Figure 2.3C shows the residual errors from the fitting and those coefficients are stored for the actual experiment.

2.3.3 Determination of the Trap Stiffness

Knowing the calibration factor that converts the QPD signal to the actual displacement of the bead, we are able to determine the stiffness of the optical trap. This final calibration step is done with trapped non-stuck beads in solution. After focusing the confocal laser beam on the surface, we record the thermal fluctuations of a single bead over a certain time period with a sampling frequency of 40-200 kHz. Using this thermal motion of the bead in x- and y-direction, two very common methods are used to obtain the trap stiffness k_{ot}. The first method simply uses the equipartition theorem, that describes the relation between the mean square displacement (MSD) of the bead and the trapping stiffness k_{ot}:

$$k_{ot} = \frac{k_B T}{\langle x^2 \rangle} \qquad (2.1)$$

where k_B denotes the Boltzmann constant, T the absolute temperature and $\langle x^2 \rangle$ the MSD displacement.

The second common method determines the roll-off frequency of the Brownian motion of the bead in the optical trap. Therefore one calculates the power spectrum of the Brownian motion of the bead and fits the power spectrum with a Lorentzian function (Figure 2.4) according to

$$P = \frac{k_B T}{cons \cdot (f^2 + f_0^2)} \quad (2.2)$$

The roll-off frequency f_0 is then used to determine the stiffness of the optical tweezers setup following:

$$k_{ot} = 2\pi \cdot \gamma(z) \cdot f_0 \quad (2.3)$$

where $\gamma(z)$ is the corrected drag coefficient. Keeping the optical tweezers close to the surface requires a correction of the apparent drag coefficient $\gamma(z)$. This hydrodynamic effect, together with the filtering effect of the QPD, also needs to be taken into account when fitting the power spectrum [105-107]. We use the following expression to correct for the altered drag coefficient:

$$\frac{\gamma_0(z=\infty)}{\gamma(z)} = 1 - \frac{9}{16}\left(\frac{r}{r+z}\right) + \frac{1}{8}\left(\frac{r}{r+z}\right)^3 - \frac{45}{256}\left(\frac{r}{r+z}\right)^4 - \frac{1}{16}\left(\frac{r}{r+z}\right)^5 \quad (2.4)$$

where r denotes the bead diameter (in our case 500 nm) and z denotes the real average bead height above the surface.

Since our typical experimental assay does not allow a calibration of each bead, we record many time traces from different beads and determine the average spring constant (~ 0.1 pN/nm in our case). The variation between the spring constants and several beads is on average less than 10%.

2.4 Confocal Microscope in the Hybrid Instrument

As described in the previous chapter, confocal microscopy has been used for single molecule fluorescence studies for years [12,108] and one way to obtain the sample image is to raster scan the peizo-stage. An alternative way to obtain the image is to use a two-dimensional piezo-controlled mirror to raster scan the excitation laser beam over the sample stage while keeping the sample stage fixed (Figure 2.1A). A telescope system containing two lenses [98] (L1 and L2) is used for steering the confocal excitation beam (532 nm) so that the excitation laser focus can scan for individual fluorescently labeled biomolecules immobilized on the coverslip (Figure 2.4). For keeping the excitation beam collimated before and after the telescope, the distance between lenses L1 and L2 is the sum of their focal lengths (Figure 2.5A). Beam steering is achieved by placing the piezo-controlled mirror in a plane conjugate to the back aperture of the objective so that the lens L2 images the lens L1 onto the back aperture plane. This can be easily achieved by arranging lenses L1 and L2 as follows: the distance between the piezo-controlled mirror and lens L1 is set to the focal length of L1 (f_1), the distance between lens L2 and the back aperture plane of the objective is set to the focal length of L2 (f_2) (Figure 2.5B). Then a rotation of the laser beam direction (θ_1) at the mirror position is propagated into a rotation (θ_2) at the back aperture where θ_2 is given by,

$$\theta_2 = \theta_1 \frac{f_1}{f_2} \qquad (2.5)$$

The focus of the excitation laser beam is set right on the coverslip surface and the laser spot on the coverslip moves as the incident angle of the beam through the objective lens changes.

A fluorescent bead sample is needed for the alignment of the pinhole and the APDs in the confocal light path. The procedure is:

1. Dilute the fluorescently labeled bead stock (FluoSpheres® carboxylate-modified beads, 0.2 µm, crimson fluorescent, 625/645, 2% solids, Molecular Probes) to an appropriate concentration (Typically 200- to 500-fold dilution) in buffer B (10 mM Tris-HCL, pH 8.0, 20-50 mM $MgCl_2$).
2. Inject the diluted beads into a sample chamber. Incubate for 10 min.
3. Rinse with buffer B to remove excess beads in the solution and use epoxy to seal the chamber.

After focusing the 532-nm confocal excitation laser onto the flow chamber surface, the APD and pinhole position can be precisely adjusted with a precision XYZ stage to maximize the photon counting rate of the APDs.

2.5 Coalignment of Confocal Microscope and Optical Tweezers

2.5.1 Calibration of Piezo-Controlled Mirror

To simultaneously operate the single molecule confocal microscope and optical trap, the confocal excitation beam has to be programmed to follow the motion of the molecule when the molecule is moved with the piezoelectric stage for stretching. The deflection angle of confocal beam can be controlled precisely by the piezo-controlled mirror but its resulting displacement in the sample plane is unknown and needs to be calibrated. Therefore, mapping is required between the deflection angle of the piezo-controlled mirror (α, β) and the resulting displacement in the sample plane (x, y). In addition, the origin of the piezo-controlled mirror should be preset to a particular position such that the confocal spot is overlapped in the sample plane with that of the trapping laser. The piezo-controlled mirror can be calibrated as follows:

1. Prepare two fluorescent bead samples. One has stuck beads on the cover slip (please find the protocol in section 4.1), the other contains free beads in the chamber. To make the free bead sample, the protocol is similar to that for a stuck bead sample, but buffer A (10 mM Tris-HCl, pH 8.0) instead of buffer B is used to dilute and inject the beads.
2. Use the free fluorescent bead sample to reset the mirror origin. Focus the confocal beam to the sample plane and turn on the trapping laser. Some fluorescent beads can be trapped to the center of the laser trap. Steer the mirror to scan the area where the trapping laser spot is located with a stepsize of 32 nrad. Figure 2.6A (upper panel) shows a typical mirror scan image of trapped beads. Set the origin of the mirror to the center pixel position of the fluorescent spot. Note that the fluorescent spot is ellipse-like because the mirror calibration has not been performed yet. Using a calibrated mirror to scan the trapped beads with a stepsize of 100 nm in the sample plane, a circular fluorescent spot is obtained instead (Figure 2.6A, lower panel). Calibration is accomplished in the following step.
3. Use the stuck bead sample to calibrate the mirror. The stuck bead sample is imaged sequentially either by scanning with the piezo stage (scan area, 38.4 μm × 38.4 μm) while fixing the mirror or by scanning with the mirror while fixing the

piezo stage. Two third order polynomial fits, $x = \sum_{i,j=0}^{3} m_{ij}\alpha^i\beta^j$, $y = \sum_{i,j=0}^{3} n_{ij}\alpha^i\beta^j$, are used to map angle coordinates into spatial coordinates in the sample plane. Then two mapping files containing the coefficients m_{ij} and n_{ij} are generated, which are later used for steering the confocal beam to any desired position in the sample plane. Typical mapping images were shown previously [99].

With the calibrated piezo-mirror, we can ask the confocal spot to follow the movement of the piezo stage by written software such that the confocal spot keeps track of the fluorescently labeled molecule under investigation.

2.5.2 Setting Up the Tethered Molecule for Measurement

Once the calibrations of QPD and piezo-controlled mirror are complete, fluorescence-force measurements can be performed on a sample. After a surface-tethered λ-phage DNA is optically trapped via the attached bead, the stretching curve is obtained by moving the coverslip in x- and y-direction with the piezo stage (Figure 2.6C). The symmetry of the stretching curves can be used to roughly determine the tethered position by finding the central positions in two orthogonal stretching directions in the *xy* sample plane. The origin of the piezo stage can then be reset to this central position. After considering the bead radius and the deviation of the bead from the trap center, force-extension curves of the molecule (blue line, upper inset, Figure 2.6C) are obtained and can be fitted with the worm-like-chain (WLC) model (red solid line) yielding a persistence length of about 40-50 nm [109].

Next the fluorescently labeled biomolecule is displaced by typically 13 μm for the spatial separation of the trapping and excitation laser beams. The confocal image around the target molecule is taken by scanning the confocal spot in the sample plane (scan area, 3.2 μm × 3.2 μm) using the steering mirror calibration. A more accurate position of the fluorescently labeled molecule and therefore the accurate surface attachment point is then determined from the image (Figure 2.6C, lower inset). For the fluorescence-force measurement, the piezo stage was moved further away to reach different forces, while both force and the fluorescence signals are recorded.

2.6 Sample Preparation Protocols

A good sample preparation is essential for fluorescence-force measurement. For example, a high dye labeling efficiency, appropriate annealing and sample assembly lead to a successful fluorescence-force measurement.

2.6.1 Nucleic Acid and Protein Labeling

Since the λ-phage DNA linker is acting as an entropic spring, the force resolution is limited in fluorescence-force spectroscopy. Therefore, the FRET or fluorescence data, rather than the force values, are the read-out of the conformational changes of single molecules. The fluorescent probes (donor and acceptor) need to be engineered to the desired locations on individual nucleic acids or proteins. There are many conjugation strategies for either proteins or nucleic acids as previously described [9,110], but a high labeling yield is achieved much more easily for nucleic acids than proteins. 3' or 5' fluorescently end-labeled DNA/RNA oligonucleotides can be ordered from companies (for example, Integrated DNA Technologies). Fluorescent probes may also be incorporated internally into the nucleic acid chain using phosphoramidite chemistry during oligonucleotide synthesis. This is optimal in cases where the dynamic nature of the biological system is affected little by the internal modification. Not quite understand the comment here either In most of the cases, an alternative method is recommended for internal labeling where the DNA backbone is not broken: an amine-modified base (typically thymine), instead of a fluorescent probe, is inserted into the desired location, which can later react with the *N*-Hydroxysuccinimide (NHS) ester form of the fluorescent probe (GE Healthcare). Purification can be achieved by polyacrylamide gel electrophoresis to separate labeled from unlabeled oligonucleotides. Recombinant engineered cysteine variants of proteins can be easily labeled with maleimide derivatized fluorescent probes, for example, *E. coli* Rep helicase [9,111]. However, there are certain limitations since many proteins carry multiple solvent-exposed cysteines and upon substitution of those cysteines the functionality might be changed or totally lost.

In order to specifically immobilize the molecules of interest on the glass coverslip for single molecule experiments, a biotin-neutravidin linkage is commonly used. A biotin modification is easily introduced by commercially ordered DNA oligonucleotides.

Furthermore, proteins can be biotinylated using similar conjugation strategies as used for the conjugation of fluorescent probes.

2.6.2 Polymer-Passivated Surface Preparation

Although biotinylated bovine serum albumin (BSA) can be used to adsorb to the glass surface for immobilization of biotinylated molecules through neutravidin protein sandwiched in the middle, a polymer-passivated surface coated with polyethyleneglycol (PEG) is highly recommended in order to eliminate nonspecific surface adsorption of proteins and efficiently reduce the surface interactions with nucleic acids and beads. The common protocol for preparing the PEGylated surface contains three steps [110]:

1. Pre-cleaning and surface activation
2. Aminosilanization of the surface
3. PEGylation (Coating the amino-modified surface with PEG–NHS esters)

In the third step, a small fraction (~ 3%) of biotin-PEG–NHS ester (Bio-PEG-SC, Laysan Bio) is mixed with regular PEG–NHS ester (mPEG-SC, Laysan Bio) for the purpose of immobilizing biomolecules. The detailed steps can be inferred from [110]). The PEGylation following this protocol on a glass surface is not as good as on a quartz surface. However, dissolving PEG-NHS ester in 50 mM MOPS (pH 7.5) for PEGylation instead of in 0.1 M sodium bicarbonate (pH 8.5) has been found to improve the PEGylation efficiency resulting in further suppression of nonspecific adsorption on a silicate surface [112]. A higher concentration of KOH (10 M in MilliQ water) for the first cleaning step can also be applied to drastically enhance the aminosilanization result and hence improve the PEGylation efficiency.

2.6.3 Nucleic Acid Construct Preparation

The nucleic acid construct (for example, a four-way Holliday junction, partial duplex, or forked DNA substrates that can interact with proteins) carrying fluorescence dyes (Cy3, Cy5) is pre-annealed from oligonucleotides and contains a 5’ single-stranded tail (5’-GGG CGG CGA CCT) which is complementary to the 12 nt *cos* site of λ-phage DNA. λ-phage DNA adopts either a circular from or a linear form that has two complementary 12 nt single-stranded overhangs. By heating to above the melting temperature of the *cos* site (~ 60-70 °C) for approximately 10 min (please specify temperature here), the circular λ-phage DNA is converted into the linear form with single-stranded 5’ extensions of 12 nt at both ends which are complementary to each other. Thus, we can make the nucleic acid construct annealed with the linear form of a λ-phage DNA using the following protocol:

1. Resuspend and mix the oligonucleotides in a microcentrifuge tube with each final concentration no less than 1 μM in annealing buffer (10 mM Tris-HCl, pH 8.0, 50 mM NaCl). The biotinylated strand should have a slightly lower concentration than the other strands.
2. Put the tube in a heat block at 90-95 °C for 3 min. Remove the heat block from the heater and allow it to slowly cool to room temperature over ~ 2 h.
3. Dilute the pre-annealed nucleic acid product to a concentration of 100 nM, make aliquots and store in the freezer.
4. Prepare 40-μl aliquots of λ-phage DNA (~ 500 μg/ml, Promega) in microcentrifuge tubes. Take one λ-phage DNA aliquot and add 5 μl of 5 M NaCl. Mix very gently (large orifice pipette tips should be used when handling λ-phage DNA to avoid high shearing forces).
5. Place the tube from Step 4 in a heat block at 85-90 °C for 10 min.
6. Bury the tube in ice and incubate for 5 min for fast cooling. Then quickly add 3 μl of 100 nM pre-annealed mixture from Step 3 and 1 μl of 10 mg/ml BSA (New England Biolabs).
7. Rotate the tube for 1-1.5 h at room temperature.
8. Move the tube to a cold room (4 °C) and keep rotating for another hour.
9. Take out the tube from the cold room and add 1 μl of 10 μM digoxigenin-conjugated DNA oligonucleotide (5’-AGG TCG CCG CCC TTT /digoxigenin/-3’) into the tube and keep rotating the tube in the cold room for 1-1.5 h. This generates the complete DNA/RNA construct with a single digoxigenin-tag on one end of the λ-phage DNA and a biotin-tag on the other end.
10. Add 250 μl of 10 mM Tris-HCl, pH 8.0, 50 mM NaCl into the tube and prepare 10-μl or 20-μl aliquots of this completed sample (which is now at a concentration of 1 nM). Store aliquots at -20°C.

2.6.4 Preparation of Anti-Digoxigenin Coated Beads

Anti-digoxigenin is cross-linked to Protein G-coated polystyrene beads following the protocol below so that the beads can be attached to the DNA/RNA template for optical stretching via a Digoxigenin-Anti-digoxigenin interaction.

Buffer solutions:

1. MES buffer: 100 mM MES-NaOH, pH 6.5 (prepare immediately before use).
2. Antibody reconstitution buffer: 0.019 M NaH_2PO_4, 0.081 M Na_2HPO_4, 0.14 M NaCl, 2.7 mM KCl.
3. Bead storage buffer: 0.039 M NaH_2PO_4, 0.061 M Na_2HPO_4, 0.14 M NaCl, 2.7 mM KCl, 0.1 mg/ml BSA, 0.1 % (v/v) Tween-20, 0.02% (w/v) sodium azide.

Protocol:

1. Resuspend protein G coated polystyrene beads (1.0 µm, undiluted, 1.4% solids-latex, Polysciences) and take 250 µl of it to a microcentrifuge tube. Exchange the beads into a freshly made MES buffer by repeating buffer wash for 3-4 times (centrifuge for 4 min at 7000 rpm, carefully pipette off the supernatant, and add 250 µl of MES buffer into the tube).
2. Dissolve 50 mg of *N*-(3-Dimethylaminopropyl)-*N'*-ethylcarbodiimide hydrochloride (EDC hydrochloride, Sigma-Aldrich) in 1 ml MES buffer, and dissolve 50 mg of *N*-Hydroxysuccinimide (NHS, Aldrich) in 1 ml MES buffer.
3. Add 50 µl of EDC hydrochloride and 25 µl of NHS from step 2 into the tube.
4. Tumble the tube for 10 min at room temperature.
5. Dissolve 200 µg of anti-digoxigenin antibody (Roche Applied Science) in 200 µl of antibody reconstitution buffer and add 30 µl of anti-digoxigenin to the tube. Aliquot and shock freeze the remaining dissolved anti-digoxigenin with liquid nitrogen for future use.
6. Keep tumbling the tube for 2 h at room temperature.
7. Stop the crosslinking reaction by adding 20 µl of Tris-HCl buffer (1 M, pH 6.8) and continue tumbling for one hour.
8. Wash the beads three times with bead storage buffer by resuspending and centrifuging as in step 1.

9. Store the beads at 4 °C for future use. This bead solution is 50- to 100-fold diluted in Tris buffer (10 mM Tris-HCl, pH 8.0) for sample assembly in the fluorescence-force experiment as follows.

2.6.5 Sample Assembly

Experimental samples are assembled by sequential infusions of buffer solutions into an open-ended chamber with a volume of approximately 15-20 μl[110]. The infusion is a very important step for successful sample preparation, especially after the DNA/RNA samples are immobilized on the coverslip. An overly rapid fluid flow may result in the adsorption of some internal portion of λ-phage DNA onto the coverslip surface. Incubation in a buffer containing tRNA (Ambion) or short double-stranded DNA (20-30 base pairs) can significantly reduce this non-specific adsorption. The buffer solutions are delivered drop by drop to one open end of the chamber using a micropipette. Slightly tilt the chamber with a small angle such that the liquid drop infuses into the chamber slowly through gravity and comes out the other end. An alternative way for infusing buffer is to adapt an automated pump (PHD 22/2000 series syringe pump; Harvard Apparatus) by using a sample chamber with two 0.75-mm-diameter inlet/outlet holes [110]. The incubations given in the following protocol are performed at room temperature by putting the sample chamber in a humid environment (The chamber was put on a pipette tip box with some water underneath the chamber) to avoid evaporation.

1. Take out a PEGylated coverslip and a PEGylated microscope slide and assemble a fluid chamber.
2. Infuse 25 μl (slightly larger than the chamber volume) of 0.25 mg/ml Neutravidin in T50 buffer (10 mM Tris-HCl, pH 8.0, 50 mM NaCl)and incubate for 5 min.
3. Rinse the chamber with 50 μl of T50 buffer.
4. Infuse 50 μl blocking buffer (10 mM Tris-HCl, pH 8.0, 50 mM NaCl, 1 mg/ml tRNA, 1 mg/ml BSA) and incubate for one hour.
5. Remove one aliquot of completed DNA/RNA sample and dilute it to a final DNA/RNA concentration of 30-50 pM in 10 mM Tris-HCl, pH 8.0, 50 mM NaCl, 0.1 mg/ml BSA. Infuse the diluted solution into the chamber and incubate for 30 min.

6. Rinse sample chamber with 100-120 µl (more than 5 chamber volumes) of buffer A(10 mM Tris-HCl, pH 8.0).
7. Mix 1 µl of the anti-digoxigenin-coated beads as prepared before and 99 µl of buffer A. Complete the buffer exchange from bead storage buffer to the Tris buffer by resuspending and centrifuging twice. Infuse 25 µl of the 100-times diluted beads into the chamber. Incubate for 30 min.
8. Rinse sample chamber with 100-120 µl Tris buffer (10 mM Tris-HCl, pH 8.0).
9. Infuse the final imaging buffer typically containing 20 mM Tris-HCl, pH 8.0, 0.5mg/ml BSA, 0.01 mg/ml anti-digoxigenin, 0.5 % (w/v) D-glucose (Sigma), 165 U/ml glucose oxidase (Sigma), 2170 U/ml catalase (Roche), 3 mM Trolox (Sigma), and 0.1% (v/v) Tween 20 (Sigma) as well as appropriate concentrations of NaCl and divalent ions ($MgCl_2$, $CaCl_2$, etc) for the scientific question at hand. Proteins and other reagents (ATP, DTT, EDTA, glycerol, etc) can be added to the imaging buffer as needed.

2.7 Figures

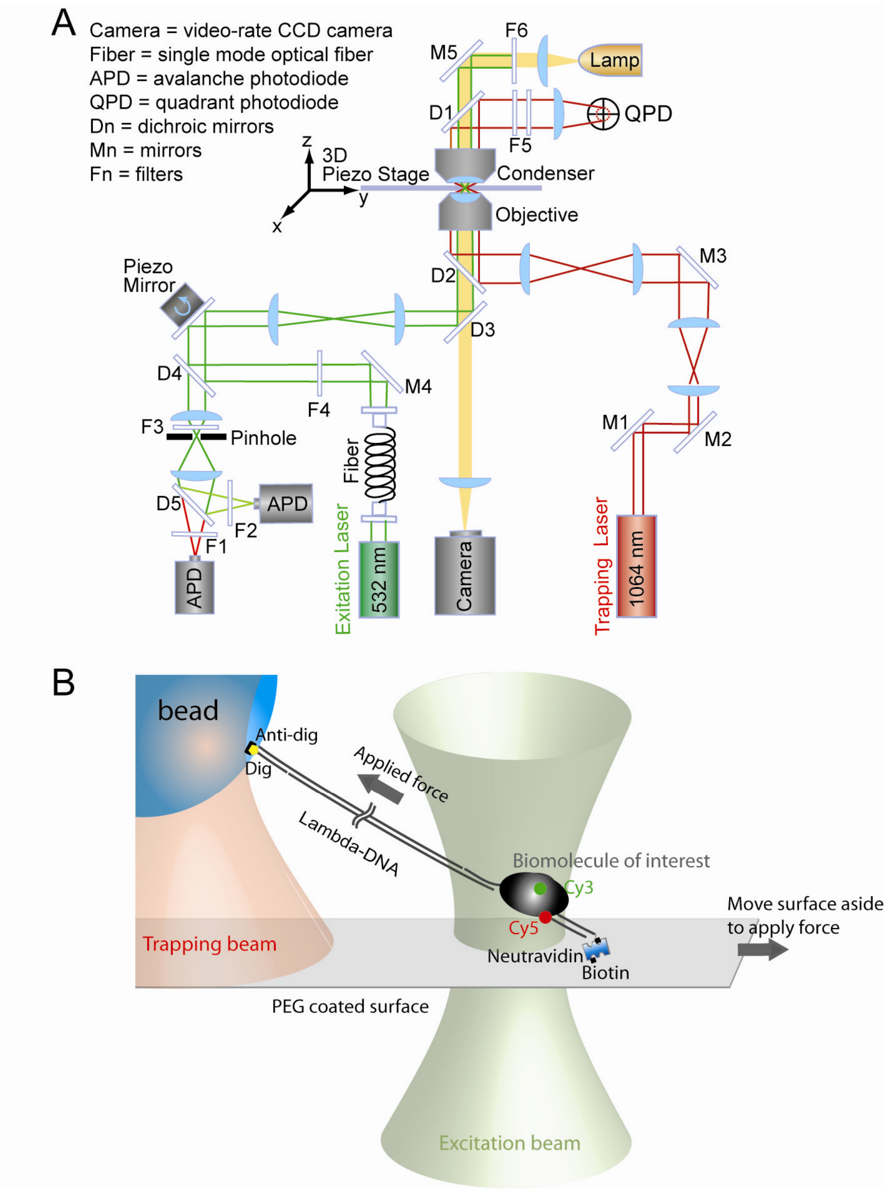

Figure 2.1 Experimental configuration: (A) Optical scheme of the hybrid instrument that combines optical tweezers and confocal microscopy . (B) Experimental scheme for Fluorescence-Force spectroscopy (not-to-scale). Mechanical forces can be applied to the biomolecule of interest by moving the sample surface aside with the piezo-stage. The biomolecule here could be a DNA/RNA molecule, a protein, or a biological complex (DNA-protein complex, protein-protein complex, etc). Cy3 and Cy5 are attached to the desired locations to monitor the conformational dynamics of the system through FRET.

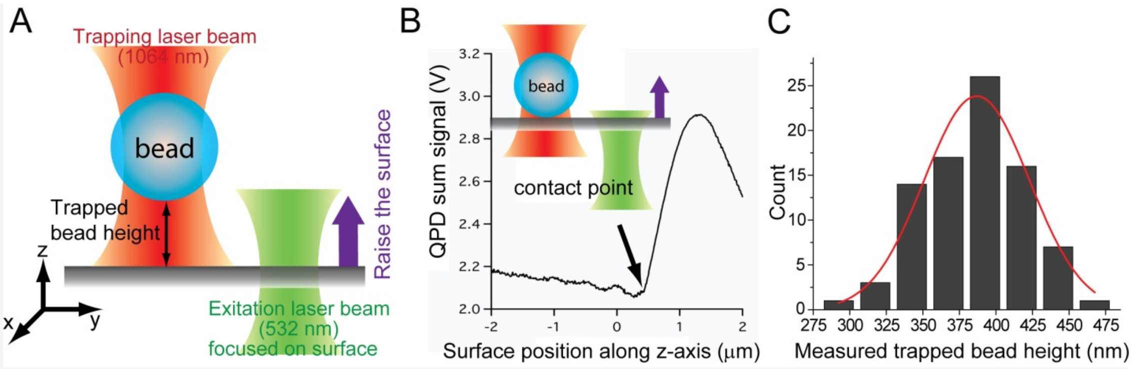

Figure 2.2 Determination of the trapped bead height. (A) A diagram that shows how to determine the trapped bead height. Initially, a freely floating bead is trapped by the optical trap and the 532 nm laser is then focused at the surface by adjusting the height of the objective in *z*-axis. The coverslip surface is next raised to determine the height of the bead above the surface. (B) The QPD sum signal as a function of the surface position along *z*-axis. The QPD sum signal is recorded while moving the surface with a step size of 10 nm in *z*-axis from -2 μm to +2 μm (the initial *z*-position of the surface is zero). The contact point at $z = 0.4$ μm where the curve shows a strong kink and then rises steeply is when the elevated surface touches the bottom of the trapped bead (marked by a black arrow). (C) Histogram of the measured trapped bead height ($n = 85$). The average measured height, $z_{measured}$, is determined to be ~390 nm by a Gauss fit to the histogram.

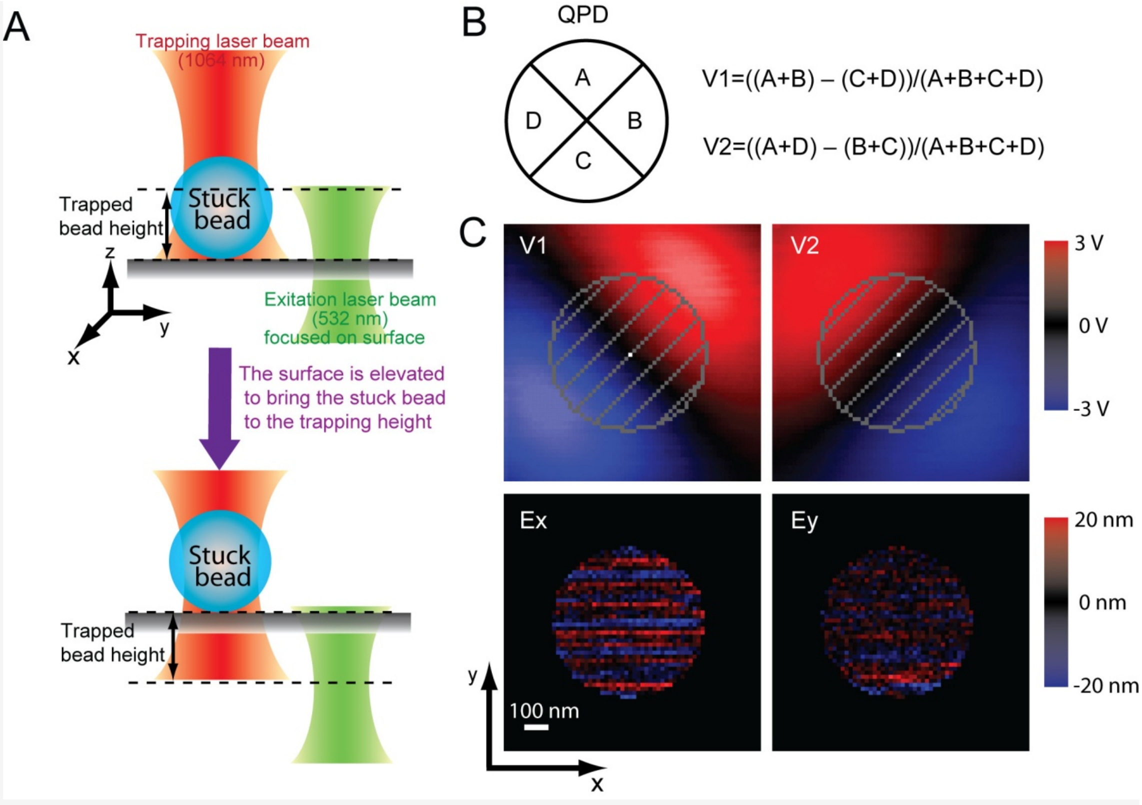

Figure 2.3 The QPD calibration. (A) A diagram that shows how to place a surface-struck bead to the proper height to reproduce the trapped bead height. (B) The cartoon for a QPD containing four elements A, B, C and D. (C) The V1, V2 signals obtained at different bead positions (step size is 16 nm) when raster scanning the stuck beack through the trap center in the *xy* plane. Ex and Ey represent the residual errors from the fifth order polynomial fit (the circle indicates the fitting area).

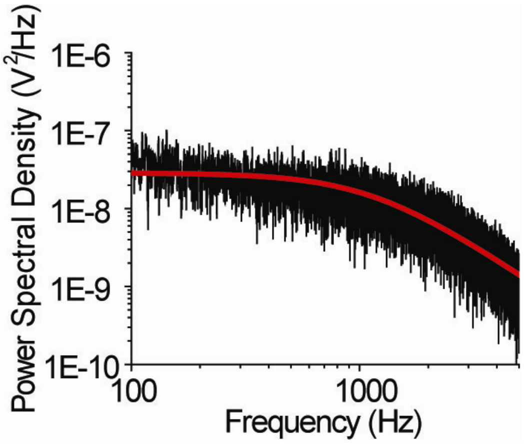

Figure 2.4 An example power spectrum for the trap stiffness determination. The trapped bead (1-µm diameter) is trapped and the confocol beam is focused onto the surface while the bead position in the xy plane is recorded at the sampling rate of 20 kHz. The roll-off frequency f_0 = 1140 Hz obtained from the fit to Equation (2.2) (red solid line).

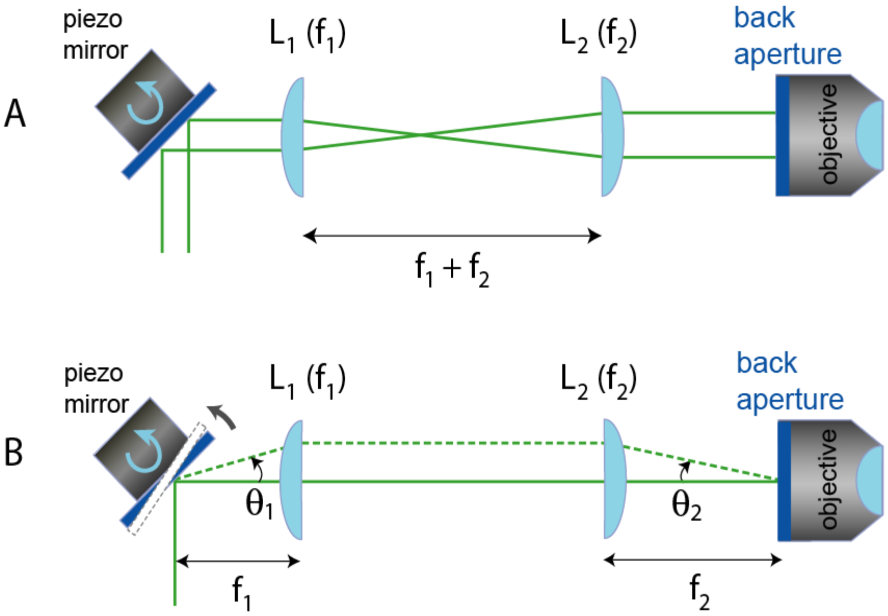

Figure 2.5 Optically conjugated geometry for the piezo-controlled mirror. (A) The distance between L_1 and L_2 is the sum of their focal lengths, to keep the excitation laser beam collimated before and after the telescope system. (B) The piezo-controlled mirror is positioned in the optically conjugated plane of the back aperture of the objective.

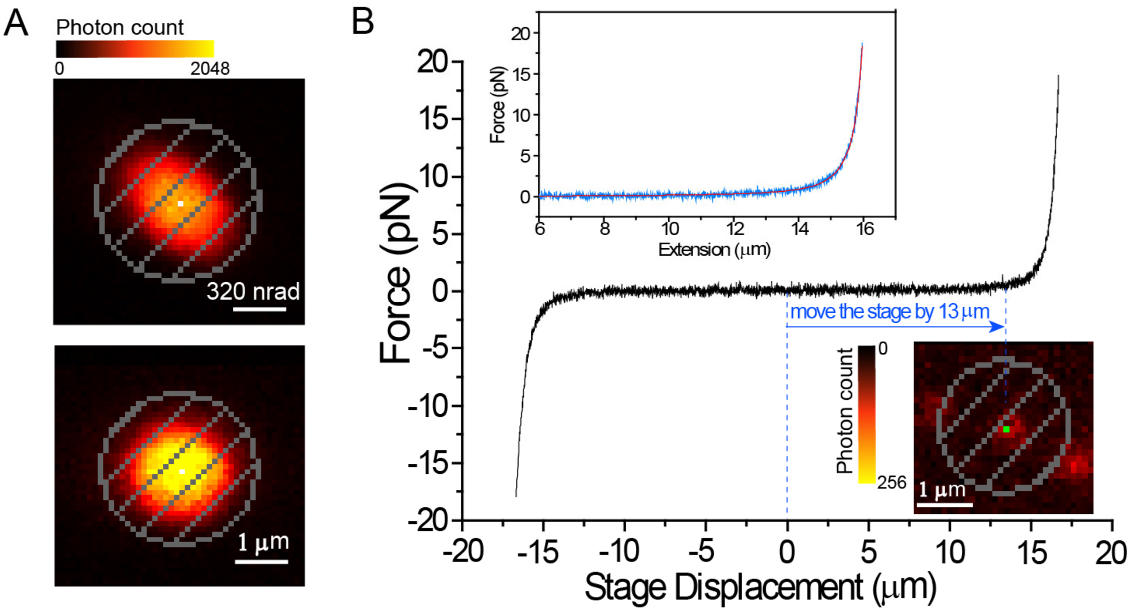

Figure 2.6 Piezo mirror calibration and force-extension curve. (A) The mirror scan image around the area where the fluorescent beads are trapped in the sample plane without (upper) and with (lower) the mirror calibration. (B) A stretching curve and the force–extension curve (upper inset) of the tethered DNA after the origin of the piezo stage is set to the estimated tethered position. A WLC model (red) is used to fit the experimental force–extension curve (blue). The lower inset shows a mirror scan image around the origin of the piezo stage after displacing the stage from its origin by 13 μm. The green dot indicates the center position of the fluorescently labeled molecule that is being stretched.

Chapter 3
Probing Protein Dissociation Mechanism from Single-Stranded DNA[‡]

3.1 Introduction

Single-stranded DNA binding (SSB) proteins are a class of proteins that bind preferentially and with high affinity to single-stranded DNA (ssDNA) which is a key intermediate in DNA metabolic processes including replication, recombination and repair [113-115]. The binding of SSB proteins to ssDNA is mostly in a DNA-sequence-independent manner [116]. SSB proteins are conserved in all kingdoms of life and are essential for cell survival [117]. The *E. coli* SSB (*Eco*SSB), one of the first SSB proteins identified, forms a stable homotetramer in solution (Figure 3.1A) and each *Eco*SSB monomer (19 kDa) possesses one oligonucleotide binding (OB) fold [118,119]. *Eco*SSB is found to ssDNA with multiple modes (Figures 3.1B and 3.1C): At low salt concentrations ($<$10 mM Na^+ or $<$ 0.2 mM Mg^{2+}) and high SSB to DNA ratios, an SSB tetramer binds in the $(SSB)_{35}$ mode in which on average two subunits of the tetramer cover ~35 ssDNA nucleotides (nt); in this mode SSB can form long cooperative clusters along ssDNA. At high salt conditions ($>$ 200 mM Na^+ or $>$ 2 mM Mg^{2+}), a low cooperativity mode ($(SSB)_{65}$) is dominant in which ~65 nt of ssDNA wraps fully around all four subunits so that the two ends of the ssDNA exit the protein in close proximity [118,120-122]. But there are increasingly more evidence to show that the $(SSB)_{65}$ mode is more biological relevant because SSB binds to ssDNA with this mode in the replication foci inside the living cells and SSB has been found to migrate ssDNA back and forth in this mode to facilitate the RecA filament growth on DNA[123,124].

[‡] The work in this chapter has been published as a paper:
Zhou, R. et al. SSB Functions as a Sliding Platform that Migrates on DNA via Reptation. *Cell* **146**, 222-232 (2011)

Not only does SSB binding protect ssDNA from degradation and reduces the secondary structure of ssDNA, but it also controls the accessibility of ssDNA to other proteins. However, for subsequent DNA metabolic processes, SSB needs to give access of its bound ssDNAto other proteins such that the DNA metabolism can resume. *Eco*SSB interacts directly with at least 14 other proteins in every aspect of DNA metabolism that we term SIPs (SSB Interacting Proteins), including DNA Polymerase II, III and V, primase, RecQ, RecO, RecJ, RecG, PriA, PriB, Exonuclease I and IX, Uracil DNA Glycosylase and phage N4 RNA polymerase (Shereda et al., 2008), bringing them to their sites of function. How SSB permits access of SIPs to SSB-bound DNA is unclear. In this chapter, we adopt fluorescence-force spectroscopy described in Chapter 2 to probe the detailed steps by which SSB releases its bound DNA (i.e. the SSB dissociation mechanism from ssDNA).

3.2 Two Distinct Stages of SSB Dissociation

3.2.1 Near-Equilibrium DNA Unwrapping and Rewrapping at Low Forces

The experimental configuration used is shown in Figure 3.2A to investigate the initial stage of the removal of tightly wrapped ssDNA from SSB in its fully wrapped $(SSB)_{65}$ mode. A partial duplex DNA with a 5'-82 nt ssDNA overhang (Figure 3.2B; $(dT)_{70}$ + 12 nt *cos* site of λ-DNA) was immobilized on a polymer-paussivated glass surface using a biotin-neutravidin link. A Cy3 (donor) - Cy5 (acceptor) FRET pair was attached to the DNA, separated by 68 nt of ssDNA ($(dT)_{68}$). A λ-DNA was annealed to the 5' end of the ssDNA tail via its 12 nt *cos* site and to a bead held in an optical trap via the other end via a Dig-Anti-dig interaction. (Figures 3.2A and 3.2B). For simplicity, we depict the complex as a protein disc surrounded by a line, whereas in the 3D structural model of the SSB/DNA complex in its $(SSB)_{65}$ mode, the path of the DNA around SSB resembles the seam of a tennis ball (Figure 3.1C).Our previous work showed that surface immobilization and fluorescent labelling have no measurable effect on the dynamics of the SSB-ssDNA binding mode transitions [121]. At zero force and in 500 mM Na^+, the wrapping topology of the 70-mer ssDNA around an SSB tetramer when bound in the $(SSB)_{65}$ mode under our solution conditions should result in high FRET (~ 0.7) due to the close proximity of the donor-acceptor pair (Figure 3.1C). SSB remains bound to the surface-tethered DNA even 5 hours after removing free SSB from solution (Figure 3.2C). After a surface-tethered bead was optically trapped and the tethered point was determined as we describe in Chapter 2, the coverslip was moved with the piezo-controlled stage to stretch the SSB-bound ssDNA for five force cycles. For each cycle, the stage was moved from a low force position (typically ~0.5 pN) at a constant speed of 455 nm s^{-1} until the force reached a pre-determined value (typically ~ 6 pN), followed by returning the stage at the same speed to the initial low force position (at 20 nM SSB tetramer concentration). The FRET efficiency E decreased and increased gradually (between ~ 0.7 and 0) as the force was increased and then decreased respectively, demonstrating force-induced, progressive DNA unravelling from SSB (Figure 3.2D). Figure 3.2D also shows the donor signal I_D and acceptor signal I_A as a function of time.

In contrast, the E vs. force curve of ssDNA alone without SSB showed E values below 0.2 for the entire force range (Figure 3.3). For each DNA stretching cycle shown in Figure 3.3, the sample stage was moved from a low force position (~0.5 pN) at a constant speed v (455 nm s^{-1}) until the force reached a pre-determined value (~typically between 15-20 pN), followed by a sudden jump of the stage back to the initial low force position. In Figure 3.3B, the FRET efficiency trace obtained in the absence of SSB showed a very small force dependence until Cy3 (donor) was photobleached at t = 20.5 s. In each force cycle, FRET efficiency started from ~ 0.1 and decreased to ~ 0 as the force increased. In contrast to the case of SSB-bound DNA displaying high FRET, the initial FRET value for the ssDNA in solution is close to the value reported in a previous FRET study on single-stranded DNA conformational flexibility [125]. In Figure 3.3C, the FRET efficiency E decreased gradually from ~ 0.7 to ~ 0 as the force increased, demonstrating force-induced, progressive unraveling of the ssDNA from SSB as we observed in Figure 3.2D. Blue arrows indicate SSB rebinding events. With 20 nM SSB tetramers in solution, once the force was reduced, E returned to 0.7 within our time resolution (~ 44 ms). However, with 1 nM SSB, E often remained low after force reduction, indicating that the SSB had dissociated at high force but did not immediately rebind. The E vs. force curve in the presumed unbound state resembled that of ssDNA itself.

Having confirmed that the time traces shown in Figure 3.2D indeed represents the initial ssDNA unraveling from a SSB tetramer surface, we calculated the averaged

FRET versus force curve from many obtained molecules in 500 mM Na^+ (Figure 3.4A). We found that ssDNA unravelling begins once the force goes above a threshold of β = 0.9 ± 0.2 pN and the averaged stretching and relaxation curves coincide (Figure 3.4A), indicating that the initial peeling off of ssDNA from the SSB surface below 6 pN of force is reversible. From the averaged FRET vs. force curve for stretching the SSB-bound ssDNA, we can replot the same data in a different presentation of distance vs. force (Figure 3.4B) by converting FRET efficiencies to distance values. The theoretical expression of FRET efficiency, E_{FRET}, is given by $E_{FRET} = 1/\ (1+(R/R_o)^6)$, where R is the donor-accepter separation (or inter-fluorophores distance) and R_o is the Förster radius. R_o for Cy3-Cy5 pair is ~ 6 nm [9,126]. Therefore,

$$R = R_o\left(\frac{1}{E_{FRET}}-1\right)^{\frac{1}{6}} = 6\cdot\left(\frac{1}{E_{FRET}}-1\right)^{\frac{1}{6}}\ \text{nm} \qquad (3.1)$$

Throughout the following discussion, force and distance units are pN and nm respectively. Consequently, the energy is in pN nm. We can further define a variable, the ssDNA unraveling distance D, as the distance change in Cy3-Cy5 separation caused by the ssDNA unraveling from the protein surface. Assuming the initial donor-accepter separation for the fully wrapped state is D_0, then

$$D = R\text{-}D_0 \qquad (3.2)$$

The change in the distance between Cy3 and Cy5 estimated from FRET efficiency, D, scales linearly with force, F, within the FRET detectable range with a slope of α = 1.0 ± 0.03 pN/nm (Figure 3.4B). We have

$$D= \alpha\cdot(F\text{-}\beta) \quad (\text{when } F \geq \beta) \qquad (3.3)$$

where α = 1.0 ± 0.03 nm/pN, β = 0.9 ± 0.2 pN for 500 mM Na^+. The unraveling experiment performed at a different ionic condition (5 mM Mg^{2+} and 100 mM Na^+) gave a similar result except that α = 0.7± 0.02 nm/pN and β = 1.2 ± 0.3 pN (Figure 3.4).

For estimating the mechanical work, W, performed to reach an unraveling distance D, we have

$$W = \int_0^D F\cdot dD = \int_0^D (\frac{1}{\alpha}D + 0.9)\cdot dD = \frac{1}{2\alpha}\cdot D^2 + \beta\cdot D\ \text{pN nm} \qquad (3.4)$$

However, this work contains two parts: 1) the adsorption energy, E_{ads}, contributed by the interaction between the protein surface and a ssDNA of a contour length L, which we assume is equally distributed along the ssDNA bound to SSB, i.e. $E_{ads} = \varepsilon_{ads} \cdot L$, where ε_{ads} is the adsorption energy density; and 2) the energy stored in the ssDNA segment that has been unraveled from the protein surface, E_{DNA}. The first energy gives the adsorption energy of SSB-DNA complex so it is more specific to the protein-DNA interaction whereas the second term is a property of the ssDNA itself. In order to estimate the adsorption energy, we consider a regime where the ssDNA has been unraveled by an infinitely small amount, i.e. $D \to 0$ and $F \to \beta$. We define L as the total contour length of two end ssDNA segments that has been unraveled from the protein surface (Figure 3.4C). We can show that $D \approx L$ in the small D region by making two reasonable assumptions:

1) When the two end segments of ssDNA stays bound to SSB, they have their total length close to the contour length L, shown in the above cartoon.
2) After being unraveled, the segments of ssDNA changed their total length from L to x as unbound/bare ssDNA. When the applied force is small, using worm-like chain (WLC) model to estimate [127], the applied force, F, required to induce an end-to-end distance extension of x in a ssDNA of contour length L is given by $F = \frac{3k_BT}{2P}\left(\frac{x}{L}\right)$, where P, the persistence length of ssDNA, is very small (~ 1 nm in 150 mM NaCl and even smaller at higher salt concentrations) compared with that of dsDNA (~50 nm)[18]. At room temperature $k_BT = 4$ pN nm, we have $x = \frac{2P \cdot F \cdot L}{3k_BT} = \frac{F \cdot L}{8}$ if using $P \sim 1$ nm for estimation. When $F \to \beta$ and β=~1 pN, $x \to \beta \cdot L/8 \approx 0.1 \cdot L$ At higher ionic strength (500 mM Na^+), x should be even smaller and WLC tends to overestimate the end-to-end extension of ssDNA[4]. For example, in 5 mM Mg^{2+} buffer , at a force of ~ 0.9 pN the extension x is $\sim 0.03 \cdot L$ estimated from Figure 2 in Ref. [127]. Therefore, x is negligible compared with L in 500 mM Na^+. But this approximation becomes not as good as at decreased ionic strength.

From the discussion above, we show that $D \approx L$ is a good approximation for infinitely small D at high ionic strength. So W can be rewritten by

$$W \approx \frac{1}{2\alpha} \cdot L^2 + \beta \cdot L \qquad (3.5)$$

The linear term is dominant compared with the second order term when L is small, so we have $W \approx \beta \cdot L$. Here, this dominant linear term represents E_{ads}, while E_{DNA} can be expressed from higher order terms. The contour length of ssDNA is 0.58 nm/nt [18], so $\varepsilon_{ads} = \beta = 0.9 \pm 0.2$ pN = 0.22 ± 0.05 k_BT/nm = 0.13 ± 0.03 k_BT/nt for 500 mM Na^+, and ε_{ads} = 1.2 ± 0.3 pN = 0.29 ± 0.07 k_BT/nm = 0.17 ± 0.04 k_BT/nt for 5 mM Mg^{2+} and 100 mM Na^+. This SSB/DNA interaction energy density is smaller than that between nucleosomal DNA and a histone octamer (0.5 -1.0 k_BT/nm) [128,129], potentially explaining the more rapid diffusion for SSB.

3.2.2 SSB Dissociation Events at Higher Forces

If a maximum force of ~13 pN was reached, hysteresis was often observed (Figures 3.5A and 2B) where the initial return segment resembled that observed for ssDNA alone (Figure 3.3B), indicating that the SSB had dissociated fully at this higher force and did not immediately rebind. The averaged stretching and relaxation curves did not overlap and displayed hysteresis due to suppression of rebinding at high forces (Figure 2C), further indicating that full SSB dissociation occurs mainly at forces between 6 and 13 pN.

To determine precisely the force at which SSB dissociates, we repeated the same experiment, but using 1 nM SSB_f, an A122C SSB mutant labeled with ~ one Alexa555 per SSB tetramer[124]. Cy3 was used to locate the tethered DNA and then photobleached before the asymmetric force cycles were initiated. Alexa555 fluorescence becomes observable only upon SSB_f binding to the DNA because proteins free in solution contribute only to the overall background fluorescence. Alexa555 fluorescence increases abruptly upon SSB_f binding to the DNA and disappears later due to either SSB_f dissociation or photobleaching (Figures 3.6A and 3.6B, green trace). The same types of events but monitored by FRET were seen if Cy5 is still active (Figures 3.6D and 3.6E).

Similar force-induced fluorescence disappearance events were observed at twice the stage moving speed (Figures 3.6C and 3.6F).

From many SSB dissociation events, we could build a dissociation force histograms (Figures 3.7A and 3.7B). Beside the dominant peak centered at higher force (9-10 pN), an additional low force peak was found. The number N reflects the total events recorded including both dye photobleaching and SSB dissociation. The photobleaching of fluorophores follows an exponential decay [130] and most of the stretching cycle at the constant stage-moving speed was spent at low forces. The dominant peak did not shift very much upon doubling the pulling speed and the unraveling data in Figure 2 showed that SSB does not dissociate at these low forces. We hence attribute the additional peak in the low force region to photobleaching of fluorophores.

The probability distribution $p(F_d)$ was obtained (Figure 3.7D) after removing the population at low force (~ 1 pN) that we attribute to photobleaching. $p(F_d)$ is broad and asymmetric, and the mean F_d shifted from 8.8±0.2 to 9.5±0.2 pN upon doubling the pulling rate $\boldsymbol{v}$ (Figures 3.7D), indicating that the final SSB dissociation from a partially wrapped intermediate [131] is a non-equilibrium process. We used the theory of Dudko *et al* [132-134] to obtain the rate of SSB dissociation from the partially wrapped intermediate at zero force, $k_{-1} = 0.010 \pm 0.006\ \mathrm{s}^{-1}$; the distance to the transition state from the intermediate, $\Delta x^{\ddagger} = 3.2 \pm 0.5$ nm; and the height of the free energy barrier between the intermediate and unbound state $\Delta G^{\ddagger} = (11 \pm 2)\ k_B T$ (Experimental Procedures). Similar results were obtained in 5 mM Mg^{2+} and 100 mM Na^{+} (Figure 2H) with mean F_d = 10.7±0.3 pN, $k_{-1} = 0.010 \pm 0.005\ \mathrm{s}^{-1}$, $\Delta x^{\ddagger} = 2.4 \pm 0.3$ nm, and $\Delta G^{\ddagger} = (8.0 \pm 0.3)\ k_B T$, Combining our data both at low (< 6 pN) and high force ranges (> 6 pN), the overall energy landscape can be stitched together with two major regions along the dissociation reaction coordinate (Figure 3.8).

3.3 Conclusions

Our data suggest that DNA unravels from SSB in two distinct stages (Figure 2G). Under moderate tension DNA is peeled off from SSB gradually at near equilibrium with a uniform SSB/DNA interaction energy density of 0.1-0.2 k_BT per nt, followed by complete dissociation at higher tension (~10 pN) that involves a large energy barrier (11 k_BT for 500 mM Na^+, 8 k_BT for 5 mM Mg^{2+} and 100 mM Na^+). The partially wrapped intermediate that separates the two regions represents a state where SSB stays bound to the last short stretch of ssDNA before final dissociation. All SIPs tested so far bind SSB via the last 8-10 amino acids in the unstructured SSB-Ct [117]. After the initial binding to an SSB-Ct, the resulting high local concentration of a SIP and the unwrapping of ssDNA at moderate tension may allow progressive ssDNA transfer from SSB to the SIP while avoiding the exposure of the ssDNA region to nucleases.

3.4 Experimental Procedures

DNA Sequences and Annealing Procedures

1. 5'- /biotin/ TGG CGA CGG CAG CGA GGC /Cy5/ - 3'
2. 5'-/5Phos/ GGG CGG CGA CCT T /iAmMC6T/ $(T)_{68}$ GCC TCG CTG CCG TCG CCA - 3'
3. 5’-AGG TCG CCG CCC TTT /digoxigenin/-3’

The sequence in red is the 12 nt cohesive end site of phage lambda DNA. The amine-modified thymine (iAmMC6T) shown in the sequence enables the oligonucleotides to be labeled with the monofunctional NHS ester form of Cy3 or Cy5 dyes (GE Healthcare). Otherwise, Cy3 or Cy5 dye was attached directly to the DNA backbone using phosphoramidite chemistry.

The partial duplex DNA substrates (18 bp dsDNA) with poly(T) single-stranded tails carrying fluorescence dyes were annealed by mixing ~5µM of biotinylated strand and ~7 µM of poly(T) strand in 10 mM Tris:HCl (pH 8.0) and 50mM NaCl followed by slow cooling from 90°C to room temperature for ~ 2 hours. λ-DNA (Promega) was then attached to the pre-annealed partial duplex DNA by following the protocol described previously[100]. Subsequently, the digoxigenin-labeled oligonucleotide complementary to the cohesive end site of λ-DNA was added (5’-AGG TCG CCG CCC TTT /digoxigenin/-3’). This produced the complete DNA template, which was labeled with a single dig tag on one end and a biotin tag on the other end.

Protein Purification, Characterization and Labeling

E. coli SSB [135] and SSB mutant (A122C labelled with ~ one Alexa555 per SSB tetramer) [124] were purified as described.

Fluorescence-Force Spectroscopy Instrument

The combined optical trapping and single-molecule confocal fluorescence instrument was built as previously described in Chapter 2. Briefly, the trapping laser beam was coupled through the back port of the microscope, while the fluorescence excitation laser beam (532 nm, 30 mW, World StarTech) was directionally controlled by a two-dimensional piezo-controlled steering mirror (S-334K.2SL, Physik Instrument) and coupled through the right side port. The fluorescence emission was isolated from the reflected infrared light (F3: HNPF-1064.0-1.0, Kaiser) and was band-pass filtered (F1: HQ580/60m, F2: HQ680/60m, Chroma) before being imaged onto two avalanche photodiodes. The bright-field image of the trapped bead was obtained using a CCD camera (GW-902H, Genwac). Two dimensional calibration of the QPD (UDT SPOT/9DMI) over the full detector range and trap stiffness determination were performed as described in Chapter 2.

Sample Assembly

For fluorescence-force measurements, about 10-50 pM of the complete DNA templates were immobilized on a coverslip surface which is coated with polyethyleneglycol (mPEG-SC, Laysan Bio) in order to eliminate nonspecific surface adsorption of proteins and reduce the surface interactions with DNA and beads [9,126]. The immobilization was mediated by biotin-Neutravidin binding between biotinylated DNA, Neutravidin (Pierce), and biotinylated polymer (Bio-PEG-SC, Laysan Bio). Next anti-digoxigenin-coated 1 μm polystyrene beads (Polysciences) were added so that one bead can attach to the free end of each tethered DNA. Finally, 1 nM or 20 nM of SSB protein was added in an imaging buffer containing 500 mM NaCl (or 5 mM $MgCl_2$, 100 mM NaCl), 20 mM Tris:HCl (pH8.0), 0.1mM EDTA, 0.5mg/ml BSA(New England Biolabs), 0.01 mg/ml anti-digoxigenin, 0.5 % (wt/vol) D-glucose (Sigma), 165 U/ml glucose oxidase (Sigma), 2170 U/ml catalase (Roche), 3 mM Trolox (Sigma), and 0.1% (vol/vol) Tween 20 (Sigma).

Single-Molecule Data Acquisition

All single molecule measurements were performed at 22 ± 1°C. For fluorescence-force measurements, once a tethered bead was trapped, the coverslip was moved back and forth with the piezo-stage to roughly determine the tethered position by finding the central position of the stretching curves in two orthogonal directions in the sample plane. The origin of the piezo stage was then reset to this central position. Next a more accurate position of the fluorescently labeled molecule was determined by displacing the molecule by 13 μm from the trap center and taking a confocal image around the tethered position. For the SSB dissociation experiment, the piezo-stage was then moved back and forth between a starting position (typically 13-14 μm separation between the tethered point and the trap center) to an end position (16.5 -16.8 μm separation between the tethered point and the trap center) at a constant stage-moving speed (455 or 910 nm s^{-1}) for several force cycles. The confocal excitation beam was programmed to follow the motion of the molecule so that in the meantime we were able to record the donor and acceptor fluorescence intensities with 44ms time resolution as the applied force ramped up. To obtain the averaged FRET vs. force curve, averaging was done over 30-50 cycles from 10-20 molecules using a force bin size of 0.2 pN. To test the force dependence of the SSB diffusion rates, the stage was sequentially moved to five different positions. At different constant forces, single-molecule fluorescence signals were collected for 6 s with 10 ms time resolution. For force-free smFRET experiments, the confocal microscope in the combined setup or a TIR microscope was used and single-molecule FRET histograms were generated by averaging for 300 ms.

Dissociation Force Distributions

Unfolding force distributions were created by reading out the corresponding force value for the SSB dissociation event indicated by fluorescence. The two distributions obtained in 500 mM Na^+ with different pulling speeds were fit to the non-equilibrium model of Dudko *et al* [132].

$$p(F) \propto \frac{k(F)}{r} \exp\left\{ \frac{k_{-1}}{\Delta x^{\ddagger} r} - \frac{k(F)}{\Delta x^{\ddagger} r} \left(1 - \frac{\Delta x^{\ddagger} F}{\Delta G^{\ddagger}} \mu \right)^{1-\frac{1}{\mu}} \right\}$$

where $$k(F) = k_{-1} \left(1 - \frac{\Delta x^{\ddagger} F}{\Delta G^{\ddagger}} \mu \right)^{\frac{1}{\mu}-1} \exp\left\{ \Delta G^{\ddagger} \left[1 - \left(1 - \frac{\Delta x^{\ddagger} F}{\Delta G^{\ddagger}} \mu \right)^{\frac{1}{\mu}} \right] \right\},$$

r is the loading rate, k_{-1} is the SSB dissociation rate from the partially wrapped intermediate at zero force, $\Delta x^{\ddagger}$ is the distance to the transition state from the intermediate; and $\Delta G^{\ddagger}$ is the height of the energy barrier between the intermediate and unwrapped state, and μ is a parameter characterizing the shape of the energy barrier. We found the fitting results to be insensitive to the absolute values of the two loading rates but sensitive to the ratio between the two. Shifting the loading rate values by 10 % (the ratio maintains at 1:2) caused a shift of less than 1% in the fitted values of the three parameters. Considering that the majority of the dissociation events happened in a short span between 5 and 13 pN and the contour length of the DNA tether is very long, the loading rates can be treated as constant to a good approximation [133]. We therefore performed a linear fit to the force-time curve in the range of 5-13 pN to determine the approximate loading rates for the two pulling speeds. We used two values of v to fit the force distributions and the fitting was performed globally between the two dissociation force distributions with three shared parameters k_{-1}, $\Delta x^{\ddagger}$ and $\Delta G^{\ddagger}$. We obtained $k_{-1} = 0.010 \pm 0.007\ \mathrm{s}^{-1}$, $\Delta x^{\ddagger}=3.4 \pm 0.7$ nm., and $\Delta G^{\ddagger} = (12 \pm 3)\ k_{\mathrm{B}}T$ for a sharp, cusp-like energy barrier ($\mu = 1/2$), whereas $k_{-1} = 0.010 \pm 0.006\ \mathrm{s}^{-1}$, $\Delta x^{\ddagger} = 3.2 \pm 0.5$ nm, and $\Delta G^{\ddagger} = (11 \pm 2)\ k_{\mathrm{B}}T$ for a softer, cubic potential ($\mu = 2/3$).

3.5 Figures

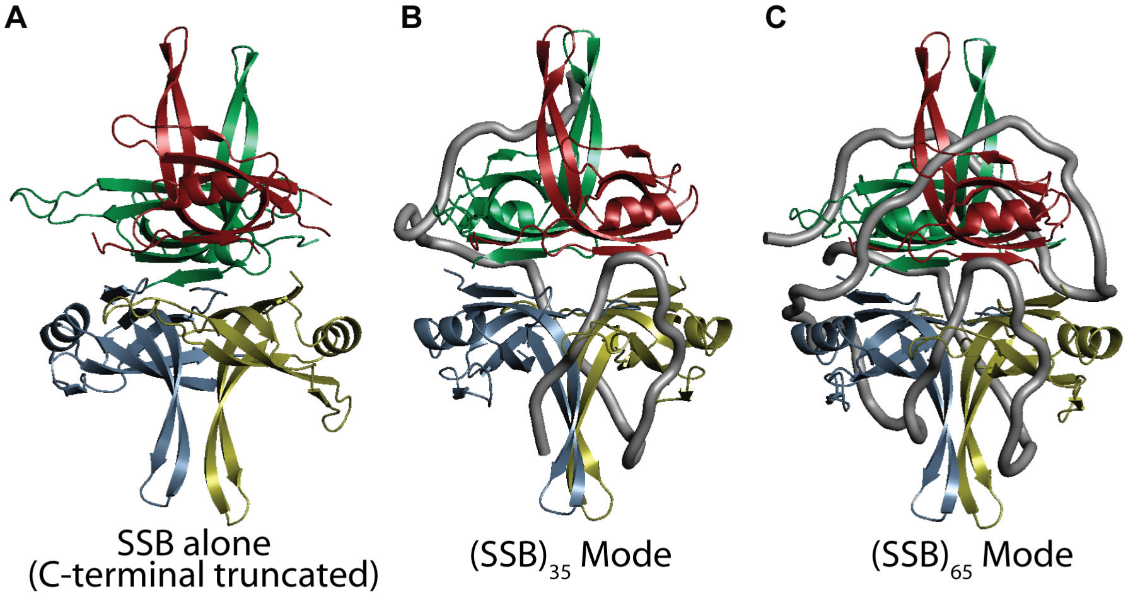

Figure 3.1 (A) a cystal structure of a C-terminal truncated SSB tetramer (SSBΔC) [119]. (B and C) Structural model for an SSB tetramer bound to a stretch of ssDNA (thick gray line) in the $(SSB)_{35}$ binding mode and fully wrapped $(SSB)_{65}$ binding mode respectively, based on an X-ray crystallographic structure of a C-terminal truncated SSB tetramer (SSBΔC) bound to two $(dC)_{35}$ oligonucleotides [118].

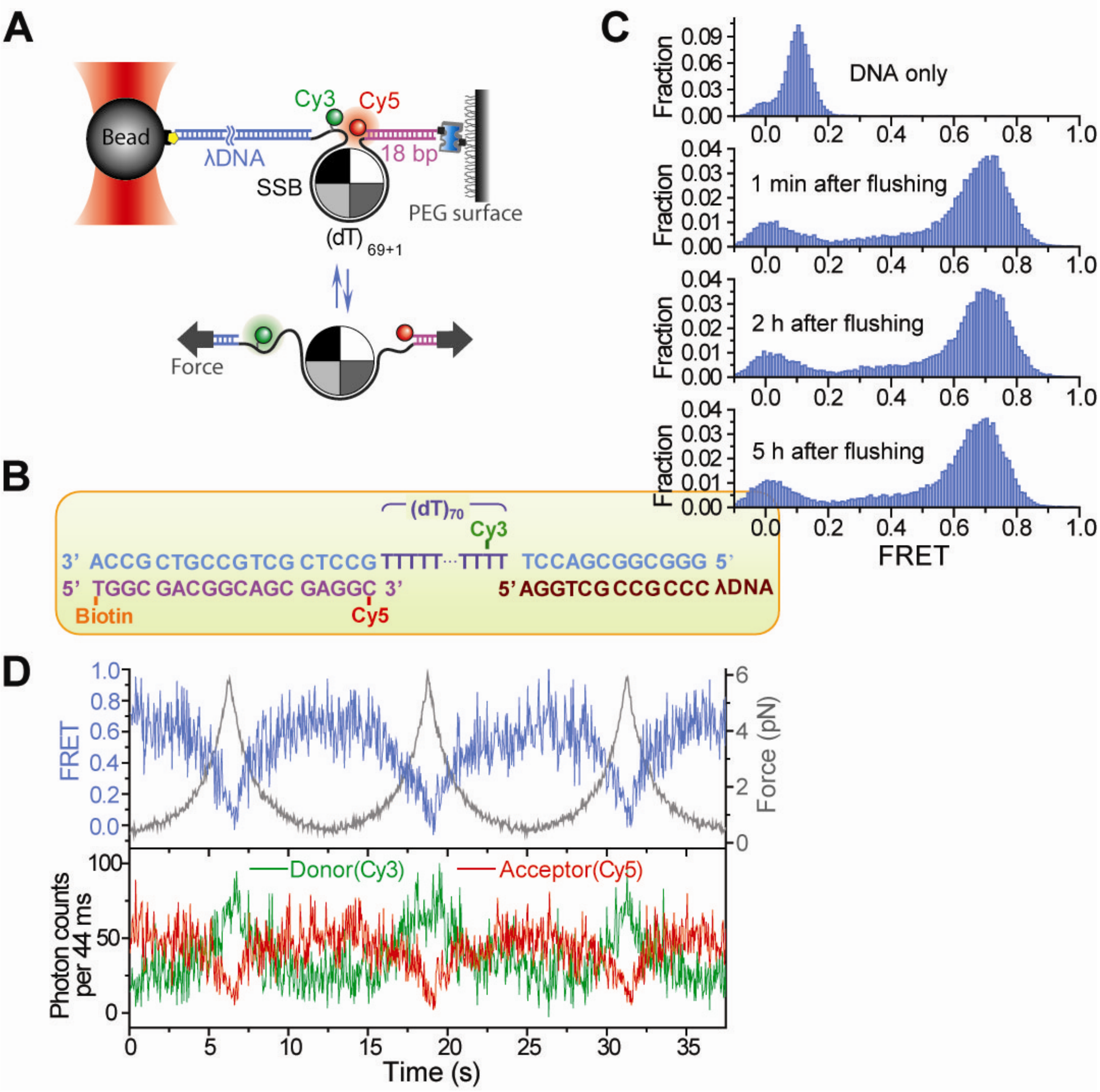

Figure 3.2 Force-induced Unraveling of ssDNA from SSB Measured by Fluorescence-Force Spectroscopy. (A) Experimental scheme for force-induced unravelling of ssDNA, (dT)$_{69+1}$, from SSB measured via FRET. One end of the construct was immobilized on a PEG surface via biotin-neutravidin interaction and the other end was linked to a bead held in an optical trap via a Digoxigenin-Anti-digoxigenin interaction. (B) DNA template used for the unravelling experiment showing the fluorescent labeling and the annealing geometry to λ DNA. The (dT)$_{70}$ in purple represents the ssDNA part. (C) FRET histograms of the DNA construct at zero force with and without SSB bound. The peak at zero FRET corresponds to DNA molecules with active Cy3 only, and the second major peak corresponds to DNA molecules with both active Cy3 and Cy5. Excess SSB proteins

were removed from the solution after incubating at 500 mM NaCl and 1 nM SSB tetramer concentration. The FRET histograms were obtained 1 minute, 2 hours, and 5 hours after the removal of free SSB in solution. (D) Fluorescence-force traces obtained while stretching and relaxing the DNA at the stage-moving speed *v* of 455 nm s^{-1} (20 nM SSB in solution) when the maximum force achieved was set to ~ 6 pN (Averaged among ~ 50 cycles from 10 molecules with a bin size of 0.2 pN).

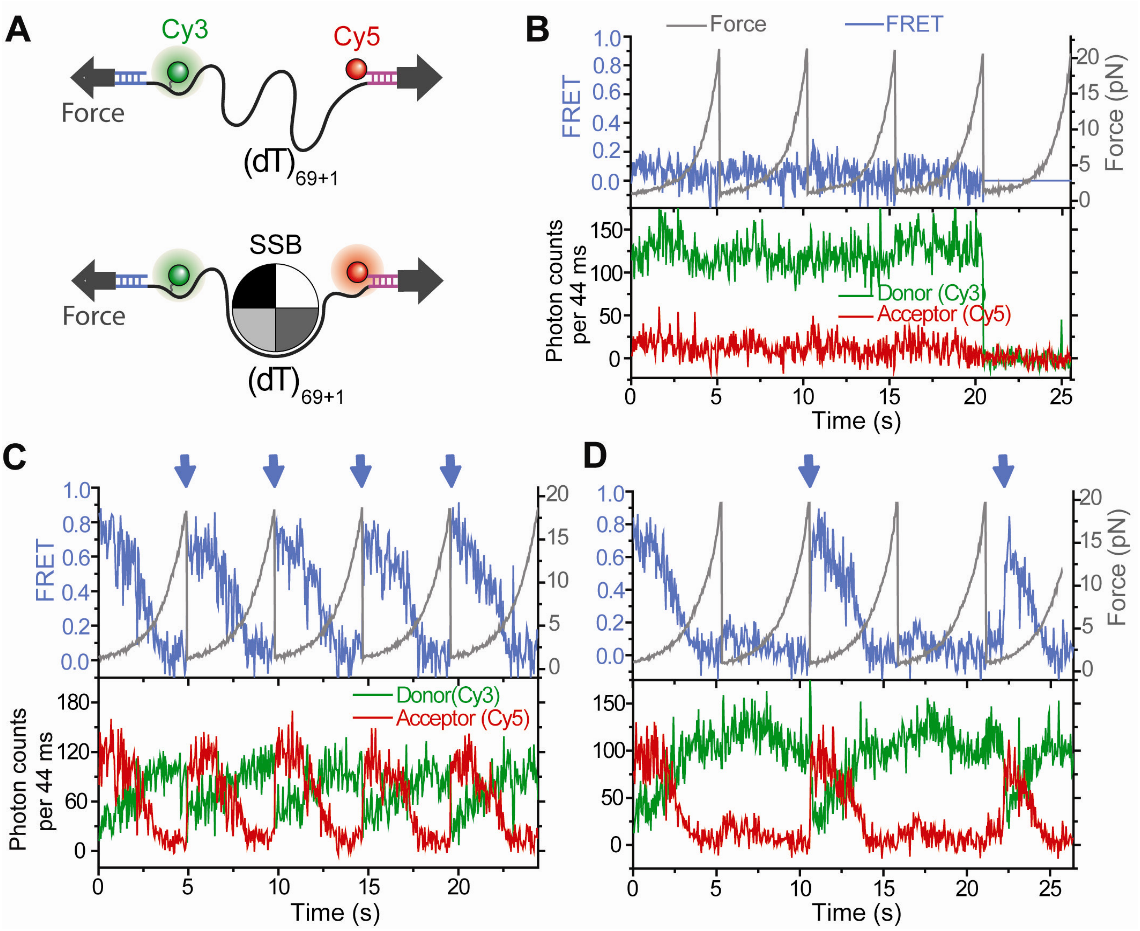

Figure 3.3 Unraveling ssDNA from an SSB tetramer. (A) Experimental scheme to stretch a 70-mer ssDNA with Cy3 and Cy5 separated by 68 nts of the ssDNA region. (B-D) Force-fluorescence traces at a SSB tetramer concentration of 0 (B), 20 (C), or 1 (D) nM SSB.

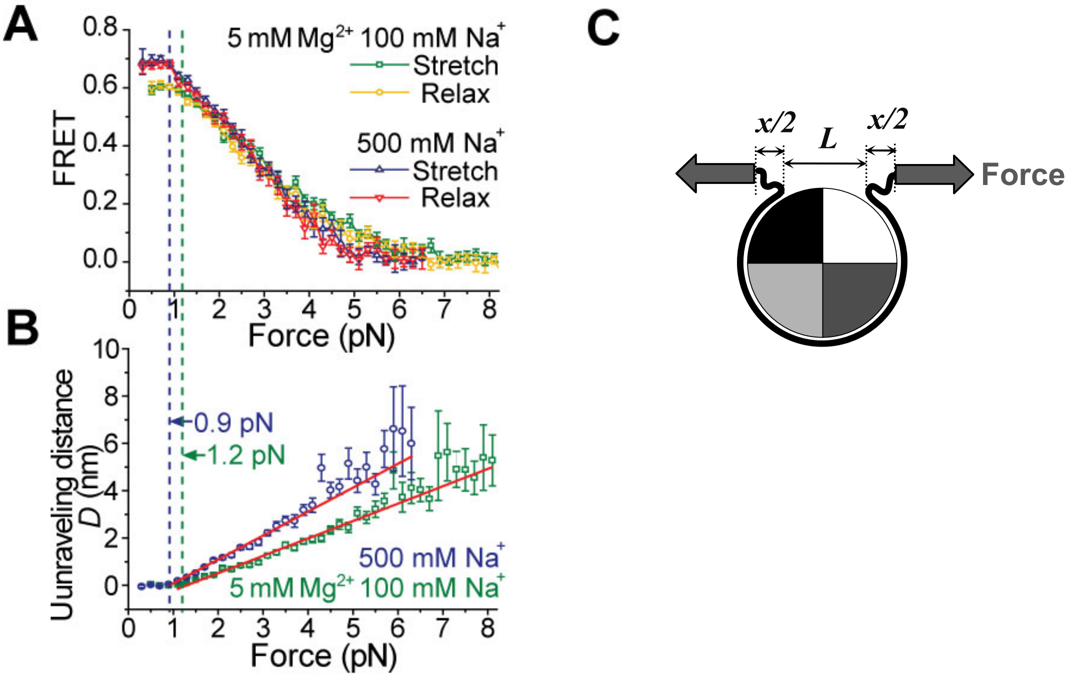

Figure 3.4 (A) The averaged FRET vs. force curves for stretching and relaxing the DNA when the maximum force achieved was set to ~ 6 pN (in 500 mM Na^+) or ~8 pN (in 5 mM Mg^{2+} and 100 mM Na^+). (B) Unraveling distance vs. force curves in two ionic conditions fit to straight lines (red lines), $D = \alpha \cdot (F - \beta)$ (when the force $F \geq \beta$), where α = 1.0 ± 0.03 nm/pN, β = 0.9 ± 0.2 pN for 500 mM Na^+, and α = 0.7± 0.02 nm/pN, β = 1.2 ± 0.3 pN for 5 mM Mg^{2+} and 100 mM Na^+, determined from the fit Error bars are the standard errors. (C) The cartoon illustrates when a force is applied, two end segment of SSB-bound DNA are unraveled from the protein surface. The black thick curve presents the ssDNA. We define L as the total contour length of the two end ssDNA segments that have been unraveled from the protein surface, and $x/2$ as the end-to-end extension of each ssDNA segment unraveled.

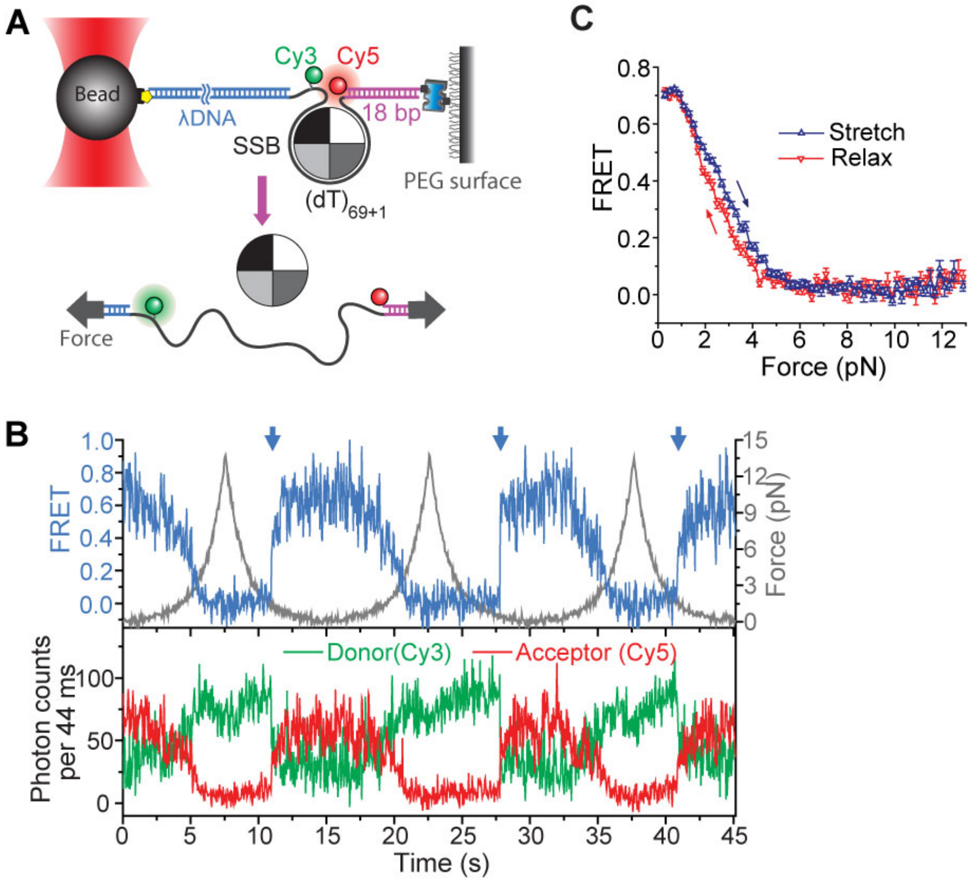

Figure 3.5 (A) Experimental scheme for force-induced unravelling of ssDNA, (dT)$_{69+1}$, from SSB measured via FRET as in Figure 3.2D. (B) Fluorescence-force traces obtained while stretching and relaxing the DNA at the stage-moving speed v of 455 nm s^{-1} (20 nM SSB in solution) when the maximum force achieved was set to ~ 13 pN (in 500 mM Na^{+}). Blue arrows indicate SSB binding events. (C) The averaged FRET vs. force curves for stretching and relaxing the DNA when the maximum force achieved was set to ~ 13 pN. Error bars are ± s.e.m. (Averaged among 45 cycles from 12 molecules with a bin size of 0.2 pN).

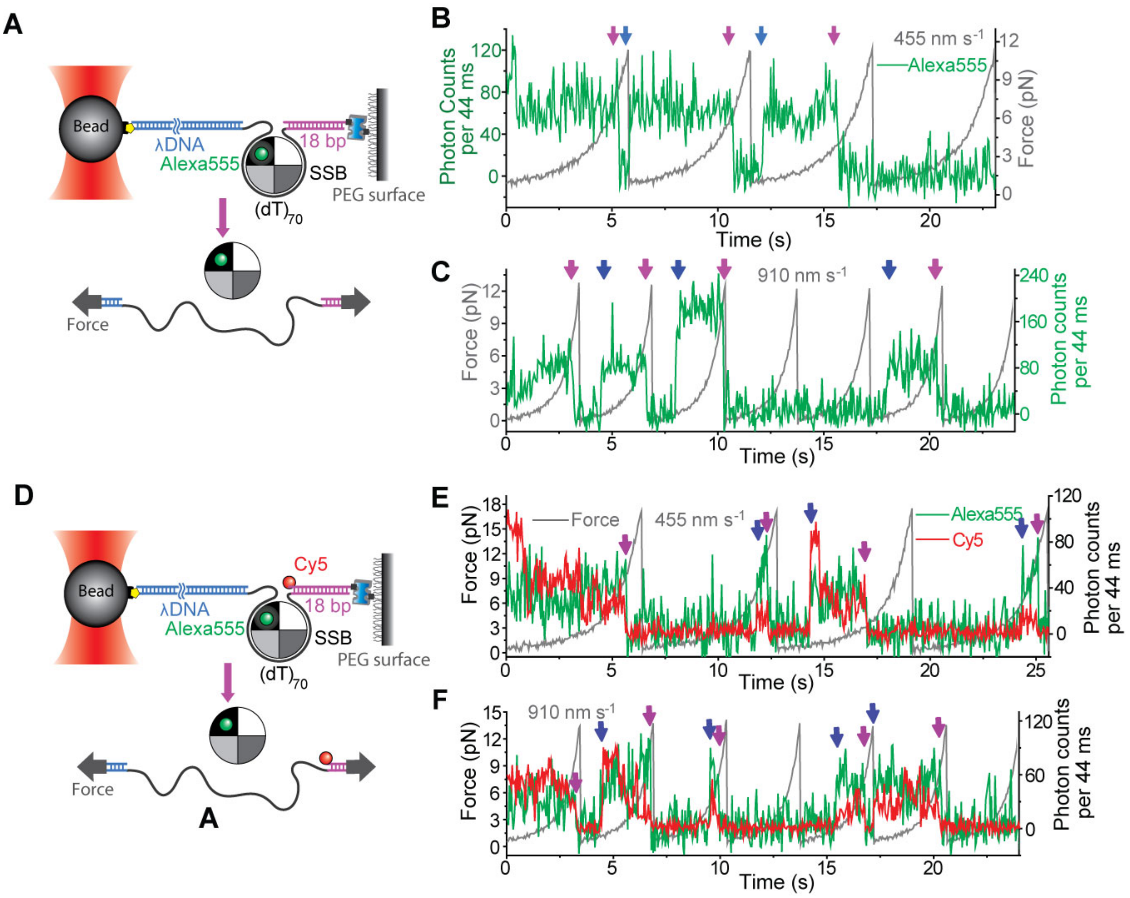

Figure 3.6 (A-C) Experimental scheme and force-fluorescence curves that indicate the binding and dissociation of individual Alexa555-labeled SSB (SSB$_{f}$) at a stage-moving speed of 455 (B) or 910 (C) nm s^{-1}. Similar force-induced fluorescence disappearance events were observed as seen at a stage-moving speed of 455 nm s^{-1}. Blue and magenta arrows represent SSB binding and dissociation events respectively. (C-E) Experimental scheme and force-fluorescence curves that indicate the binding and dissociation of individual SSB$_{f}$ with active Cy5 at a stage-moving speed of 455 (D) or 910 (E) nm s^{-1}. When Cy5 labeled on the DNA duplex junction is active, fluorescence signals appear both in donor and acceptor channels upon SSB$_{f}$ binding (blue arrows), further suggesting the abrupt fluorescence appearance events observed were not caused by non-specific binding of SSB$_{f}$ to the surface. The sudden disappearance of fluorescence signal in both detection channels represents SSB$_{f}$ dissociation or donor photobleaching events (magenta arrows).

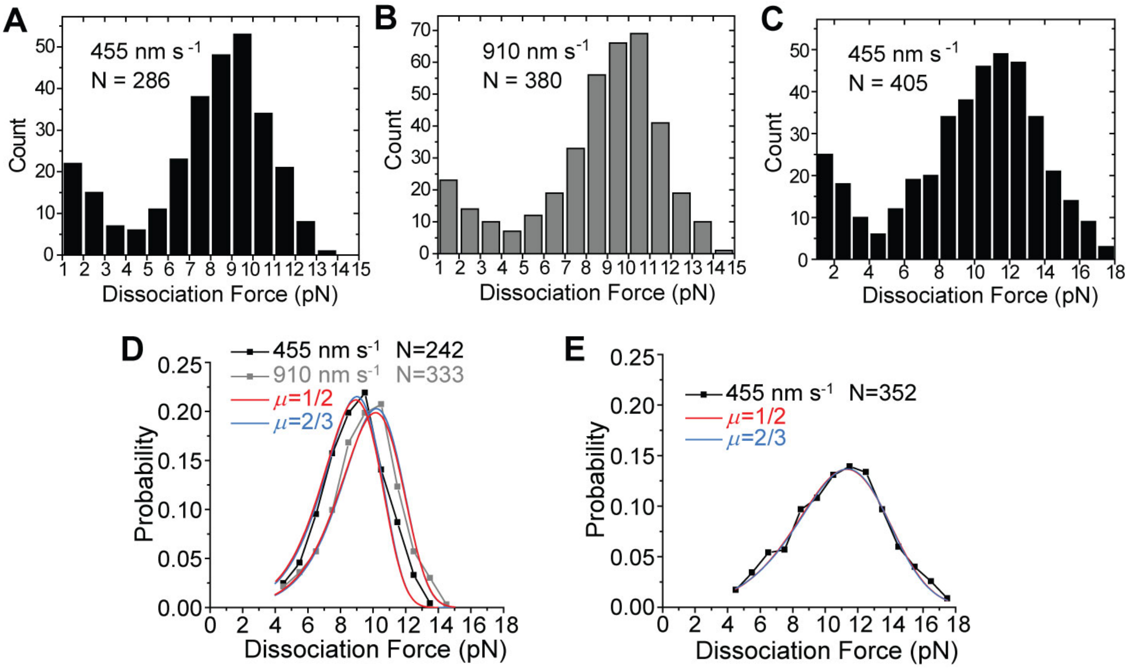

Figure 3.7 (A and B) The dissociation force histograms obtained in 500 mM Na$^+$ at the stage-moving speed of 455 (A) or 910 (B) nm s^{-1}. (C) The dissociation force histogram obtained in 5 mM Mg^{2+} and 100 mM Na$^+$ at the stage-moving speed of 455 nm s^{-1}. In contrast to the previous work where a force-fluorescence combined scheme was used [136], our method has the single protein resolution so that we can differentiate some part of photobeaching events from protein dissociation events. This reduces the influence of the fluorophore photobleaching in counting the protein dissociation events because the photobleaching population outside the time window of the protein dissociation events can be removed as shown above. (D) Dissociation force distributions obtained in 500 mM Na$^+$ at the two stage-moving speeds. The small population assigned to fluorophore photobleaching has been removed. The solid lines are the global fits to the Dudko model with the parameter (μ) that controls the shape of the energy barrier set to 1/2 (blue) or 2/3 (red) (see Experimental Procedures). (E) Dissociation force distribution obtained in 5 mM Mg^{2+} and 100 mM Na$^+$ at the stage-moving speed of 455 nm s^{-1}.

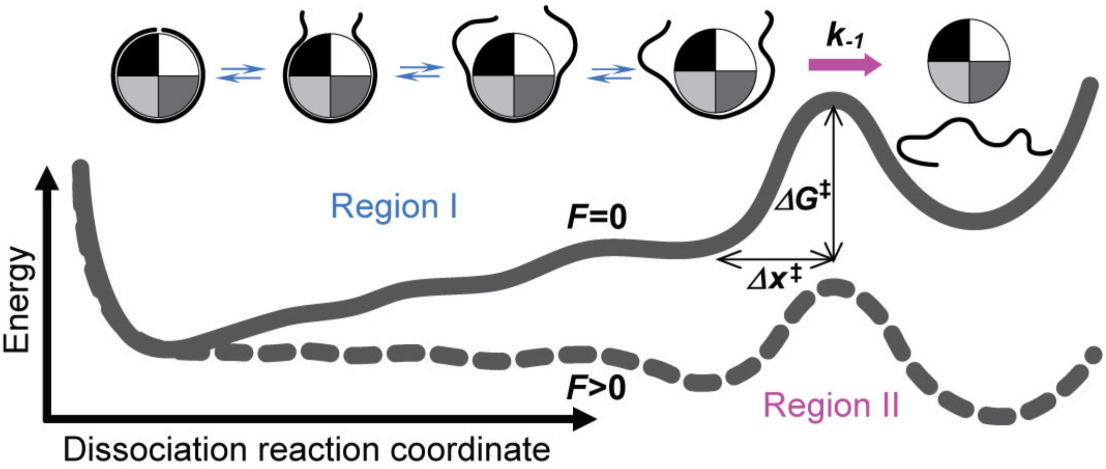

Figure 3.8 Energy landscape along the SSB dissociation reaction coordinate with two distinct regions: 1) gradual peeling off of SSB-bound ssDNA from SSB tetramer surface and 2) Final dissociation of SSB that needs overcome a high energy barrier.

Chapter 4
Probing Protein Diffusion Mechanism on Single-Stranded DNA[§]

4.1 Introduction

The process by which protein diffusion along DNA facilitates location of specific target sites or its repositioning has been studied almost exclusively on double-stranded DNA [137]. Recently, we reported the direct observation of a protein diffusing on ssDNA [124]. Using single molecule two- and three-color FRET (fluorescence resonance energy transfer [10]), we found that *Eco*SSB can diffuse on ssDNA (diffusion coefficient ~300 nt^2/s at 37 ºC) with a mean step size of 3 nt, and that this SSB activity transiently melts DNA secondary structures and stimulates RecA filament elongation [124]. The underlying mechanism for diffusion is fundamental to understanding cellular functions but how a protein with such a large binding site size (~65 nt for SSB) and high affinity can diffuse spontaneously and rapidly on DNA remains unknown. In addition, how the application of force or the binding of SIPs might modulate these SSB dynamics has not been investigated.

Here, we apply fluorescence-force spectroscopy described in Chapter 2 to monitor the tension-dependent conformational transitions of DNA/protein complexes with nanometer resolution at the single protein level. Our earlier study on SSB [124] was based on only fluorescence measurements. Here, with tension applied to the DNA and our unique capability to measure temporal changes of arbitrary coordinates (i.e., not just the end-to-end distance of a biopolymer) at low forces, we were able to obtain unique information that is unattainable by mechanical manipulations or fluorescence techniques alone. The fluorescence probes can be positioned at different desired locations on DNA and/or protein to probe the dynamics along various vectors, which maximizes the information content. This approach allowed us to directly observe the mechanical

---

[§] The work in this chapter has been published as a paper:
Zhou, R. et al. SSB Functions as a Sliding Platform that Migrates on DNA via Reptation. *Cell* **146**, 222-232 (2011)

regulation of an individual SSB tetramer diffusing along ssDNA. In addition, we also applied single molecule FRET together with fluorescence-force spectroscopy to probe SSB diffusion mechanism.

4.2 Probing SSB Diffusion Mechanism

4.2.1 Rolling vs. Sliding Mechanisms for SSB Diffusion on DNA

At present, there is only one proposed mechanism in the literature on how SSB may achieve this feat [138,139]. In this rolling mechanism, a partial unwrapping of one end segment of ssDNA from an SSB tetramer is followed by rewrapping of the other end of the ssDNA in its place, resulting in a one-dimensional random walk of SSB along DNA (Figure 4.1A). The rolling mechanism utilizes the closed wrapping of ssDNA on the SSB surface and allows SSB diffusion while maintaining most of its contacts with ssDNA (with relatively low energetic cost), and is therefore an attractive mechanism. An alternative scenario that has not been previously considered for SSB is that the whole ssDNA 'slides' relative to the protein surface (Figure 4.1B).

To distinguish between 'rolling' and 'sliding', we performed smFRET experiments with Alexa555-labeled SSB (SSB_f) and DNA constructs with Cy5 attached to either the end (Figure 4.1C, Scheme 1) or the mid-section (Figure 4.1D, Scheme 2) of $(dT)_{70}$ ssDNA. In rolling, only the end segments of the ssDNA would display motion relative to SSB while the mid-section of bound ssDNA would not because the 70 nt ssDNA is only slightly longer than the SSB binding site. Therefore, Scheme 2 should show FRET fluctuations for sliding due to the change in the distance between Alexa555 and Cy5 (Figure 4.1B), but not for rolling (Figure 4.1A). FRET time traces for both schemes show fluctuations of similar amplitudes (Figures 4.1C and 4.1D), strongly supporting the sliding model in which the whole SSB-bound ssDNA moves relative to the SSB surface during diffusion. Plotting the mean FRET efficiency of each molecule, $<E>$, versus its standard deviation over time, σ_E, (Figure 4.1E) revealed no significant differences in the amplitude of FRET fluctuations between the two labelling schemes, further indicating that sliding is likely the dominant mechanism and that contributions from rolling, if any, must be much smaller. To quantify the diffusion time scale in each case, we calculated the cross-correlation function between Cy3 and Cy5 intensity-time traces. The diffusion-induced fluctuation time scales were 117 ± 3 ms for Scheme 1 and 301 ± 22 ms for Scheme 2 obtained from single-exponential fits to the cross-correlation of I_D and I_A (Figure 4.1F and Experimental Procedures in this chapter).

Besides Schemes 1 and 2, we also tested the other two labeling schemes (Schemes 3 and 4) for $SSB_f/(dT)_{70}$ where Cy5 was instead positioned either 16 or 70 nt away from one end of the ssDNA $(dT)_{70}$ (in Schemes 1 and 2, Cy5 was positioned either 0 or 35 nt away from one end of the $(dT)_{70}$ respectively). In Figure 4.2, we plot the normalized cross-correlation functions of I_D and I_A for all the four labeling schemes. The scatter plot of $<E>$ versus σ_E for individual FRET time trajectories obtained from Schemes 3 and 4 shows the similar result as we observed for Schemes 1 and 2 (Figure 4.2C).

In order to further test that the FRET fluctuations observed are due to SSB diffusion on DNA, we first obtained FRET time traces using $(dT)_{40}$ and $(dT)_{51}$, which are shorter than an SSB tetramer binding site size and therefore are not expected to allow SSB diffusion. Indeed, FRET fluctuations beyond measurement noise were eliminated (Figures 4.2A-C). The cross-correlation of I_D and I_A averaged over >100 molecules showed no significant anti-correlation (Figure 4.3D). Next, we performed a systematic experiment using unlabeled SSB and DNA constructs with ssDNA equal to or shorter than the SSB tetramer binding site size and labelled with Cy3 and Cy5 separated by 16, 31, 41, 50 and 60 nt (Figure 4.4). We did not observe any FRET fluctuations beyond measurement noise, indicating that the FRET fluctuations observed when ssDNA is longer than the binding site size are not due to conformational changes of SSB-bound ssDNA.

As a further test, we applied tension to SSB-bound DNA to disrupt the closed wrapping which is a prerequisite for rolling [124,131]. The diffusion-induced FRET fluctuations persisted even at forces up to ~ 5 pN (Figure 4.5), a force regime where the ssDNA unravelling, as measured by FRET, is essentially complete (Figure 1C). If diffusion on ssDNA indeed does not require closed wrapping, the ability to diffuse on ssDNA may be shared by other ssDNA binding proteins that do not display closed wrapping. This result also supports the sliding mechanism.

4.2.2 Reptation (Sliding-With-Bulge) Mechanism for SSB Diffusion

Having ruled out rolling as a dominant mechanism, how might the sliding of 65 nt of SSB-bound DNA be achieved every time SSB takes a step? There are two general classes of model with different transition or intermediate states between diffusional steps. In one, all of the contacts are broken simultaneously before the protein can slide relative to the DNA to arrive at the adjacent position (Class A, Figure 4.6A). In the other, only a few contacts between the protein and the DNA are broken and then reformed at a time, i.e., all contacts are broken in piecemeal (Class B). An attractive possibility for a Class B model is 'reptation' (Figure 4.6B) where propagation of a defect (or a loop/bulge) in a polymer chain gives rise to an overall translation of the chain [140-142]. A DNA bulge is formed via thermal fluctuations with an excess length ΔL, equivalent to the diffusion step size, which then propagates via a random walk: if the bulge happens to be annihilated at the position where it formed, there will be no net motion, but if it reaches the other end of the SSB-bound DNA, the protein would be repositioned by ΔL [143]. The bulge can form spontaneously if an unwrapped DNA segment is rewrapped but with an offset of size ΔL. Because this would reduce the overall end-to-end length of the DNA tether, an applied force would make such an event less likely to occur, slowing down the reaction. Therefore, the reptation model predicts that increased tension on the DNA will slow down SSB diffusion. One would expect just the opposite for Class A models where the DNA needs to be transiently detached from the protein surface for each step of diffusion because higher forces will make it easier to achieve such a transient state (hence faster diffusion) by reducing the number of contacts between the protein and the DNA via DNA unraveling.

In order to probe if diffusion becomes faster or slower with increasing force, we extended the ssDNA region by 13 nt beyond the 69 nt that separate Cy3 and Cy5 (Figure 6A) and measured FRET at constant forces and at 1 nM SSB and 500 mM Na^+. The anti-correlated fluctuations in I_D and I_A confirm that SSB can diffuse along the ssDNA even under tensions up to ~ 5 pN (Figures 4.7A and 4.7B). The peak of the FRET histogram shifted to a value near zero at the higher (6.5 pN) force (Figure 4.7C) due to ssDNA unwrapping from the protein surface, as was seen from the FRET-Force stretching curve in Chapter 3 (Figure 3.4A). We repeated this experiment in another ionic condition (5 mM Mg^{2+} and 100 mM Na^+) and the result was similar (Figures 4.7E and 4.7F). Importantly, the characteristic time scale for diffusion τ calculated from the cross-correlation curve increased with force F under both ionic conditions that we have investigated (Figures 4.7D and 4.7G). The slower diffusion at higher forces favors the reptation model ('sliding-with-bulge'), over the Class A models ('sliding-without-bulge') as a mechanism for sliding. In addition, the data in Figures 1 and 2 indicate that the energy cost of breaking multitudes of bonds simultaneously between ~65 nt of DNA and the protein surface is $(11 + 0.13 \cdot N)\ k_B T$ (N is the number of nucleotides unraveled before reaching the partially wrapped intermediate) and that an SSB tetramer remains bound to ssDNA in the absence of free SSB for several hours (Figure 3.2C). Therefore, it is highly unlikely that a complete/global dissociation of SSB occurs every time SSB diffuses on ssDNA by each step, further discounting Class A models in favour of the reptation model.

In reptation, to step from one site to the other at zero force, SSB needs to overcome an energy barrier, $\Delta U(0)$ (Figure 4.8), associated with the extra curvature energy for the DNA loop-bulge formation and the adsorption energy of the protein surface and DNA [143].The ragged plateaus in the energy landscape represent the intermediates when a DNA loop-bulge of about 3 nt in extra length is formed, and in this model, we envision that the bulge propagates to either of the two ends rapidly and is then annihilated. The tension, F, applied to the ends of the ssDNA adds an extra mechanical energy penalty ($\sim F\Delta L$) to loop formation, and increases the energy barrier by the same amount, resulting in a force-dependent diffusion time scale.

Why is the force dependence of the diffusion time scale steeper in 5 mM Mg^{2+} and 100 mM Na^+ than in 500 mM Na^+? We obtained FRET histograms of naked ssDNA with Cy3 and Cy5 separated by either $(dT)_{31}$ or $(dT)_{50}$ (Figure 4.9). We observed lower FRET values in 5 mM Mg^{2+} and 100 mM Na^+, suggesting that ssDNA is more extended and the persistence length of ssDNA is larger due to the lower salt concentration [125]. If the minimum bulge size during reptation is limited by the persistence length of ssDNA, one would expect a larger ΔL at lower salt concentrations, resulting in a stronger force dependence.

4.2.3 SSB Interacting with RecO via SSB-Ct Decelerates SSB Diffusion on DNA

Our data thus far show that SSB diffusion on DNA is robust against moderate tension. Would SSB diffusion persist even when bound to SIPs? We examined the effect of RecO, one of the 14 SIPs in *E. coli* [117]. RecO promotes annealing between SSB-coated DNA strands [144] and stimulates RecA loading onto SSB-coated ssDNA [145-149]. RecO is monomeric in solution under our conditions (Experimental Procedures) and binds with 1:1 stoichiometry to each of the four SSB-Cterminal tail (SSB-Ct) but not to SSB without the Ct (Figures 4.11A-C)[145,150]. After forming a stable complex of a single SSB tetramer with $(dT)_{69+8}$, we added RecO to the solution (Figure 4.10A). These FRET histograms (Figure 7B) differed from those observed for DNA/RecO interactions (Figure S6E). FRET fluctuations persisted even with RecO present in solution (Figures 4.10C and 4.10D), indicating that SSB diffusion occurs even with RecO bound to the DNA/SSB complex. However, cross-correlation analysis (Figure 4.10E) showed that RecO binding does slow SSB diffusion and the characteristic time scale of SSB diffusion increased from 50 ± 2 to 77 ± 4 ms at the highest RecO concentration tested. This effect is not merely due to RecO binding to ssDNA [147,150,151] because it is abolished if the SSB/RecO interaction is disrupted by deleting the last 42 amino acid residues from the SSB-Ct [118] (termed SSBΔC; Figure 4.10F). SSBΔC or an 8 amino acid C-terminal truncation of SSB (termed SSBΔC8) displayed the same ssDNA binding features as wild type SSB under these conditions [124,152], but SSBΔC8 does not bind RecO (Figure 4.11B). Because RecO-promoted ssDNA annealing requires Mg^{2+} [151], we repeated our experiment in buffer containing 10 mM Mg^{2+} and 80 mM K^+. Similar diffusion-induced FRET fluctuations were observed in the absence and presence of RecO (Figures 4.11F and 4.11G). Slowing of diffusion was also observed for wild type SSB but not for SSBΔC8 (Figures 4.10G).

4.3 Discussion

4.3.1 Reptation as a Diffusion Mechanism

Our probing of SSB diffusion along ssDNA has provided new insights into the fundamental mechanism of the one-dimensional random walk of proteins on ssDNA. Our data ruled out 'rolling' as a dominant mechanism for SSB diffusion on DNA and suggest that the SSB-bound DNA would 'slide' all together relative to the protein surface during diffusion. Reptation may also offer an explanation for why SSB diffusion may occur with a step size larger than 1 nt [124]. The minimum step size in reptation is constrained by the minimum size of the DNA bulge. Because the persistence length ranges from 1 to 3 nm between 25 mM and 2 M Na^+ [125], a bulge of the minimal size, 1 nt, could be too energetically costly to form. A reptation step size of ~3 nt may also be rationalized by the crystal structure of SSB bound by ssDNA which showed clusters of 2-4 nt in size that bind to specific sites on the protein [118].

The force-dependence data on SSB diffusion (Figure 6) provides direct experimental evidence for a 'reptation' model of protein motion on DNA. Although we have not directly observed bulge formation and propagation, which is presumably too fast to detect, and we have not technically ruled out all other Class B models, reptation (or sliding-with-bulge) is the only model we are aware of that is consistent with all of the data reported here.

4.3.2 Functional Role of SSB Diffusion on DNA

The fact that SSB diffusion along ssDNA was detected with up to 5 pN of tension, even when the SSB-ssDNA structure is not fully wrapped, suggests that SSB diffusion may persist during its cellular functioning even in the crowded conditions *in vivo* where the DNA is likely to experience tension of various magnitudes, and that the ability to diffuse on ssDNA may be shared by other ssDNA binding proteins that do not display closed wrapping, as suggested for phage T4 gene 32 protein [153]. SSB appears to diffuse continually as long as there is an available extension of ssDNA beyond its binding site size. This small-scale (tens of nucleotides) SSB diffusion along DNA should be important in the redistribution of SSB on ssDNA after its initial binding to a random location because for proteins with such high affinities, redistribution would be difficult if it required complete dissociation and reassociation. SSB diffusion over short lengths would be important for protecting these small DNA gaps and allowing access of SIPs to the ssDNA and hairpin removal by SSB. In addition, single SSB tetramers can be moved by the action of a directed motion as we have shown for RecA filament formation [124]. Our data also suggest RecO and other SIPs that bind to SSB via the SSB-Ct would not prevent but only moderately slow down SSB diffusion along ssDNA. The slowing of diffusion may be due to the weak interaction of RecO with ssDNA facilitated by SSB-Ct binding [150], and/or the increased radius of the SSB-RecO complex**.** Our data overall suggest that SSB diffusion may occur even when a SIP interacts simultaneously with both ssDNA and SSB and that SSB may serve as a dynamic platform to recruit SIPs for use in DNA replication, recombination and repair.

4.3.3 Implications for Nucleosomes

The closed wrapping of ssDNA around SSB bears some resemblance to the wrapping of ~ 147 bp of dsDNA around the histone core in a nucleosome [118,154,155]. The mechanistic insights that we obtained for SSB diffusion and dissociation processes parallel those observed for nucleosomes [156-160]. Nucleosomes can also be repositioned along duplex DNA [156], likely through the spontaneous unwrapping of the DNA ends [160], and RNA polymerase can rectify this thermal motion to move through chromatin [161]. A similar mechanism allows a growing RecA filament to rectify the diffusion of SSB into a directed movement [124].Two models for nucleosome sliding were proposed, based on the reptation of defects in polymer chains: through 10 bp bulge defects [128,143] and through 1 bp twist defects [162] but no experimental support is yet available for either. Our study provides direct experimental evidence for a reptation model of protein motion on ssDNA.

4.4 Experimental Procedures

DNA Sequences and Annealing Procedures

1. 5'- /biotin/ TGG CGA CGG CAG CGA GGC /Cy5/ - 3'
2. 5'-GGG CGG CGA CCT $(T)_{13}$ /iAmMC6T/ $(T)_{68}$ GCC TCG CTG CCG TCG CCA - 3'
3. 5’-AGG TCG CCG CCC TTT /digoxigenin/-3’
4. 5’- GCC TCG CTG CCG TCG CCA - /biotin/ - 3’
5. 5’- /Cy5/ GCC TCG CTG CCG TCG CCA -/biotin/- 3’
6. 5’- TGG CGA CGG CAG CGA GGC $(T)_{70}$ - 3’
7. 5’- TGG CGA CGG CAG CGA GGC $(T)_{16}$ /Cy5/ $(T)_{54}$ - 3’
8. 5’- TGG CGA CGG CAG CGA GGC $(T)_{35}$ /Cy5/ $(T)_{35}$ - 3’
9. 5’- TGG CGA CGG CAG CGA GGC $(T)_{70}$ /Cy5/T - 3’
10. 5’- TGG CGA CGG CAG CGA GGC $(T)_{68}$ /iAmMC6T/ $(T)_{8}$ - 3’
11. 5’- TGG CGA CGG CAG CGA GGC $(T)_{16}$ /Cy5/ $(T)_{24}$ - 3’
12. 5’- TGG CGA CGG CAG CGA GGC $(T)_{16}$ /Cy5/ $(T)_{35}$ - 3’
13. 5’- TGG CGA CGG CAG CGA GGC $(T)_{40}$ /Cy5/ - 3’

14. 5’- TGG CGA CGG CAG CGA GGC $(T)_{40}$ - 3’
15. 5’- TGG CGA CGG CAG CGA GGC $(T)_{16}$ /iAmMC6T/ $(T)_{43}$ - 3’
16. 5’- TGG CGA CGG CAG CGA GGC $(T)_{31}$ /iAmMC6T/ T - 3’
17. 5’- TGG CGA CGG CAG CGA GGC $(T)_{41}$ /iAmMC6T/ T - 3’
18. 5’- /Cy3 / $(T)_{50}$ GCC TCG CTG CCG TCG CCA -3'
19. 5'-GGG CGG CGA CCT /iAmMC6T/ $(T)_{65}$ GCC TCG CTG CCG TCG CCA - 3'

The sequence in red is the 12 nt cohesive end site of phage lambda DNA. The amine-modified thymine (iAmMC6T) shown in the sequence enables the oligonucleotides to be labeled with the monofunctional NHS ester form of Cy3 or Cy5 dyes (GE Healthcare). Otherwise, Cy3 or Cy5 dye was attached directly to the DNA backbone using phosphoramidite chemistry. DNA Annealing protocol is the same as described in Chapter 3.

Protein Purification, Characterization and Labeling

E. coli SSB, SSB-C proteins (>99% homogeneity), SSBΔC [135], SSBΔC8 [152] and SSB mutant (A122C labelled with ~ one Alexa555 per SSB tetramer) [124] were purified as described. *E. coli* RecO protein was expressed and purified as described [163,164]. The assembly state and stability of RecO protein was verified using sedimentation equilibrium at two concentrations (3 and 4 μM) and three rotor speeds (20, 25 and 30 thousands RPM) as described [165]. All sedimentation profiles (not shown) obtained either under conditions of single molecule assays (Figures 7 and S7E) or ITC binding experiments (Figure S7A-C) fit well to a model for a single ideal species with molecular masses 26.9 ± 0.3 kD and 25.9 ± 0.4, respectively, similar to that expected for a RecO monomer (27.3 kD).

Sample Assembly and Data Acquisition

For fluorescence-force measurements, the protocols and instrumentation are described in Chapter 2 and Chapter 3. For the diffusion measurement of SSB at zero force, the partial duplex DNA was surface immobilized as described above but the beads were not added afterwards. Instead, 1 nM of SSB was directly added with the aforementioned imaging buffer and then incubated for 1 min to form the SSB-ssDNA complexes before flushing with the same imaging buffer (but with no SSB) to remove the excess SSB from solution. All the experiments with RecO were performed with a total internal reflection (TIR) microscope described in Chapter 1. After SSB/DNA complexes were formed and excess SSB proteins were removed, RecO was added at varying concentrations with buffer: 200 mM KCl, 0.2% DMSO (or 10 mM $MgCl_2$, 80 mM KCl, 0.8% DMSO), 20 mM Hepes:NaOH (pH 7.5), 0.5mM TCEP, 1 mM EDTA, 0.1 mg/ml BSA, 5% (vol/vol) glycerol, 0.5 % (wt/vol) D-glucose, 165 U/ml glucose oxidase, 2170 U/ml catalase, 3 mM Trolox, and RecO at concentrations as stated. Single-molecule FRET histograms were generated by averaging for 300 ms.

Isothermal Titration Calorimetry (ITC)

All ITC experiments were performed using a VP-ITC titration microcalorimeter (MicroCal Inc., Northampton, MA) in buffer C (200 mM KCl, 10 mM Cacodylate, pH 7.0, 0.1 mM EDTA, 1 mM BME, 25% glycerol) following the routine established for studying SSB interaction with PriA and Chi proteins [166]. RecO concentrations were 1-3 μM in the cell, and C-terminal peptides and SSBs concentrations in the syringe were 40-100 μM and 8-14 μM (tetramer), respectively (Figures S7A and S7B). In Figure S7C, the concentration of SSB in the cell was 1 μM and concentration of $(dT)_{70}$ in the syringe 15 μM. Binding isotherms were analyzed using n-independent and identical sites model as described [166].SSB C-terminal peptides WMDFDDDIPF and WMDFDDDISF were obtained from Celtek peptides (Celtek Bioscience, LLC, TN). The Trp residue at N terminus was added for better quantification of peptide concentration (ε_{280}= 5500 $M^{-1}cm^{-1}$)

Cross-correlation Analysis

The cross-correlation analysis was performed as previously described [167]. The calculated cross-correlation functions were calculated between donor and acceptor time traces for a given molecule. By fitting the calculated cross-correlation functions to a single exponential function, one obtains two parameters (the characteristic time of the exponential, τ, and the amplitude of the exponential at $\tau = 0$). As an extra example, we re-examined SSB diffusion along a 70 nt ssDNA using two different labeling schemes: (A) Cy3-Cy5 labeled DNA and SSB; (B) Cy5-labeled DNA and SSB_f (Figure 4.12A). Both schemes showed anti-correlated fluctuations of I_D and I_A (Figure 4.12B; 10 ms time resolution), likely due to SSB diffusion on ssDNA. The fluctuation time scales (30 ± 2 ms for Scheme A and 149 ± 4 ms for Scheme B) obtained from single-exponential fits to the cross-correlation of I_D and I_A[167,168] were similar to those for SSB diffusion on similar length ssDNA[124]. The faster fluctuations of smaller amplitudes observed using Scheme A are likely due to a different degree of degeneracy in the FRET states (Figure 4.12C).

4.5 Figures

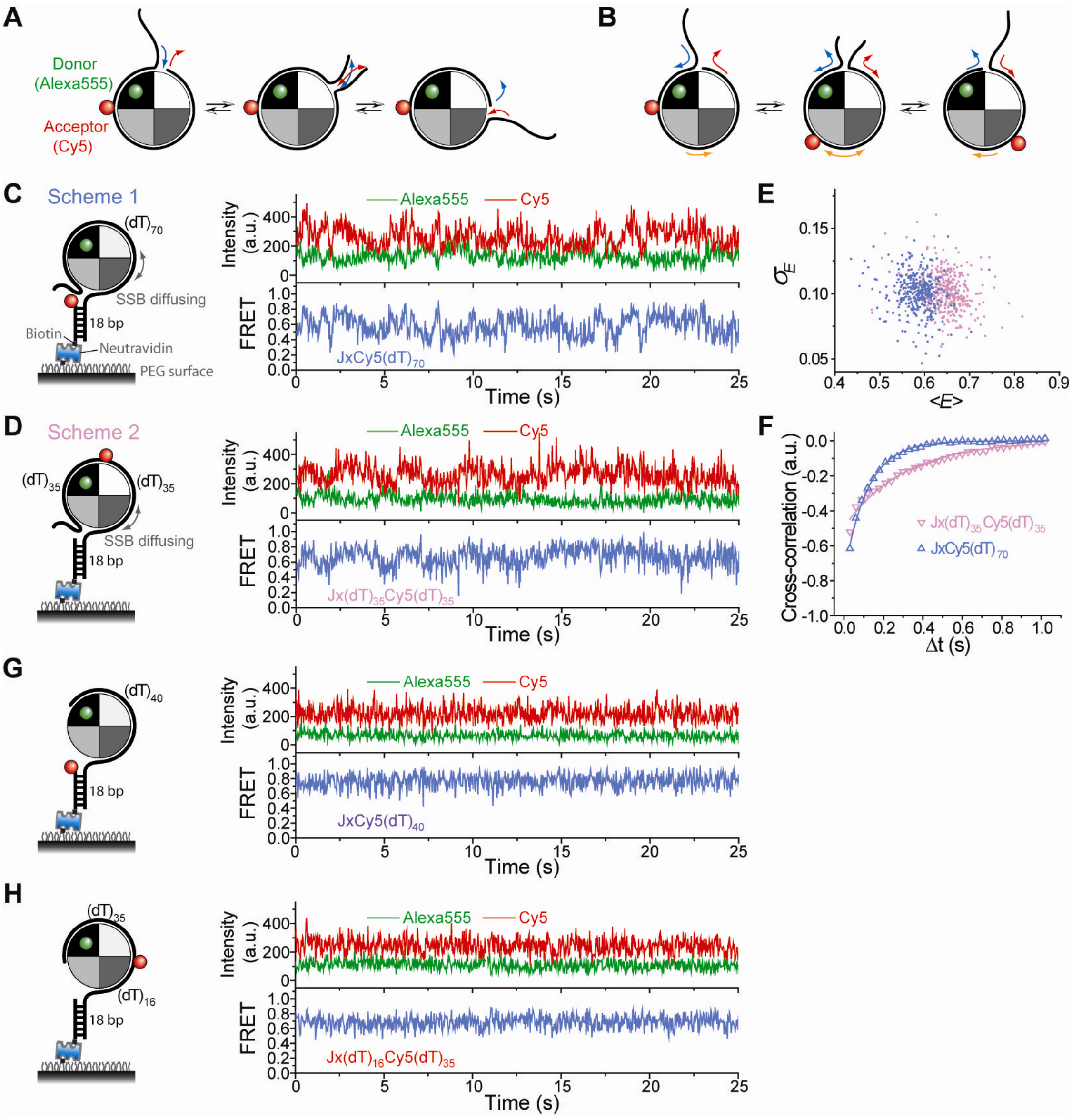

Figure 4.1 Evidence favoring the sliding mechanism over the rolling mechanism. (A) Rolling mechanism for SSB diffusion. One end of the wrapped DNA could partially dissociate from the SSB while the other end of the DNA binds to the same newly open DNA binding site. This mechanism is facilitated by the ‘closed wrapping’ topology of the DNA around the SSB tetramer and there is no relative ‘sliding’ motion between ssDNA and the SSB surface in this model. Only the ends but not the mid-section of the bound DNA slide/move relative to SSB during diffusion. (B) Sliding mechanism for SSB

diffusion. In this mechanism, the whole SSB-bound DNA (65 nt) slides relative to protein surface during diffusion. (C and D) Representative single-molecule time traces of donor(Alexa555) and acceptor(Cy5) intensities and corresponding FRET efficiency show fluctuations induced by SSB_f diffusion along the ssDNA if Cy5 is attached near one end of $(\text{dT})_{70}$ (Scheme 1) or to the middle of $(\text{dT})_{70}$ (Scheme 2; 30 ms time resolution). a.u., arbitrary units. (E) A scatter plot of $\langle E\rangle$ versus σ_E for individual FRET time trajectories obtained from the two Cy5 labelling schemes. (F) Cross-correlation analysis of single-molecule intensity-time traces fit to single exponential function for data obtained with the two labeling schemes in (C) and (D) (averaged over > 300 molecules each).

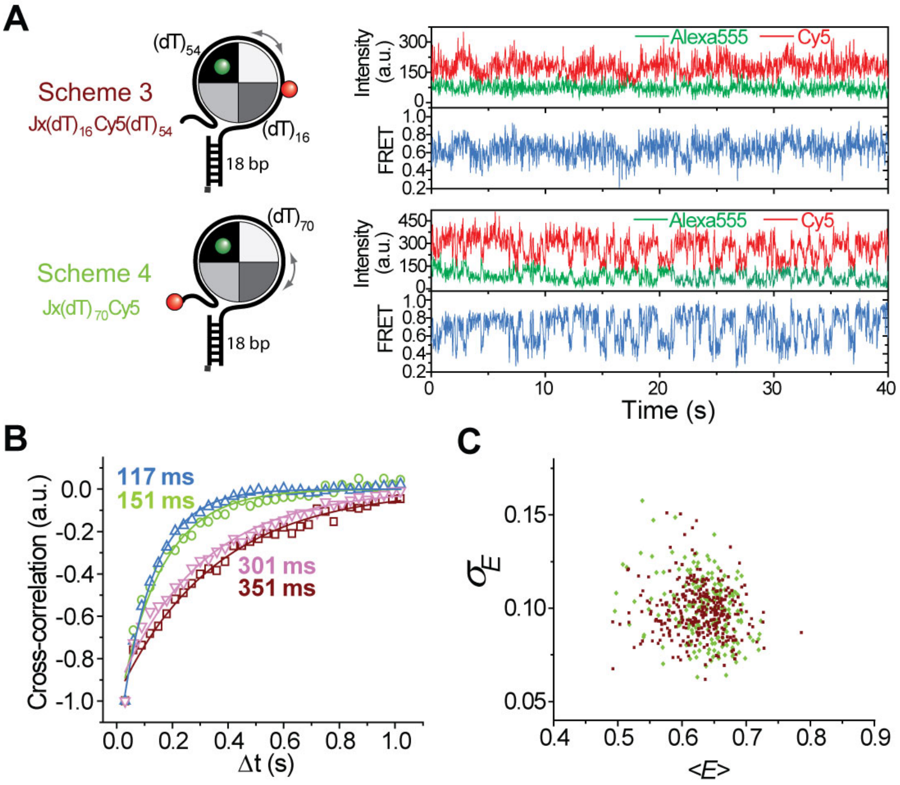

Figure 4.2 (A) The other two Cy5 labeling schemes for $\text{SSB}_\text{f}/(\text{dT})_{70}$ and their typical corresponding FRET time traces (time resolution: 30 ms). To test whether the reptation or rolling mechanisms is more likely, we varied the Cy5 labeling locations on the same DNA partial duplex. Cy5 was positioned either 0, 16, 35, or 70 nt away from one end of the ssDNA $(\text{dT})_{70}$. The length of the ssDNA here was only 5 nt longer than the SSB tetramer binding site size (65 nt). The rolling mechanism proposed previously suggests no relative 'sliding' movement between bound ssDNA and the SSB surface so the DNA

substrates with internally labeled Cy5 should not yield FRET fluctuation as when Cy5 was attached to either end of the ssDNA because in the rolling model diffusional dynamics occurs only at the two unwrapping/rewrapping ends of the ssDNA. However, the FRET time traces show the same amplitude of diffusion-induced fluctuations for all four DNA substrates, indicating the existence of movement of protein relative to ssDNA.

(B) Normalized cross-correlation analysis of FRET trajectories fit to single exponential function for data obtained with the four labeling schemes (average from more than 300 molecules for each scheme). The characteristic time constants obtained for these fluctuations are 117 ± 3, 301 ± 22, 351 ± 25, 151 ± 10 ms for Schemes 1, 2, 3, 4 respectively. The characteristic times obtained from Schemes 1 and 4 were longer, possibly due to bulge formation events that when created at the ends did not propagate to the middle of the DNA if a reptation model is considered for SSB diffusion.

(C) A scatter plot of <E> versus σ_E for individual FRET time trajectories obtained from Schemes 3 and 4. σ_E, reflecting the amplitude of the fluctuations, shared a same mean compared with Schemes 1 and 2.

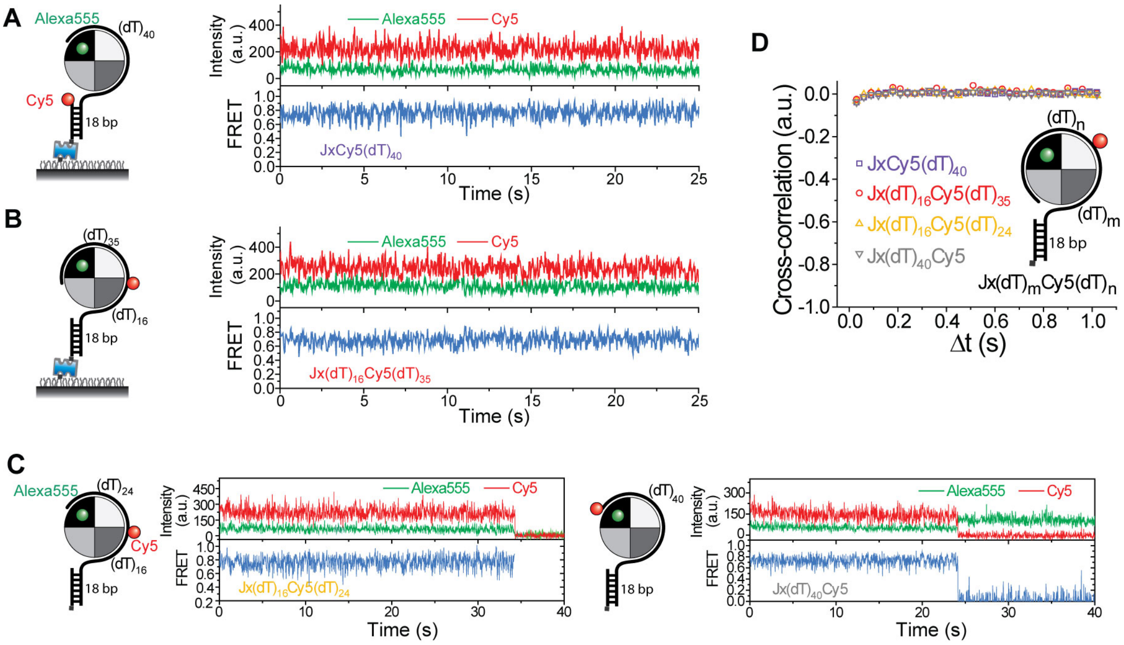

Figure 4.3 (A and B) Representative single-molecule intensity-time traces (30 ms time resolution) suggest the FRET fluctuations are inhibited if SSB$_f$ binds to a Cy5-labeled

ssDNA that is shorter than the SSB tetramer binding site size ($(dT)_{40}$ and $(dT)_{51}$). (C) Two other Cy5 labeling schemes for $SSB_f/(dT)_{40}$ and their typical corresponding FRET time traces. (D) Cross-correlation analysis of single-molecule intensity-time traces for data obtained with the shorter ssDNA in (A-C) (averaged over > 100 molecules each).

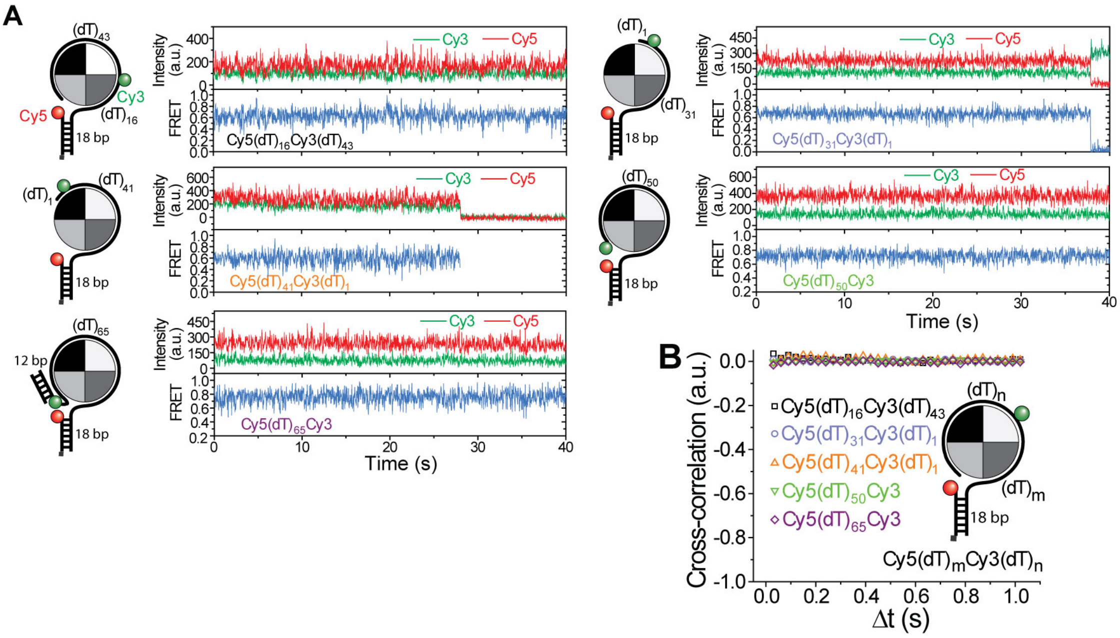

Figure 4.4 (A) Five DNA labeling schemes and their typical corresponding FRET time traces when SSB binds to the ssDNA. The lengthes of the ssDNA here were either the same with or shorter than the SSB tetramer binding site size. The Cy3-Cy5 separation was 16, 31, 41, 50 and 65 nt of ssDNA respectively. (B) Cross-correlation analysis of single-molecule intensity-time traces for data obtained with five Cy3-Cy5 labeled DNA constructs whose ssDNA tail lengths are equal to or shorter than the SSB tetramer binding site size (averaged over > 100 molecules each).

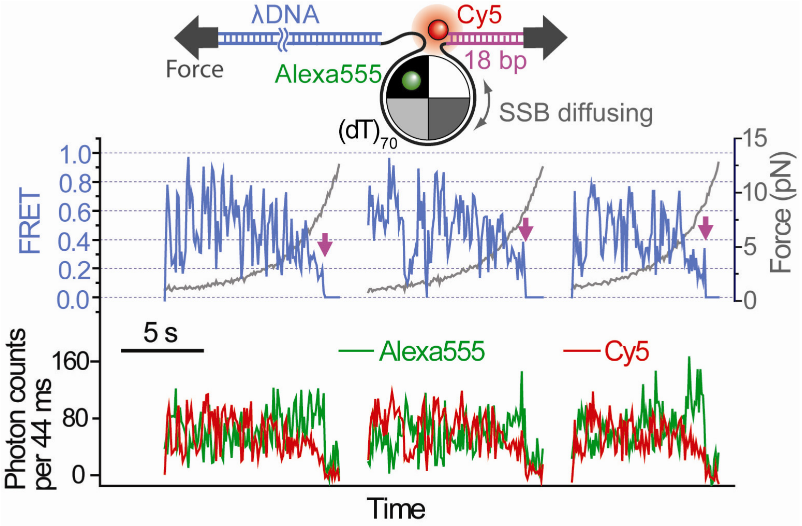

Figure 4.5 SSB diffusion persists under tension. FRET trajectories of SSB_f continue to show diffusion-induced fluctuations with increasing force up to ~ 5 pN. Magenta arrows indicate SSB_f dissociation events.

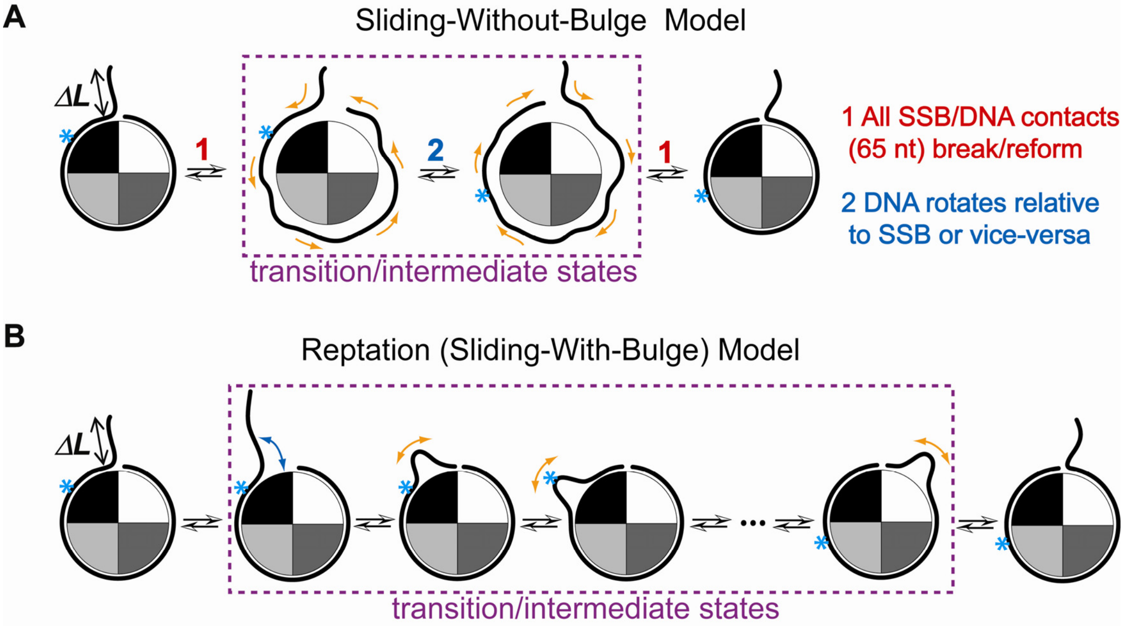

Figure 4.6 Schemes for two possible SSB sliding mechanisms. (A and B) For the sliding mechanism, the whole bound DNA sliding would occur through different transition or intermediate states. The sliding-without-bulge model (or ‘hopping’) would require the simultaneous rupture of all of the binding interactions between ~ 65 nts of DNA and the SSB protein surface as the transition state (A). Alternatively, a sliding-with-bulge model, namely the reptation mechanism for SSB diffusion, allows the sliding of the whole bound

DNA relative to SSB surface to occur little by little. As the transition states in reptation, the ssDNA at the 'edge' of the SSB partially dissociates from the protein surface and distortion of this unwrapped segment of DNA can form a loop-bulge with an extra length of three nucleotides, and this 'defect in stored length' propagates back and forth over the entire wrapped portion until it emerges on the other side, leading to one step of SSB diffusion along the ssDNA (B). The arrows represent the DNA movements and the cyan asterisk represents a single nucleotide position on the DNA. The asterisk-marked position on ssDNA will slide along the protein surface by the end of the diffusion cycle.

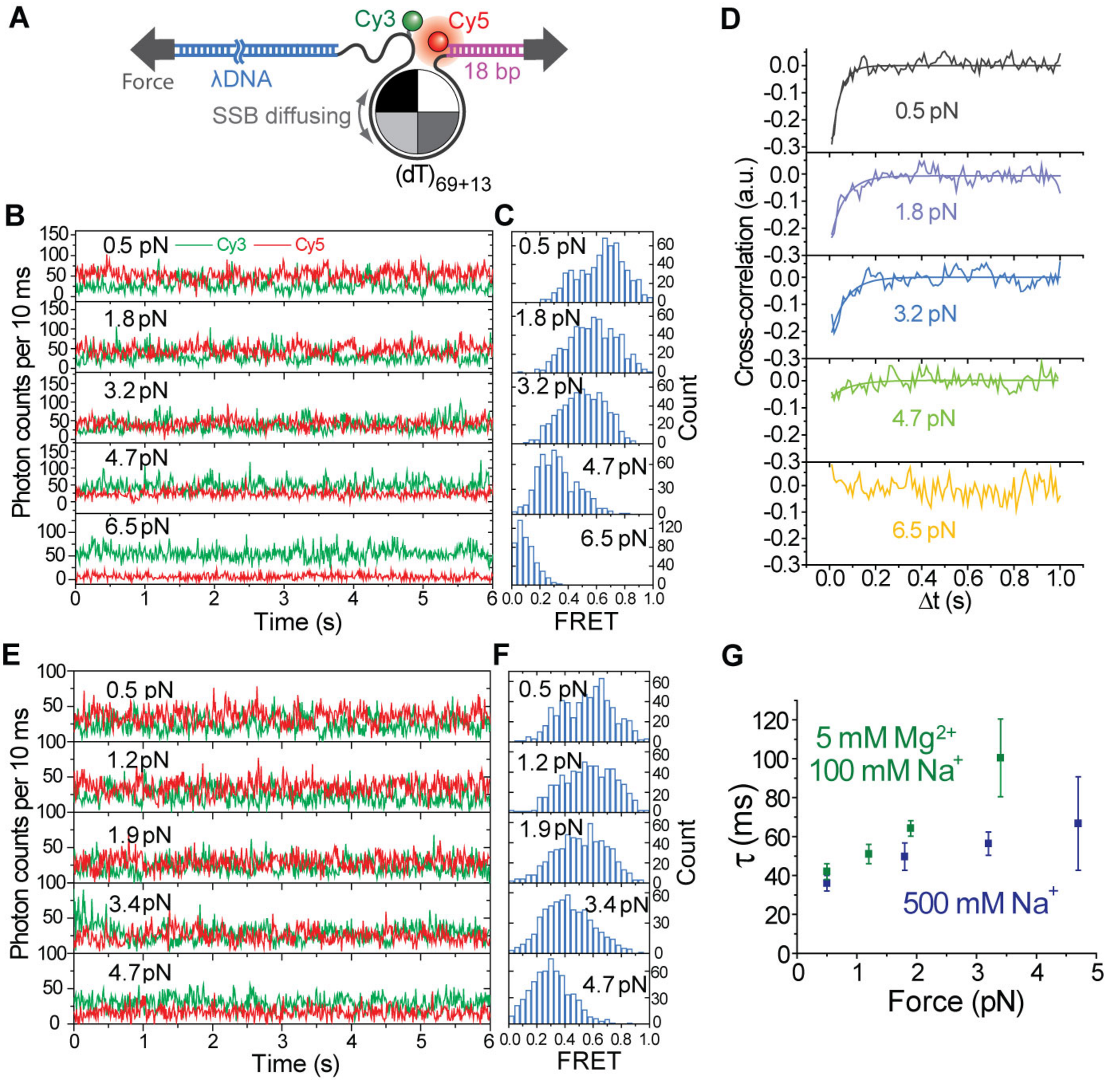

Figure 4.7 Mechanical control of SSB diffusion along DNA and the reptation (sliding-with-bulge) mechanism. (A) Experimental scheme with extended ssDNA region.

Fluorophores are conjugated to the 82 nt long ssDNA ($(dT)_{69+13}$) as shown. (B and C) Cy3-Cy5 time traces and FRET histograms at five different constant forces when SSB binds to $(dT)_{69+13}$ in 500 mM Na^+ and 1 nM SSB tetramer (10 ms time resolution). These diffusion-induced FRET fluctuations persisted even at forces up to 4.7 pN. The characteristic time scale of SSB diffusion at different forces can be obtained by cross-correlation analysis. (D) Cross-correlations of donor and acceptor intensities over time and exponential decay fits in 500 mM Na^+ at five different constant forces (10 ms time resolution). (E and F) Cy3-Cy5 time traces and FRET histograms at five different constant forces when SSB binds to $(dT)_{69+13}$ in 5 mM Mg^{2+} and 100 mM Na^+ (10 ms time resolution). (G) The characteristic time scale τ of SSB diffusion determined from the exponential fit of cross-correlation vs force obtained under two ionic conditions. Error bars are s.e.m.

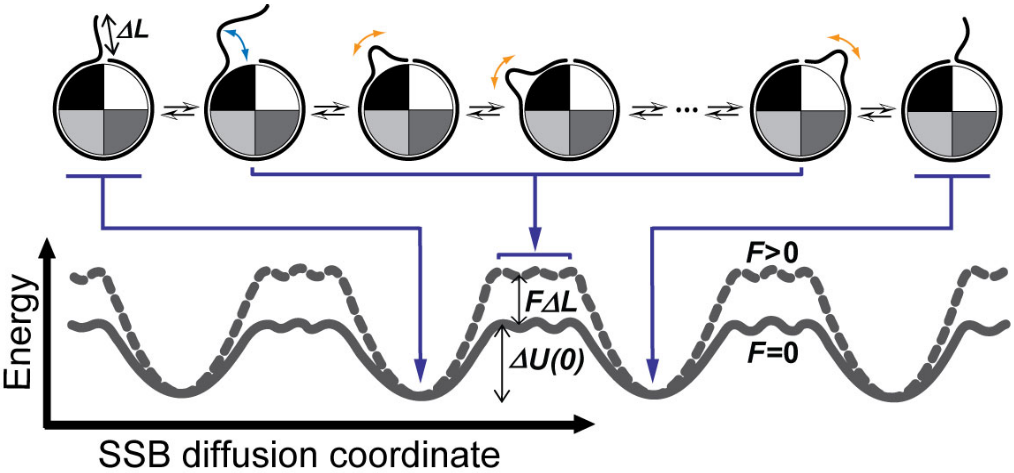

Figure 4.8 Energy landscape along the SSB diffusion coordinate and the proposed reptation model for SSB diffusion on DNA. ΔL is the reduction in the overall DNA length when the thermally activated DNA bulge is formed. Solid line for force $F = 0$; dashed line for $F > 0$.

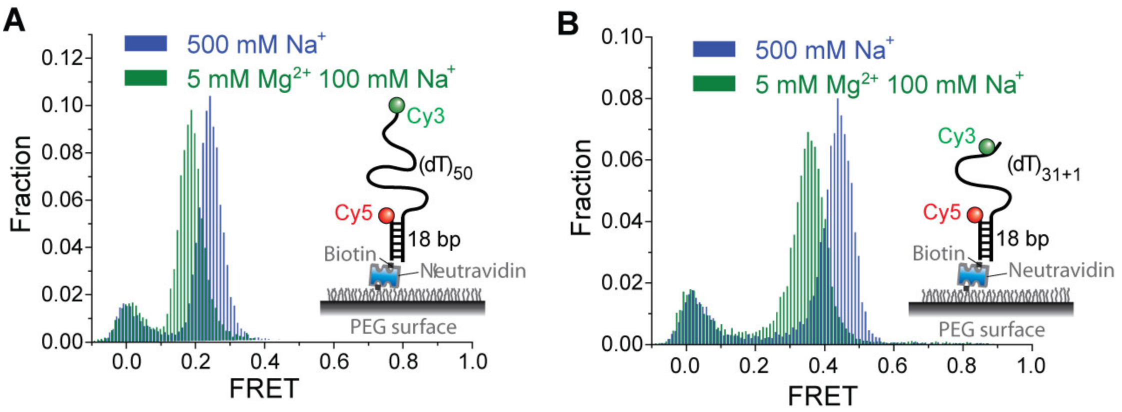

Figure 4.9 FRET histograms of naked ssDNA $(dT)_{50}$ and $(dT)_{31+1}$ in two ionic conditions, suggesting the persistence length of ssDNA is larger in 5 mM Mg^{2+} and 100 mM Na^{+} [125]. The peaks at zero FRET are due to DNA molecules possessing inactive Cy5, whereas the other peaks are due to FRET.

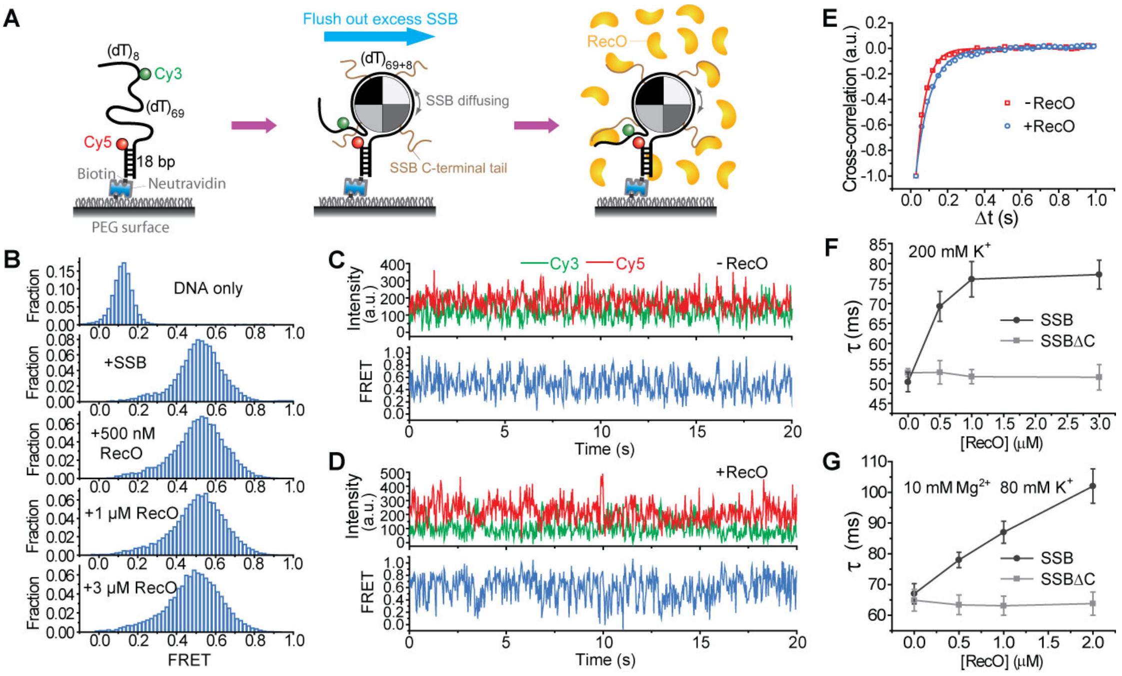

Figure 4.10 SSB diffusion along ssDNA persists but slows down when SSB interacts with RecO via SSB-Ct. (A) Schematic of reaction steps. (B) FRET efficiency histograms for $(dT)_{69+8}$ DNA only, and DNA/SSB complexes in the absence and presence of RecO. (C) Representative single-molecule time traces of DNA/SSB in the absence of free SSB

and RecO (in 200 mM K^+). (D) Representative single-molecule time traces of DNA/SSB/RecO complex in 3 μM RecO and in the absence of free SSB (in 200 mM K^+). (E), Normalized cross-correlations of donor and acceptor intensity time traces as shown in (C) and (D) averaged over more than 300 molecules each with and without 3 μM RecO. Single exponential fits are also shown. (F) The characteristic time scale τ of SSB diffusion determined from the exponential fits of cross correlations as shown in (E) as a function of RecO concentrations for wild type SSB and SSBΔC in 200 mM K^+. τ of SSB diffusion as a function of RecO concentrations for wild type SSB and SSBΔC in 10 mM Mg^{2+} and 80 mM K^+.

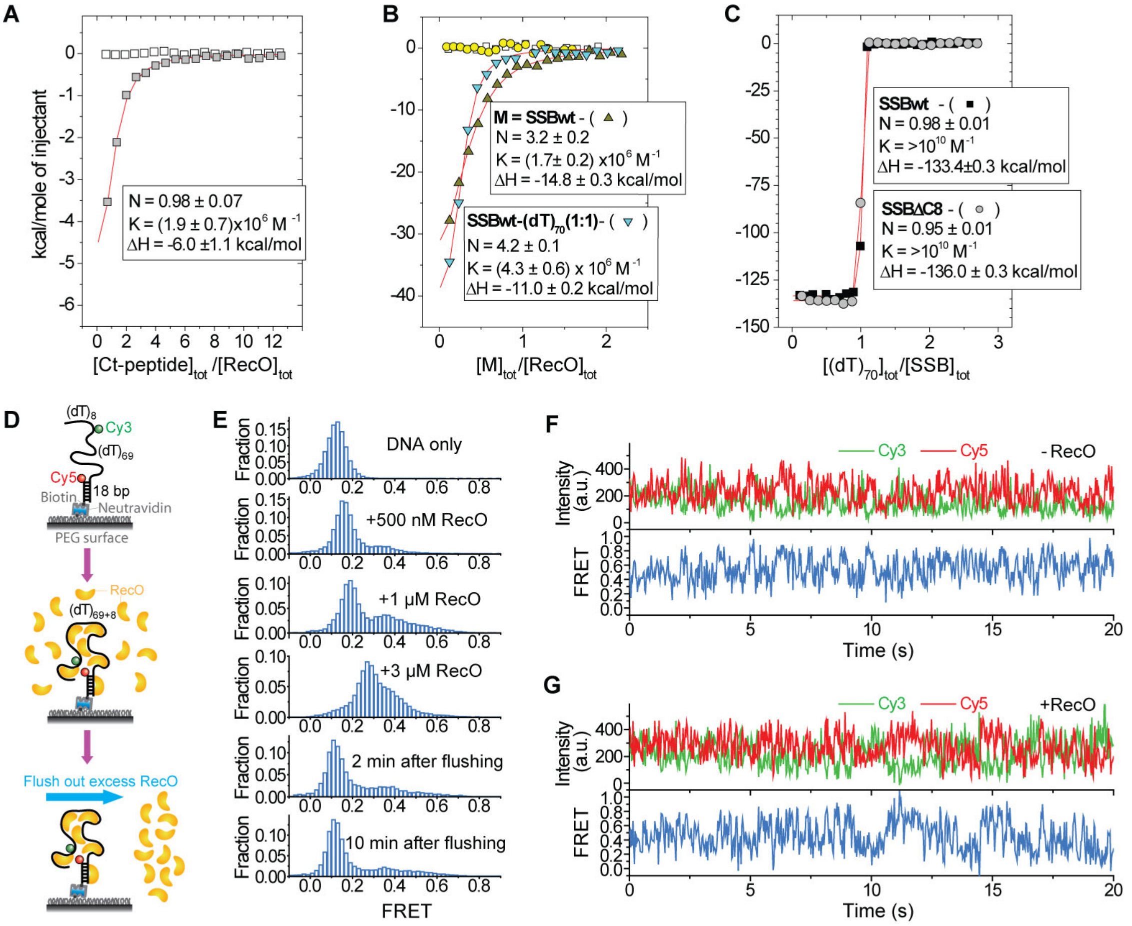

Figure 4.11 RecO binding to SSB-Ct peptide, SSB, SSB-$(dT)_{70}$ complex, and $(dT)_{69+8}$ DNA. (A) Results of ITC (Isothermal Titration Calorimetry) titration of RecO with SSB-Ct peptide, WMDFDDDIPF, (grey squares) indicate that RecO binds one molecule of the peptide with moderate affinity ~ 2×10^6 M^{-1}, whereas the interaction with the peptide

containing a single Pro to Ser mutation, corresponding to the SSB-113 mutation, which is known to disrupt a number of protein interactions with SSB-C-terminus [120,169] is not detectable (open squares).

(B) Reverse titrations of RecO with SSB (dark yellow triangles) and SSB-dT$_{70}$ (1:1) stoichiometric complex (cyan triangles) confirm that ~4 molecules of RecO interact with SSB tetramer (1 per C-terminal tail). Control titrations with SSBΔC8, lacking last 8 amino acids, (yellow circles) and its complex with (dT)$_{70}$ (open squares) show no detectable interaction with RecO. The affinity of RecO binding to C-terminal tails of SSB tetramer appears to be similar to C-terminal peptide alone. However, slight increase in affinity (~two fold) is observed when SSB tetramer is in the stoichiometric complex with (dT)$_{70}$. The latter increase could be related to additional contacts, which RecO may form interacting weakly with ssDNA in the complex, as was observed previously for another SIP protein, PriA helicase, which also can interact weakly with ssDNA alone [166].

(C) Control titrations of SSB and SSBΔC8 with (dT)$_{70}$ indicating that both proteins form identical stoichiometric ($K>10^{10}$ M^{-1}) 1:1 complex with ssDNA. All binding isotherms presented in panels a, b and c were analyzed using n- independent and identical site model as described [166]. The smooth lines through the experimental points represent fits of the data with the best fit parameters, N – the stoichiometry of binding, K – equilibrium binding constant (M^{-1}) and ΔH – enthalpy change (kcal/mol), which are shown in the inserts with the errors representing S.D.

(D) Schematic of reaction steps. RecO were added to the immobilized partial duplex DNA that contains (dT)$_{69+8}$. FRET histograms were obtained 10 min after RecO addition at varying RecO concentrations. Excess RecO were then flushed out and FRET histograms were obtained 2 min and 10 minutes after flushing.

(E) FRET histograms for (dT)$_{69+8}$ DNA, DNA/RecO complexes at varying RecO concentrations and after flushing out excess RecO in 200 mM K^+. FRET histograms suggest RecO binds to ssDNA without a well defined FRET state for RecO binding.

(F) Representative single-molecule time traces of DNA/SSB in the absence of free SSB and RecO (in 10 mM Mg^{2+} and 200 mM K^+).

(G) Representative single-molecule time traces of DNA/SSB/RecO complex in 2 μM RecO and in the absence of free SSB (in 10 mM Mg^{2+} and 200 mM K^+).

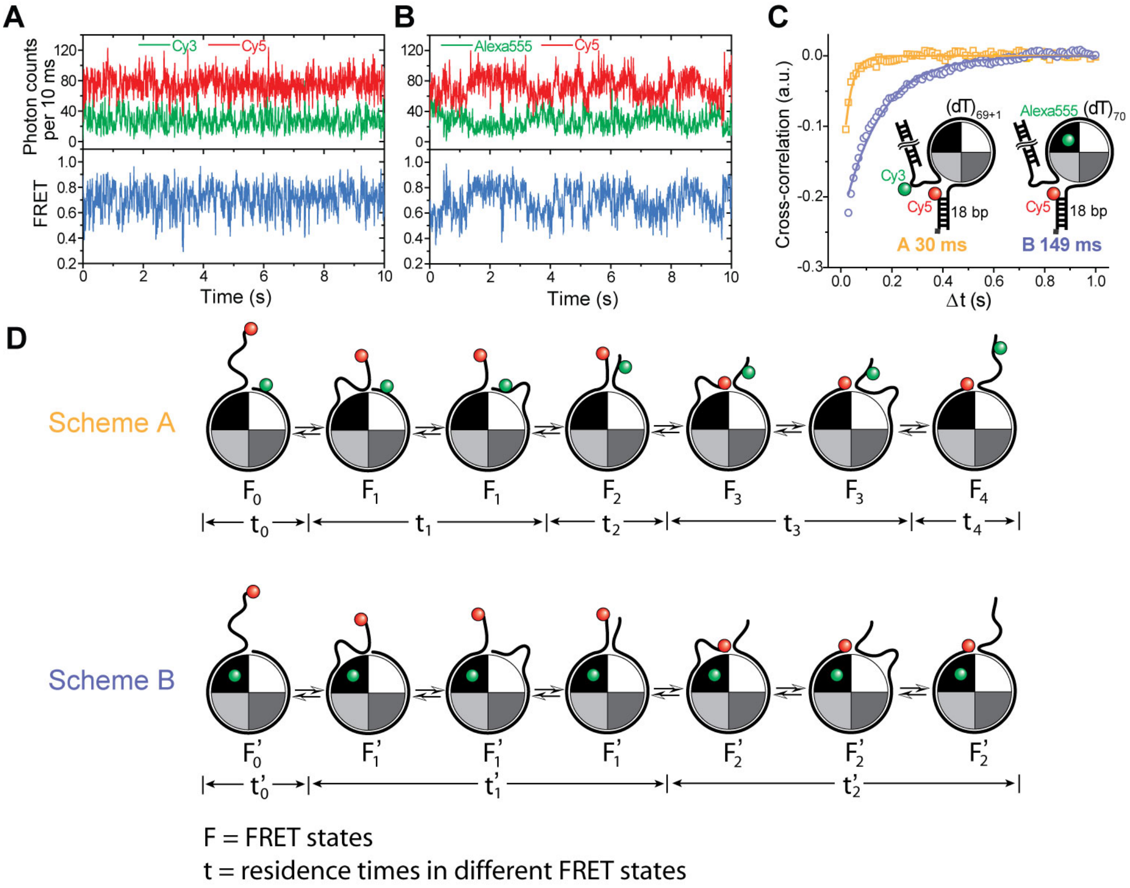

Figure 4.12 Cross-Correlation Analysis for Labeled and Unlabeled SSB. (A and B) Anti-correlated donor-acceptor time traces with corresponding FRET efficiency (time resolution: 10 ms). SSB binds to DNA substrates that contain an ssDNA region 70 nt long flanked by two dsDNA arms but the FRET pair has two different labeling schemes: A) Cy3 and Cy5 were labeled near the two ends of the 70nt ssDNA; B) Cy5 was attached near one end of the 70nt, whereas Alexa555 was labeled on the SSB (one Alexa555 per tetramer on average). (C) Cross-correlation analysis of experiments performed using Scheme A (yellow, average from 73 molecules) and Scheme B (purple, average from 76 molecules) for SSB binding to (dT)$_{70}$ at zero force. Solid lines show single exponential fits. The fluctuation time scales (30 ± 2 ms for Scheme A and 149 ± 4 ms for Scheme B) obtained from single-exponential fits to the cross-correlation of I_D and I_A were similar to those for SSB diffusion on similar length ssDNA [124]. (D) Comparison of residence times in difference FRET states for Schemes A and B in a cycle containing two SSB diffusion steps by a reptation mechanism. We plotted all the FRET states (F) and their

corresponding residence times (t). One would anticipate multiple residence times though it might not be resolved with the given time resolution. Note that the duplex DNA part was not shown in the picture for simplification and the Cy3 labeling site for Scheme A was not exactly on the end of the ssDNA, either of which has made the labeling asymmetric for the two ends in Scheme A (F_1 and F_3 would not yield the same FRET, and the same is true for F_0 and F_4). But in Scheme B, there exists a greater degree of degeneracy in the FRET states, resulting in longer residence times (t_1'= t_1 + t_2 ; t_2'= t_3 + t_4). This can explain why we observed longer characteristic times for Scheme B from the cross-correlation analysis.

Chapter 5
Mapping Two-Dimensional Reaction Landscape of the Holliday Junction[**]

5.1 Introduction

Holliday juncions (HJs) are a four-way DNA junction structures, the central DNA intermediates in homologous genetic recombination which are important in DNA rearrangements and in the repair of double-strand breaks in DNA[170]. In the absence of ions the junction adopts an 'open' state where the four arms are directed toward the corners of a square with an open central region (Figure 5.1A). In the presence of physiological concentrations of magnesium ions (or some monovalent and divalent mental ions), the HJ becomes more compact by pairwise coaxial stacking of helical arms into a right-handed antiparallel stacked-X structure [171-173]. There are two ways of forming this stacked structure that depend upon the choice of helical stacking partners (*iso*I and *iso*II), and a single junction can undergo fast dynamics of conformational exchanges between *iso*I and *iso*II conformers (Figure 5.1B) [174,175]. At present, there is no structural information on the transient species populated during these conformational changes, and the population of *iso*I relative to *iso*II strongly depends on the junction core sequence [174,176].

Many biological processes are dependent on tension. In recent years, single molecule force measurements have shown directly that biochemical reactions can be influenced by applied force [74]. Yet, purely mechanical tools can not detect small scale conformational changes unless persistent and strong enough force is applied. At weak forces, the flexible tether connecting the mechanical probe to the biological molecule is not fully stretched and therefore can not transmit small movements. This is unfortunate because weak and transient forces are likely more prevalent *in vivo*, but the experimental

---

[**] This work has been published as a paper:
Hohng, S., Zhou, R. et al. Fluorescence-force spectroscopy maps two-dimensional reaction landscape of the holliday junction. *Science* **318**, 279-283 (2007).

limitations confine *in vitro* single molecule studies to examining the effect of relatively large forces. We aimed to study the effect of small external forces by combining single molecule fluorescence resonance energy transfer (smFRET) [177-179] with manipulation using optical tweezers [180] such that an individual molecule's conformational fluctuations can be measured by FRET as a function of force. smFRET has high spatial resolution (≤ 5 Å) [181,182]) and can be measured at arbitrarily low forces. Previous attempts to combine FRET and optical trap using the DNA hairpin as a model system [183,184] did not reveal new information because the hairpin unzips at high forces (~ 15 pN), a regime that had been extensively investigated using force-based methods [185,186]. Here, we use fluorescence-force spectroscopy to detect nanometer-scale motion at sub-pico Newton (pN) forces. We used the approach to gain insight into the reaction landscape of the Holliday junction (HJ) by gently stretching it along different directions.

5.2 Experimental Scheme and HJ Construct Design

To investigate the nature of the possible transient HJ structures and to understand how HJ conformational properties could depend on physiologically relevant forces, we built a hybrid instrument that combines smFRET with optical trapping via a long linker (bacteriophage λ DNA) as we describe in Chapter 2. The trapping and fluorescence excitation beams in our confocal microscope are spatially separated (minimum 13 μm, Figure 5.2A) such that fluorescence and force processes can operate without mutual interference. The long linker acts as a loose spring that dampens the random forces generated by Brownian motion of the trapped bead and reduces force variations due to the nanometer-scale conformational change of the HJ. Therefore, the measurements can be performed under effectively constant force without the need for active force clamping. The relaxation time scales of the λ DNA are faster than the time scale of conformational fluctuations we investigate here [187]. The trapping beam (1,064 nm) was fixed along the optical axis of the microscope, and force was applied by moving the surface-tethered HJ using a piezoelectric sample scanner. The confocal excitation beam (532 nm) was programmed to follow the HJ using a piezo-controlled mirror to maintain uniform excitation and detection efficiencies regardless of the specimen location (and therefore force).

Under physiological conditions, i.e. with magnesium ions present, the HJ becomes more compact by pairwise stacking into a right-handed antiparallel stacked-X structure [171-173]. In Figure 5.2B, we show the two alternative ways of forming this stacked structure that depend upon the choice of helical stacking partners (*iso*I and *iso*II). To determine comprehensively the force response of the HJ, we used the following four constructs (Figure 5.2C). The four helices comprising the HJ are named B (red), H (green), R (dark gray), and X (gray). Helix R was labeled at its 5' terminus with biotin for surface immobilization, and helices X, H, or B were extended by a 12 nt ssDNA 5'-overhang to permit annealing to a cohesive end of λ-DNA (named junctions *XR*, *HR* and *BR* respectively). The other end of the λ-DNA was attached to a bead via digoxigenin/anti-digoxigenin coupling in order to pull on the DNA using optical tweezers in three different directions, between X and R arms for junction *XR* etc. Junctions *XR* and *XR*-long differ in the length of the X and R arms (11 bp vs. 21 bp). For these studies, we have chosen a well-studied junction construct called junction 7 which has similar population of stacking conformers *iso*I and *iso*II [176]. Cy3 (FRET donor), was attached to the 5'-terminus of helix H, and Cy5 (acceptor) to the 5'-end of helix B. For junctions *XR* and *XR*-long, the stretching force should favor *iso*I (low FRET), in which there is a larger separation between the two tether points, over *iso*II (high FRET) (Figure 5.2D). Likewise, *iso*II (high FRET) would be favored at high forces for junction *HR*. In contrast, the two tether points would have similar distances for *iso*I and *iso*II in the case of junction *BR*, and force-induced bias should be minimal.

5.3 Experimental Results

5.3.1 Conformational Equilibrium of Different HJ Constructs at Zero Force

We first compared the conformational equilibrium at zero force among the different HJ constructs that we designed above but without a λ-DNA attached and in the absence of trapping laser beam. The transition rate from *iso*I to *iso*II (k_f) and the transition rate from *iso*II to *iso*I (k_b) can be determined from FRET time traces of single HJ molecules. We made the scatter plots of k_f versus k_b for individual FRET time traces obtain for each HJ construct (Figure 5.3). It is clear from the scatter plots that the dynamic behaviors of the isolated junctions are not modified significantly when the adhesive single stranded tail is added to a different arm (Figure 5.3A) and when the arm lengths are changed (Figure 5.3B) because the scatter plots for all the HJ constructs tested showed no significant difference.

5.3.2 Force Response of Different HJ Constructs

We next applied forces to junctions *XR*, *HR* and *BR* to study how applied forces through different vectors (or arm pairs) influence the conformational dynamics of a same HJ molecule (Junction 7 in this case). Figure 5.4A shows smFRET time traces at five different forces (gray lines, 10 s duration each with 10 ms integration time) obtained from a single molecule of junction *XR*. Enhanced photostability by means of the use of Trolox [188] allowed us to obtain one to five cycles of force data from a single molecule before fluorophore photobleaching, corresponding to observation over 50 to 250 s. Idealized FRET trajectories generated by hidden Markov modeling (red lines) [189] are also shown. At the lowest force (0.3 pN), the junction switches between the high and low FRET states with similar populations. As the force exceeds 1 pN, the dynamics become clearly biased to the low FRET state. Figure 5.4B shows the transition rates determined from hidden Markov modeling as a function of force. The transition rate k_f for the forward reaction from the low FRET state (*iso*I) to the high FRET state (*iso*II) decreases with increasing force (blue), while the transition rate for the backward reaction k_b (*iso*II to *iso*I) increases with force (red) as expected. Both changes were linear in the log-linear scale but interestingly, k_f had twice the slope of k_b. If the reaction is viewed as possessing a single transition state, the slope reflects the distance to the transition state [74]. Therefore, the transition state lies closer to *iso*II than to *iso*I when force is applied via the *XR* vector. According to Ref.[74], we have the following equations for a two-state reaction energy landscape (Figure 5.5),

$$\Delta G^0 - F\Delta x_{eq} = -k_B T \ln K_{eq}(F) \tag{5.1}$$

$$-\frac{\Delta x_f^{\ddagger}}{k_B T}\cdot F = \ln k_f(F) - \ln k_f(0) \tag{5.2}$$

$$\frac{\Delta x_b^\ddagger}{k_B T} \cdot F = \ln k_b(F) - \ln k_b(0) \qquad (5.3)$$

where ΔG^0 is the energy difference between the two states. $K_{eq}(F)$ is the equilibrium constant at certain applied force F and can be determined from the ratio of dwell times of the molecule in the *iso*I and *iso*II states at any given force . $\Delta x_b^\ddagger$ represents the distance from *iso*II to the transition state (the energy maximum) along the reaction coordinate and $\Delta x_f^\ddagger$ represents the distance from *iso*I to the transition state along the reaction coordinate. the distance Δx_{eq} represents the distance between *iso*I and *iso*II along the reaction coordinate. $k_f(F)$ and $k_b(F)$ are the forward and backward transition rates at certain applied force, respectively. $k_f(0)$ and $k_b(0)$ are the forward and backward transition rates at zero force, respectively. We hence used Equations (5.2) and (5.3) to fit the data in Figure 5.4B and obtained $\Delta x_b^\ddagger$ and $\Delta x_b^\ddagger$ from the slope of the linear fits. Averaged over five molecules, for junction *XR* $\Delta x_b^\ddagger$ = 1.5 ± 0.3 nm and $\Delta x_f^\ddagger$ = 2.9 ± 0.6 nm (Table 5.1).

We next studied junction *HR* where the λ DNA tether has been transferred from the X to the H arm. In this construct, the force is expected to bias the HJ to the high FRET *iso*II state, and indeed this was the result (Figure 5.4C). k_b decreased and k_f increased with stronger forces, but with two-fold higher slope for k_b than for k_f (Figure 5.4D). Averaged over five molecules, $\Delta x_b^\ddagger$=2.4 ± 0.5 nm and $\Delta x_f^\ddagger$=1.3 ± 0.3 nm. In both junctions, ($\Delta x_b^\ddagger + \Delta x_f^\ddagger$) is equal to the distance between *iso*I and *iso*II, Δx_{eq}, calculated from equilibrium population vs. force data (Table 5.1). Therefore, the distances between the ends of the pulled arms, d_XR for junction *XR* and d_HR for junction *HR*, are suitable reaction coordinates spanning the complete trajectory from *iso*I to *iso*II (Figure 5.6A).

In one pulling direction represented by d_XR, the transition state lies closer to *iso*II (Figure 5.6A, middle panel) while for the other pulling direction along d_HR, the transition state more closely resembles *iso*I (Figure 5.6A, bottom panel). These two transition states can not represent a single structure because then both d_XR and d_HR must be relatively small, and by symmetry so must be d_XB and d_HB. Such a structure would have all four helices in the same hemisphere relative to the junction core which is highly unlikely considering the symmetry of the HJ. Instead, we favor a model where there are at least two different transition states, *ts*I and *ts*II, equal in energy but corresponding to different values of d_XR (or d_HR), such that force would elevate one of them into the single highest energy barrier via the tilting of the energy landscape (Figure 5.6A).

Finally, it is better to note that the data presented so far show that the distance change upon stacking conformer transitions is about 4 nm. Since thermal energy is about 4 pN nm, a force on the order of 1 pN would consequently change the equilibrium between the two states by 2-3 fold. Such small scale conformational fluctuations at these low forces are probably impossible to detect in a purely mechanical measurement, especially at our time resolution (10 ms).

5.3.3 A Lever Arm Effect

What determines the force sensitivity of the junction? Is it an intrinsic property of the junction core or is it dependent on the length of helical arms on which the force is applied? Since the four arms of the HJ meet at its center, we may recast the experimental configuration as a torque being applied around the central pivot point. The torque is proportional to the product of the magnitude of force and the distance between the point of application of the force and the pivot point (i.e., the length of the arm). Therefore, it could be expected that increasing arm length would result in a greater torque for the same force. We tested such a lever arm effect using junction *XR*-long, where the X and R arms are lengthened by about a factor of two (from 11 bp to 21 bp) compared to junction *XR*. FRET histograms as a function of applied force (Figures 5.7E and 5.7F) show that increasing the lever arm length has magnified the force effect such that much lower force is needed for junction *XR*-long to achieve the same conformational bias. Figures 5.7C and 5.7D compare the transition rates vs. force between five molecules each of junctions *XR* and *XR*-long each and shows that junction *XR*-long exhibits much greater changes in rates for the same magnitude of force (also compare $\Delta x_f^{\ddagger}$ and $\Delta x_b^{\ddagger}$ in Table 5.1). Since the persistence length of double stranded DNA is about 50 nm (~ 150 bp) [190] the lever arm effect can probably be extended by another factor of five for arms of ≥ 100 bp. That is, forces as low as 0.1 pN would be enough to influence the junction conformations, illustrating the exquisite force sensitivity of the HJ.

5.3.4 Mapping the Reaction Energy Landscape of HJ

Since the effect of force depends on the arm lengths, the most natural reaction coordinates are angular. The angles that define the global shape of the junction are ϕ, the interhelical angle between two stacked pairs of helices, and ψ, the angle that measures the degree of unstacking of stacked helices [191] (Figure 5.6B). For example, for a stacked-X structure ϕ=40° and ψ=0° [173], while for an open structure, ϕ is 0° and ψ is 90° (Figure 5.6C). These two angles are well-defined within the angular space in which identities of stacking pairs are maintained. Our aim here is to deduce the structure of the transition state by determining the ϕ and ψ values of the transition state using a geometrical analysis. The analysis below estimates the angles (ϕ_{II}, ψ_{II}) of the transition state *ts*II in the *iso*II half of the conformational reaction coordinate, but the same conclusions hold for *ts*I. *ts*II lies a third of the way from *iso*II to *iso*I along the d_{XR} coordinate (Table 5.1, Figure 5.6A). We can show that this condition is satisfied for a collection of (ϕ_{II}, ψ_{II}) values, starting from (70°, 0°) at one extreme and arriving at (0°, 70°) at the other (Figure 5.6C, gray zone, see also section 5.4 *Experimental Procedures*). In order to obtain an additional constraint, we performed an equivalent force analysis on junction *BR* (Figure 5.4E, 5.4F, Table 5.1). Junction *BR* exhibited much reduced (by 5-6 fold) force dependence of the equilibrium populations compared to junctions *XR* and *HR* (compare Δx_{eq} values in Table 5.1). The residual force dependence of the equilibrium populations may be attributed to the finite diameter of the DNA duplex (Supporting Online Materials). In contrast to junctions *XR* and *HR*, application of force on junction *BR* accelerated both forward and backward transitions (Figure 5.4F). Therefore, the distance between the ends of B and R arms, d_{BR} , must be larger in the transition state than in the stacked-X structures. This condition is satisfied only if ϕ_{II} in the transition state is smaller than the 40° of the stacked-X structure. Furthermore, the distance to the transition state is 0.37 nm at minimum which constrains ϕ_{II} to be essentially zero (see section 5.4 *Experimental Procedures*). In combination, our best estimate is $(\phi_{\mathrm{II}}, \psi_{\mathrm{II}})_{ts}$= (0°, 70°) for *ts*II (Figure 5.6C). This transition state is similar to the open state, but with arms deviating by about 20° from the ideal open state while displaying signatures on which pairs of helices are nearly stacked over each other (Figure 5.6D). The structure bears a strong resemblance to the HJ structure bound to the Cre recombinase [192]. Following the same argument, we can deduce that the transition state in the *iso*I-like conformational space, *ts*I, also has $(\phi_I, \psi_I)_{ts}$= (0°, 70°).

By probing the HJ dynamics in response to pulling forces in three different directions, we mapped the location of the transition states in the two-dimensional reaction landscape and deduced the global structure of the transient species populated during the HJ conformational changes. Our simplest model envisions a shallow minimum between the two transition states, depicted as the open structure (Figures 5.6A and 5.6D), but it is also possible that a continuum of conformations exist, spanning from *ts*I and *ts*II with nearly identical free energies, instead of having a single well-defined minimum.

5.3.5 Laser-Induced Heating from Optical Tweezers

A laser beam has a high power density at its focus position and hence may generate a significant amount of localized heating at the laser focus[193]. In our case, the typical laser intensities are 300-800 mW for the 1064 nm trapping laser and 2-3 μW for the 532 nm excitation laser. Considering that 300-800 mW is fairly high, we tested the heating effect by the 1064 nm trapping laser. Taking advantage of the fact that HJ dynamics are very sensitive to temperature, we compared the transition rates of HJ in the absence and presence of the IR trapping laser. In an actual fluorescence-force spectroscopy exeperiment, the HJ molecule was placed 13 μm or larger distances away from the IR laser focus (i.e. the trap center). Therefore, we obtained the FRET time traces from a HJ molecule with and without the the IR beam placed away by 13 μm. In Table 5.2, we summarize the average and standard deviation of the transition rates in the absence and presence of IR laser. Indeed, both the forward and backward transition rates increase up to ~1.5 folds. Since the enthalpic barrier determined from temperature dependent studies of the junction of same sequence was 110 kJ/mole [194], 50% increase in rate corresponds to about 2-3° C increase in temperature induced by the trapping laser.

We can also obtain the transition rates of junction *XR*, *HR* and *XR*-long at zero force by extrapolating the fit in Figures 5.4B and 5.4D to zero force and compare the rates for zero-force extrapolation with those for free forms of the junctions (without λ-DNA attached) in Table 5.3. The data in Table 5.3 show that the zero force extrapolation yields rates are 3 to 4 times higher for the forward reaction and 1.5 to 3.5 times higher for the backward reaction, than those for free forms of the junctions. This is consistent with the result shown in Table 5.2 where up to 1.5 times increase in rates were observed from laser heating. The remaining differences may have multiple origins, for example, (1) λ-DNA may tug on the junction continually even in the absence of applied force, (2) λ-DNA may alter the electrostatic environment of the junction. We note that the conformer transition rate can vary by more than two orders of magnitude when the ionic conditions are changed [195].

5.4 Experimental Procedures

Sample assembly

Nonspecific binding of the DNA and beads was prevented using cover slips coated with poly-ethylene glycol as previously described[196]. The sample chamber was sequentially incubated with (1) neutravidin (0.25 mg/ml) for 10 min, 2) blocking buffer containing tRNA (1 mg/ml) and BSA (1 mg/ml) for 1 h, 3) junction- λ-DNA (50 pM in HJ) for 40 min, 4) a solution of anti-digoxigenin coated bead for 30 min, and 5) imaging buffer comprising 10 mM Tris (pH 8.0), 5 mM NaCl, 10 mM $MgCl_2$, 1 mg/ml BSA, 1mg/ml blocking DNA, 0.04 mg/ml anti-digoxigenin, 0.4 % (w/v) D-glucose (Sigma), 165 U/ml glucose oxidase (Sigma # G2133), 2170 U/ml catalase (Roche # 10106810001), and 1 mM Trolox (Sigma) [188]). Steps 3-5 were carried out using a syringe pump to minimize DNA shearing.

Experimental Scheme and Data Analysis

The tethered position of the trapped bead was determined with an accuracy greater than 100 nm by finding the central position of the stretching curves in two orthogonal directions in the sample plane. The force-extension curves were used to determine the extension required to achieve the desired stretching force. Before collecting the data a more accurate central position of the molecule was determined from the confocal image of single-molecule fluorescence from the HJ displaced 13 μm from the trap center. At different stretching lengths, single-molecule fluorescence signals were collected for 10 s at room temperature with 5 ms (junction BR) and 10 ms (all others) time resolution. The measurements were repeated for the same molecule until photobleaching. The confocal beam was programmed to follow the motion the HJ using the mapping generated between the sample scanning and beam scanning. To determine transition rates at different forces, hidden Markov modeling was used as described previously [189] .

DNA Sequences for the Four Different Holliday Junction Structures

Junction XR

b-strand: 5’-/Cy5/ CCC TAG CAA GCC GCT GCT ACG G-3’
h-strand: 5’-/Cy3/ CCG TAG CAG CGC GAG CGG TGG G-3’
r-strand: 5’-/biotin/ CCC ACC GCT CGG CTC AAC TGG G-3’
x-strand: 5’-GGG CGG CGA CCT CCC AGT TGA GCG CTT GCT AGG G-3’

Junction XR-long

b-strand: 5’-/Cy5/ CCC TAG CAA GCC GCT GCT ACG G-3’
h-strand: 5’-/Cy3/ CCG TAG CAG CGC GAG CGG TGG GCG AAC GCT TA-3’
r-strand: 5’-/biotin/ TAA GCG TTC GCC CAC CGC TCG GCT CAA CTG GGA CCG TTT CGT-3’
x-strand: 5’-GGG CGG CGA CCT ACG AAA CGG TCC CAG TTG AGC GCT TGC TAG GG-3’

Junction HR

b-strand: 5’-/Cy5/ CCC TAG CAA GCC GCT GCT ACG G /Cy3/-3’
h-strand: 5’-GGG CGG CGA CCT TTT CCG TAG CAG CGC GAG CGG TGG G-3’
r-strand: 5’-/biotin/ CCC ACC GCT CGG CTC AAC TGG G-3’
x-strand: 5’-CCC AGT TGA GCG CTT GCT AGG G-3’

Junction BR

b-strand: 5' - /5Phos/GGG CGG CGA CCT CCC TAG CAA GCC GCT GCT ACG G - 3'
h-strand: 5' - /5Cy3/CCG TAG CAG CGC GAG CGG TGG G - 3'
r-strand: 5’- /biotin/ CCC ACC GCT CGG CTC AAC TGG G-3’
x-strand: 5' - CCC AGT TGA GCG CTT GCT AGG G/3Cy5Sp/ - 3

Sample Preparation

DNA strands were purchased from IDT DNA (Coralville, IA). The Holliday junctions were annealed as follows. Biotinylated (10 μM) and non-biotinylated strands were mixed in 1:1.2 molar ratio in a buffer containing 10 mM Tris (pH 8) and 50 mM NaCl. The mixture was cooled on a heating block from 90 ºC to room temperature over the course of 3 ~ 4 hours. Then λ-DNA was annealed to the small HJ molecules and anti-digoxigenin beads were made as described in Chapter 2.

Geometrical Model of Holliday Junction in Angular and Cartesian Coordinates

Here, we describe a simplified geometrical model that depicts the HJ conformation using two angular coordinates. Starting from this configuration shown, bend 1 and 2 out of the page by $\psi/2$ each, and 3 and 4 into the page by $\psi/2$ each. Assuming each arm length is 1,

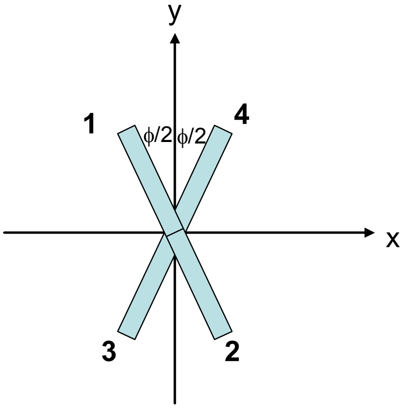

1: $\left(-\cos\frac{\psi}{2}\sin\frac{\phi}{2}, \cos\frac{\psi}{2}\cos\frac{\phi}{2}, \sin\frac{\psi}{2}\right)$

2: $\left(\cos\frac{\psi}{2}\sin\frac{\phi}{2}, \cos\frac{\psi}{2}\cos\frac{\phi}{2}, \sin\frac{\psi}{2}\right)$

3: $\left(-\cos\frac{\psi}{2}\sin\frac{\phi}{2}, -\cos\frac{\psi}{2}\cos\frac{\phi}{2}, -\sin\frac{\psi}{2}\right)$

4: $\left(\cos\frac{\psi}{2}\sin\frac{\phi}{2}, \cos\frac{\psi}{2}\cos\frac{\phi}{2}, -\sin\frac{\psi}{2}\right)$

From these coordinates, we can easily calculate the distance between two ends of any pair of helices. For example, d_{HR}, the distance between the ends of arms H and R, in *iso*I would be given by the distance between points 1 and 4 above multiplied by the effective arm length L_{eff}. Likewise, d_{BR} in *iso*I would be given by the distance between points 1 and 3 above multiplied by L_{eff}. In this model, d_{HR} in *iso*I would be identical to d_{XR} in *iso*II and d_{BR} would be identical in *iso*I and *iso*II. These are good assumptions as long as one strand being pulled is an exchanging strand and the other strand being pulled is a continuous strand which was true for junctions *XR* and *HR*, but not for junction *BR*. In fact, in junction *BR*, d_{BR} is expected to be larger in isoI where both of the pulled strands are the continuous strands (therefore at the outer sides of the HJ for 11 bp long arms) than in *iso*II where both of the pulled strands are the exchanging strands (therefore at the inner sides of the HJ). This expectation is consistent with our observation that *iso*I is favored at higher forces for junction *BR*.

Estimating ϕ and ψ Angles at the Transition State

Our data presented in the paper is not consistent with a single transition state that is valid regardless of pulling direction. Rather, our data suggest that the configuration of the transition state depends on the pulling direction. A possible explanation for this effect is the existence of two transition states of equivalent free energy, each belonging to the angular coordinate space defined by the stacking configurations, I and II. In such a model, applying tension in the direction that favors isoII (as in junction *HR*) will lower the free energy of the transition state belonging to ($\phi_{\mathrm{II}}, \psi_{\mathrm{II}}$) space, termed *ts*II, relative to that of the transition state belonging to ($\phi_{\mathrm{I}}, \psi_{\mathrm{I}}$) space, termed *ts*I, such that $\mathrm{T_I}$ becomes the single transition state (Figure 5.6A). Likewise, applying tension in the direction that favors *iso*I (as in junction *XR*) would result in *ts*II becoming the single transition state.

Below, we describe how we determined the ϕ and ψ angles in the transition state from our data. We restrict our discussion to junction *XR* but the same argument applies to junction *HR*. Here, we used a simple geometrical model described in the previous section. For a junction with effective arm length L_{eff}, the distance change between the *iso*I and *iso*II, $\Delta x_{eq} = 2L_{eff}\left(1-\sin\frac{\phi_0}{2}\right)$ where ϕ_0 is for the stacked-X structure. Using ϕ_0=40° and Δx_{eq}=4.4 nm from the data, we obtain L_{eff}=3.4 nm. We note that this effective length of each arm we deduced is similar to 3.7 nm length calculated by multiplying 11 bp arm length by 0.34 nm of crystallographic base pair length. Since the transition state is in the *iso*II half of the phase space, we need to find ($\phi_{\mathrm{II}}, \psi_{\mathrm{II}}$) such that distance from *iso*II to *ts*II, $2L_{eff}\left(\sqrt{\cos^2\frac{\psi_{II}}{2}\sin^2\frac{\phi_{II}}{2}+\sin^2\frac{\psi_{II}}{2}}-\sin\frac{\phi_0}{2}\right)$ is equal to $\Delta x_b^{\ddagger}$=1.5 nm. There is a combination of ($\phi_{\mathrm{II}}, \psi_{\mathrm{II}}$) values that satisfy this relation, starting from (70°, 0°) at one extreme and arriving at (0°, 70°) at the other (Figure 5.8A).

In order to obtain an additional constraint, we measured junction *BR*. This construct gave increase in both forward and backward rates with force. Acceleration in rates with force means that the distance between the two ends of the B and R arm is larger in the transition state than in the stacked-X structures. The distance between the two ends of B and R arms is given by $2L_{eff}\left(\sqrt{\cos^2\frac{\psi_{II}}{2}\cos^2\frac{\phi_{II}}{2}+\sin^2\frac{\psi_{II}}{2}}\right)$ which is relatively insensitive to ψ_{II} for $\phi_{\mathrm{II}} < 70°$, and is larger than its value in *iso*II, $2L_{eff}\cos\frac{\phi_0}{2}$, only if $\phi_{\mathrm{II}} < \phi_0$. Therefore, the fact that the transition rates increase with force itself already restricts ϕ_{II} to below 40 °. How much below depends on the distance to the transition state. The minimum distance to the transition state we estimated for junction BR is 0.37 nm. The equivalent distance in our model is $2L_{eff}\left(\sqrt{\cos^2\frac{\psi_{II}}{2}\cos^2\frac{\phi_{II}}{2}+\sin^2\frac{\psi_{II}}{2}}\right)-2L_{eff}\cos\frac{\phi_0}{2}$ which increases with deceasing ϕ_{II}. Here, it is uncertain which value should be used for L_{eff} because the pulling direction does not define a reaction coordinate that is valid from *iso*I all the way to *iso*II as revealed by a large discrepancy between Δx_{eq} and $(\Delta x_b^{\ddagger} + \Delta x_f^{\ddagger})$ (Table 5.1). Here, we set L_{eff} to the 11 bp arm length, 3.7 nm. Then, the maximum value of $2L_{eff}\left(\sqrt{\cos^2\frac{\psi_{II}}{2}\cos^2\frac{\phi_{II}}{2}+\sin^2\frac{\psi_{II}}{2}}\right)-2L_{eff}\cos\frac{\phi_0}{2}$ is 0.35 nm when $\phi_{\mathrm{II}}=0$ (Figure 5.8B), and this becomes smaller for smaller L_{eff}. Therefore, in order to account for the finite distance to the transition state, ϕ_{II} needs to be essentially zero.

Combining results from *XR* and *BR* analysis, we conclude that in the transition state *ts*II, $(\phi_{\mathrm{II}},\psi_{\mathrm{II}})_{\mathrm{ts}}$= (0°, 70°). This transition state is similar to the open state but with arms veering off by about 20° from the ideal open state. Following the same argument, we can deduce that for the transition state in the *iso*I-like phase space, $\mathrm{T_I}$, has the $(\phi_{\mathrm{I}},\psi_{\mathrm{I}})_{\mathrm{T}}$= (0°, 70°) as well.

We also note that the equilibrium between the two states does shift with force for junction *BR*. Δx_{eq} is 0.7 nm favoring *iso*I. This value is about 5-6 times lower than those of junctions *XR* and *HR*, confirming our prediction that there will not be as big a change in conformational bias with force for junction *BR*. We suggest that the residual bias we detect here is due to the finite diameter effect of the duplex arms which is amplified for junction *BR* because two pulling strands are either both exchanging strands (*iso*II) or both continuous strands (*iso*I). The ends of the pulling strands are therefore expected to be farther apart in isoI than isoII thereby leading to the increased relative population of *iso*I upon force application. Such an effect due to the finite DNA duplex diameter would be much less pronounced in junctions XR and HR because in both conformations, one pulling strand is an exchanging strand and the other is a continous strand.

5.5 Conclusions

Unlike DNA or RNA hairpins, where forces on the order of 15 pN are necessary to induce mechanical unzipping [185,186], the conformations of HJs could be biased at 0.5 pN or lower. The lever arm effect makes it unlikely that a purely mechanical tool could have probed the force effect on HJ conformations because if the arms are lengthened to magnify the distance change, the force effect will occur at even lower forces. FRET can also report on vectors other than the end-to-end distances which we exploited here by pulling on *XR*, *HR* or *BR* arms while simultaneously measuring the same HB vector via FRET, which led to the two dimensional mapping of reaction landscapes. The development reported here expands on the current arsenal of hybrid single molecule techniques combining force and other observables [183,197-199]. Our method is readily applicable to other nucleic acids systems and their interaction with proteins and enzymes, and with the advent of new orthogonal labeling techniques, should be extendable to proteins and protein complexes. The next technical challenge would be to obtain time evolution of the end-to-end distance by force, for example due to the action of DNA processing enzymes [200], and correlate it with the enzyme conformational changes simultaneously measured via fluorescence.

5.6 Figures and Tables

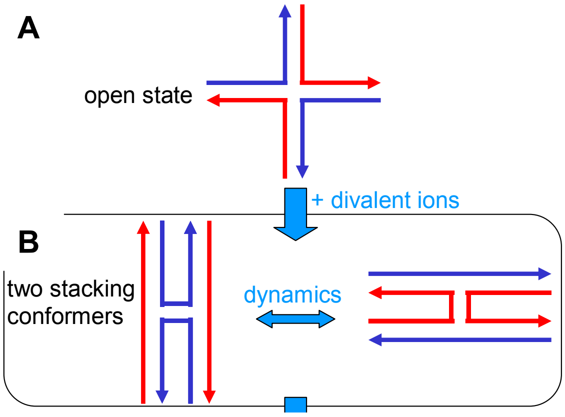

Figure 5.1 Structure diagrams of a Holliday junction in the (A) absence and (B) presence of divalent ions.

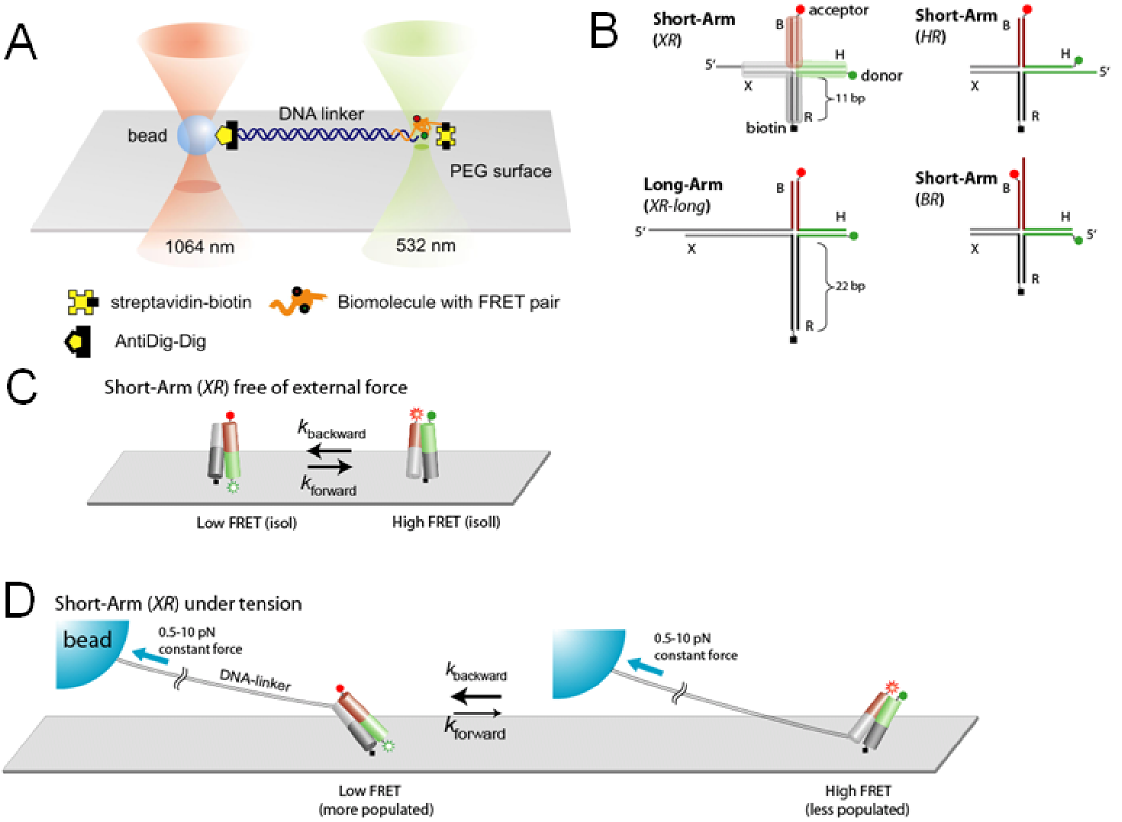

Figure 5.2 Holliday junction constructs and experimental scheme. (A) A surface-immobilized biomolecule with FRET labeling is connected to a trapped bead via a long DNA linker. The linker DNA spatially separates the confocal beam (532 nm) from the trapping beam (1064 nm) such that enhanced photobleaching and an overwhelming

background signal induced by the intense trapping laser are avoided. To apply force, the surface immobilized molecule was moved relative to the trapped bead. The confocal beam was programmed to follow the motion of the molecule using the mapping generated between sample scanning and beam scanning as described in Chapter 2. (B) Junction *XR* is known to alternate between two different stacking conformers, *iso*I (Low FRET) and *iso*II (High FRET) with similar populations in both states. (C) The HJ species studied. Junction *XR* comprises four arms of 11 base pairs (bp), termed B (red), H (green), R (dark gray) and X (gray). Cy3 and Cy5 fluorophores are terminally attached to H and B arms respectively, and the molecule is tethered to the surface through biotin attached to the end of the R arm. Stretching force is applied through the λ-DNA linker hybridized to the X arm. In junction *XR*-long the lengths of arms R and X are increased to 21 bp. In junction *HR* the λ-DNA linker is hybridized to the H arm. In junctions *HR* and *BR* the λ-DNA linker is hybridized to the H and B arms respectively. (D) Force is expected to bias the junction *XR* to *iso*I which possesses a larger separation between the two tether points than *iso*I.

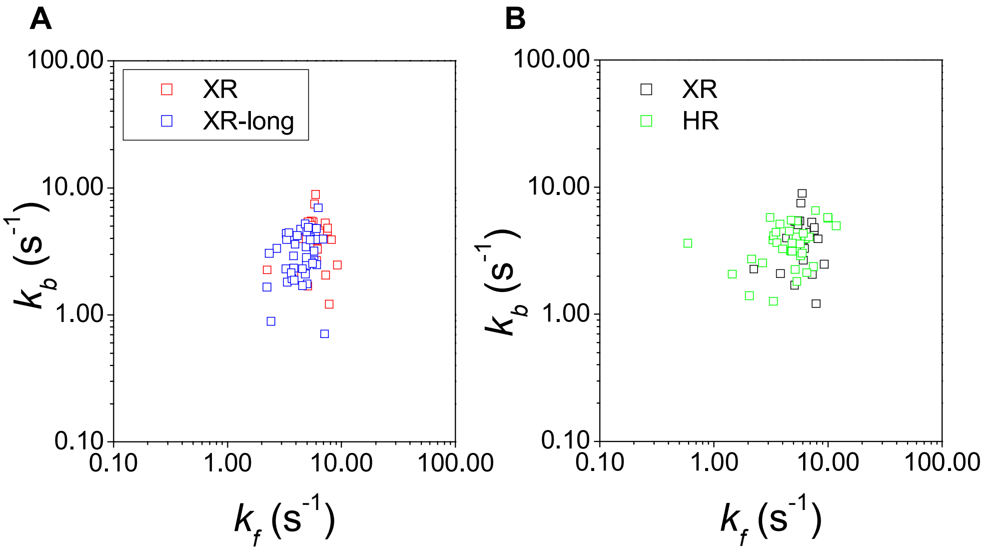

Figure 5.3 Dynamics of the three different Holliday junction structures at zero force. (A) Scatter plot of transition rates of junctions *XR* and *XR*-long. (B) Scatter plot of transition rates of junctions *XR* and *HR*. All the data were obtained without a λ-DNA attached and in the absence of trapping laser beam, but otherwise in identical solution conditions.

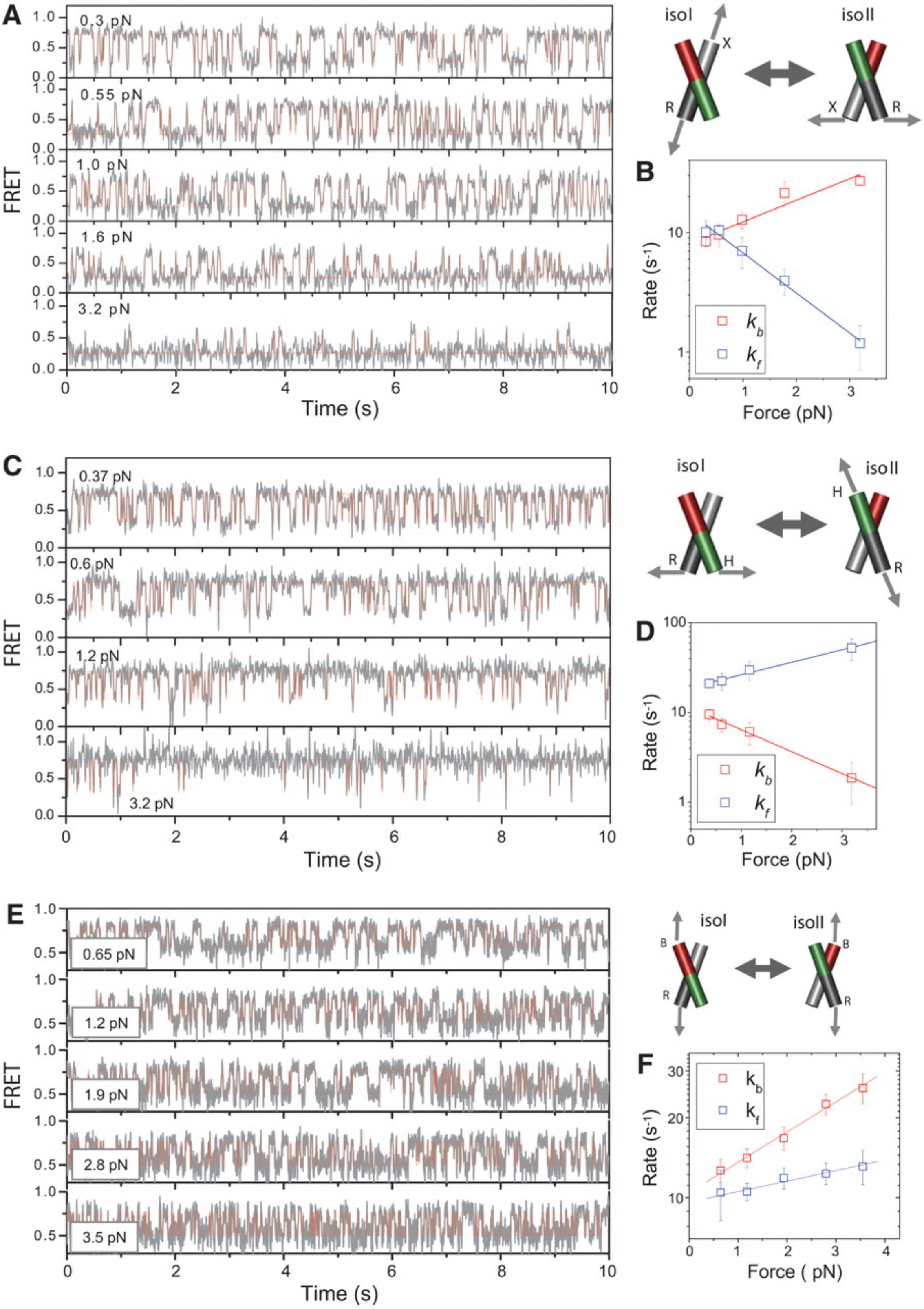

Figure 5.4 Conformer exchange dynamics of the HJ as a function of applied force. (A)

FRET time traces (gray lines) of a single junction *XR* molecule at different forces. FRET efficiency is approximated by the acceptor intensity divided by the sum of the donor and acceptor intensities. Red lines are the most likely FRET trajectories generated via hidden Markov modeling. The imposed force (indicated on the top left of each plot) increases top to bottom. (B) Log-linear plot of rate constants of conformer exchange as a function of force. Rates of transitions from states *iso*II to *iso*I (k_b red) and *iso*I to *iso*II (k_f, blue) are differentiated by color. Error bars represent standard deviations obtained from repeated measurements of the same molecule. From linear fitting, we found that the transition state is closer to *iso*II (1.5 nm) than to *iso*I (2.9 nm). (C) Same as (A) but for a single junction *HR* molecule. (D) Same as (B) for a single junction *HR* molecule. (E) Same as (A) and (C) but for a single junction *BR* molecule. (F) Same as (B) and (D) but for a single junction *BR* molecule.

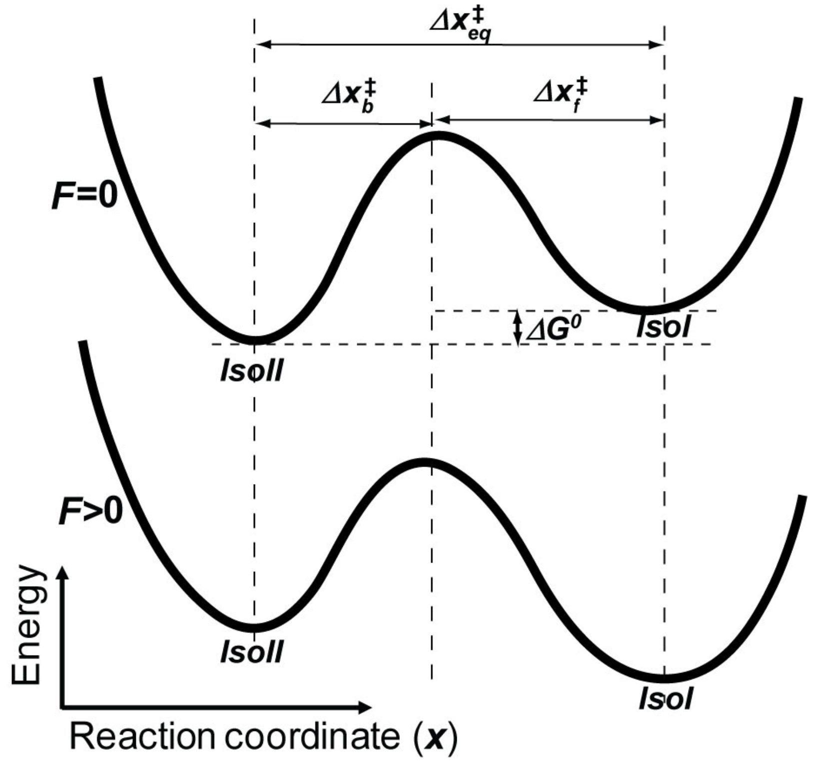

Figure 5.5 Energy landscape for a two-state system along the reaction coordinate. The applied force (*F*) tilts the energy landscape linearly.

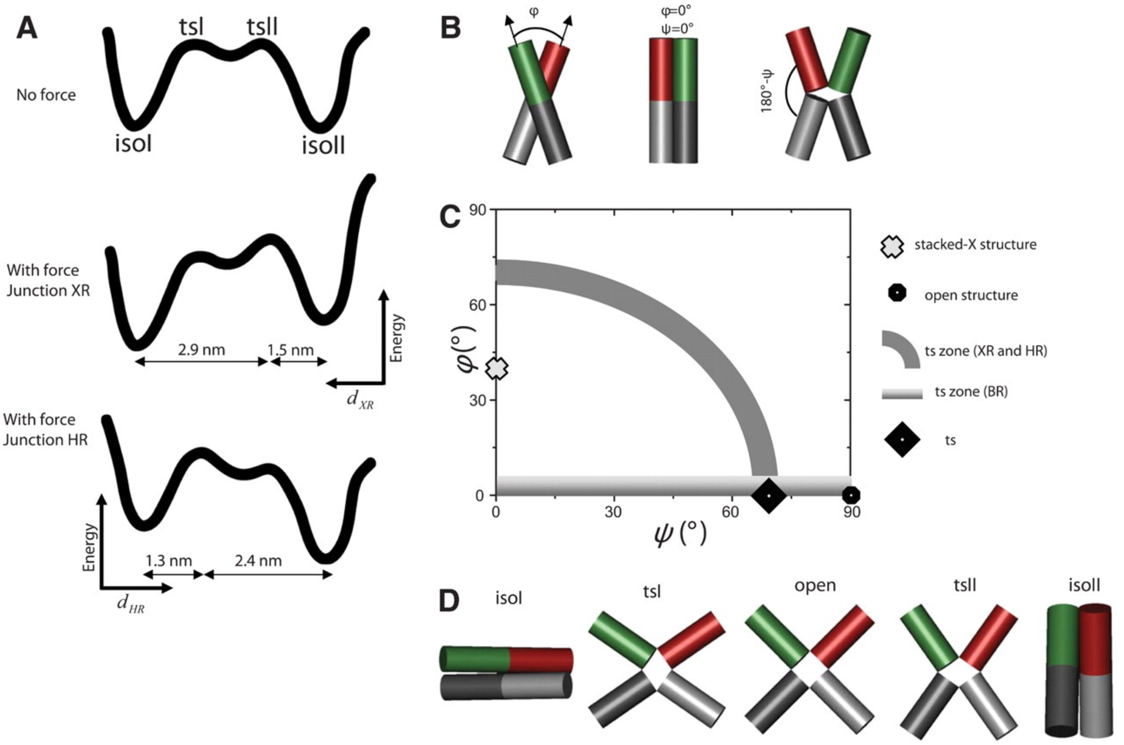

Figure 5.6 Mapping the reaction landscape and determining the transition state structure. (A) A proposed reaction landscape with two distinct transition states with nearly identical energies (top). In junction *XR*, the applied force would tilt the energy landscape toward *isoI* so that the transition state, *ts*II, nearer to *iso*II would become the state of highest energy along the entire coordinate (middle). The reaction coordinate here is the distance between the ends of X and R arms, d_{XR}, which increases to the left as shown. Similarly, in junction *XR*, the transition state, *ts*I, nearer to *iso*I would become the single transition state upon application of force. The reaction coordinate here is the distance between the ends of H and R arms, d_{HR}, which increases to the right. (B) Two angular coordinates ϕ and ψ define the global conformation of the HJ. (C) Two-dimensional conformational space of HJ conformations. The stacked-X structure and open structure are marked. The gray arc represents a zone that satisfies experimental constraints derived from *XR* and *HR* data, and the gradient zone is derived from *BR* data. The consensus location of the transition state is marked with a diamond. (D) Global structures of *iso*I, *iso*II and two transition states, *ts*I and *ts*II, plus an open structure.

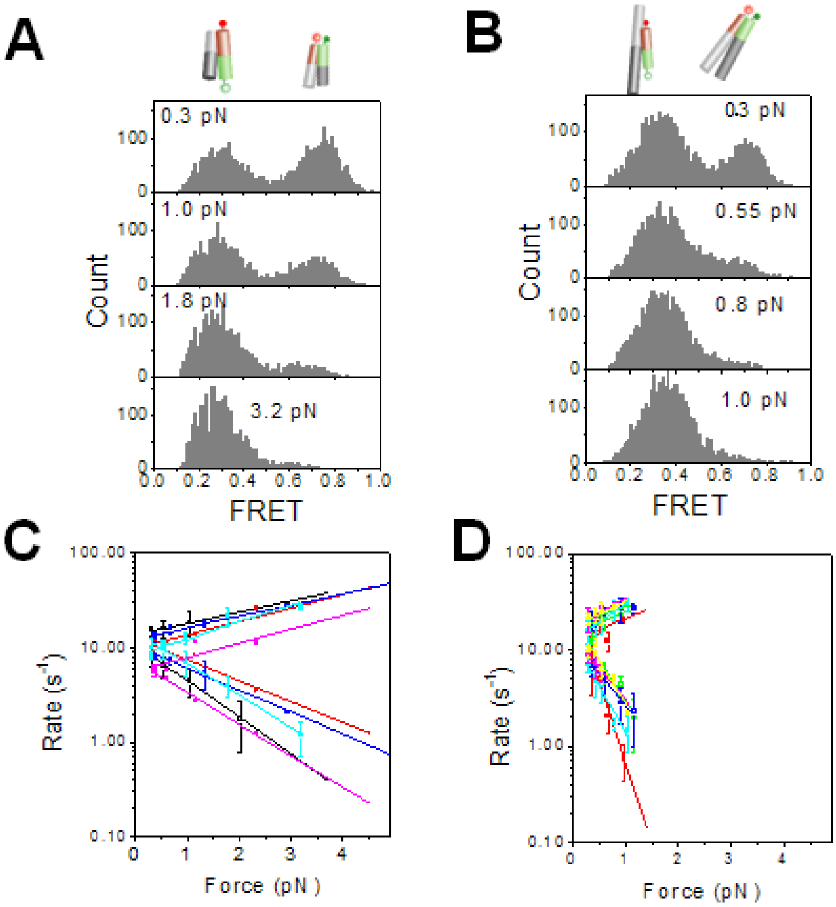

Figure 5.7 A lever arm effect. In junction *XR*-long, arms *X* and *R* (*i.e.* the arms through which the force is applied) have been extended to 21 bp in length compared to 11 bp in junction *XR*. (A) FRET histograms of a single junction XR at different forces. Junction *XR* is almost completely biased to *iso*I at ~ 5 pN. (B) FRET histograms of a single junction *XR*-long at different forces. Complete biasing to *iso*I already occurs below 2 pN. (C) Rate constants of conformer exchange are plotted as a function of force for 5 different *XR* molecules. Different molecules are marked by different colors. Backward reaction rates from *iso*II to *iso*I were represented in solid data point and forward rates from *iso*I to *iso*II in open data points. Linear fits are also shown in the figure. Error bars representing s.e.m are added when possible (i.e., when the force dependence measurements were made more than once because photobleaching did not terminate the experiment after one cycle). (D) Data for XR-long generated in the same as in (C). It is clear that *XR*-long exhibits much greater changes in rates for the same range of applied force.

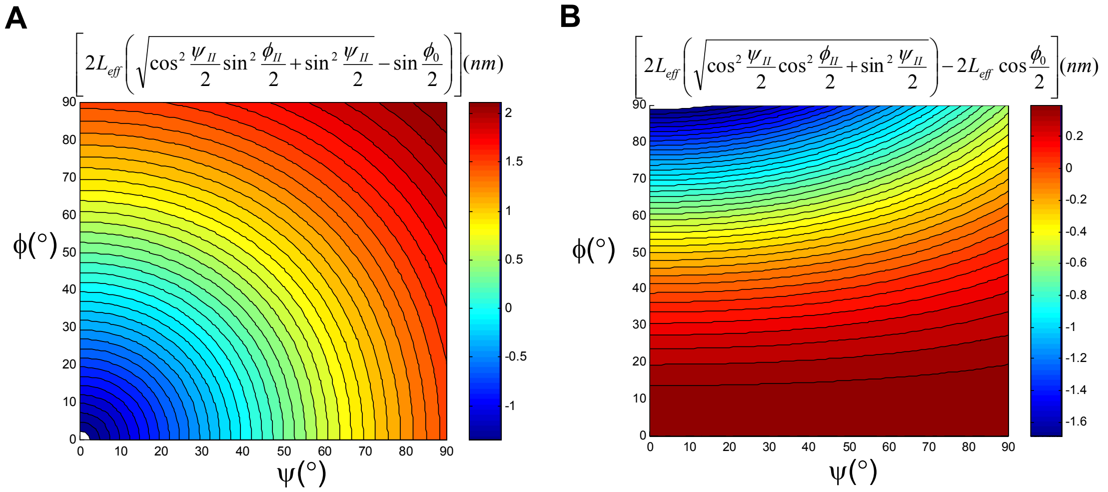

$\left[2L_{eff}\left(\sqrt{\cos^2\frac{\psi_{II}}{2}\sin^2\frac{\phi_{II}}{2}+\sin^2\frac{\psi_{II}}{2}}-\sin\frac{\phi_0}{2}\right)\right](nm)$

$\left[2L_{eff}\left(\sqrt{\cos^2\frac{\psi_{II}}{2}\cos^2\frac{\phi_{II}}{2}+\sin^2\frac{\psi_{II}}{2}}\right)-2L_{eff}\cos\frac{\phi_0}{2}\right](nm)$

Figure 5.8 Mapping the location of the transition states in the two-dimensional reaction landscape.

	XR	*XR*-long	*HR*	*BR*
$\Delta x_b^{\ddagger}$ (nm)	1.5 (±0.3)	2.6 (±0.6)	2.4 (±0.5)	1.1 (±0.2)
$\Delta x_f^{\ddagger}$ (nm)	2.9 (±0.6)	7.7 (±1.5)	1.3 (±0.3)	0.37 (±0.2)
Δx_{eq} (nm)	4.4 (±0.8)	9.9 (±2.6)	3.1 (±0.8)	0.7 (±0.2)
$\Delta x_b^{\ddagger}+\Delta x_f^{\ddagger}$ (nm)	4.4 (±0.8)	10.3 (±2.0)	3.6 (±0.5)	1.5 (±0.3)

Table 5.1 Distance to the transition state from *iso*I ($\Delta x_f^{\ddagger}$) and from *iso*II ($\Delta x_b^{\ddagger}$) measured from the force-dependent transition rates between *iso*I and *iso*II for four different junctions. Errors represent standard deviation from five different molecules each. Also shown is Δx_{eq}, the distance between *iso*I and *iso*II determined from force-dependent changes in the equilibrium constant. For junction *BR*, Δx_{eq} deviates significantly from ($\Delta x_b^{\ddagger}+\Delta x_f^{\ddagger}$) showing that d_{BR} is not a valid reaction coordinate connecting *iso*I and *iso*II. In contrast, $\Delta x_{eq}=\Delta x_b^{\ddagger}+\Delta x_f^{\ddagger}$ within error for junctions *XR* and *HR* showing that d_{XR} and d_{HR} are reaction coordinates valid from *iso*I to *iso*II.

	XR (free junction, no trapping laser)	*XR* (free junction, trapping laser on)
k_b (s^{-1})	4.7±1.4	6.2±1.9
k_f (s^{-1})	7.2±4.2	11.3±4.8

Table 5.2 Comparing the transitions rates in the absence and presence of the trapping laser. Trapping laser was focused 13 μm away from the HJ molecule when in presence.

	XR	*XR*-long	*HR*
k_b (s^{-1}) free junction	4.2±1.9	3.2±1.3	3.7±1.3
k_f (s^{-1}) free junction	6.1±1.6	4.6±1.2	5.0±2.4
k_b (s^{-1}) zero force	11±2.7	16±4.5	18±1.3
k_f (s^{-1}) zero force	9.9±3.3	16±2.5	11±1.9

Table 5.3 Comparing the transitions rates for zero-force extrapolation and for free forms of the junctions.

Chapter 6
Stretching Peptides and Proteins Using Fluorescence-Force Spectroscopy[††]

6.1 Introduction

In Chapters 2-5, we have shown applications of the fluorescence-force spectroscopy that we developed to study the effect of forces on protein-nucleic acid interactions as well as the effect of forces on the conformational dynamics of a nucleic acid structure. In this chapter, we extend its applications to monitor the conformations of a folded poly-peptide or protein in response to external forces.

As we have mentioned in Chpater 1, many force-based methods (AFM, optical tweezers, etc) have been used to stretch peptides [201-204] and proteins [23,24,47,48,76,77]. In order to apply forces to them, proper chemical reactions have to be utilized to covalently attach the peptide/protein to the force transducer (beads, AFM tips) through one tethering position on the peptide/protein and to a stiff surface through the other tethering position on the peptide/protein. Primary amino groups ($-NH_2$) and thiol groups (-SH) are natural components of peptides and proteins and are often used as the targets for such covalent attachments [205]. However, if we want to apply fluorescence-force spectroscopy to stretch peptide/protein, more covalent attachments have to be introduced to label the same peptide or protein with two fluorophores (a FRET pair) as well. It is extremely difficult to achieve four covalent attachments on the peptide/protein with high yield and this requires four different types of reactions for the attachments. Therefore, we have developed a simpler method to achieve this by covalently attaching two DNA handles carrying

---

[††] Part of this work has been published as papers:

- Grashoff, C., Hoffman, B. D., Brenner M. D., Zhou R., Parsons M., Yang, M. T., McLean, M. A., Sligar, S. G., Chen, C. S., Ha, T. & Schwartz, M. A. Measuring mechanical tension across vinculin reveals regulation of focal adhesion dynamics. *Nature* **466**, 263-266 (2010).
- Brenner, M. D., Zhou, R. & Ha, T. Forcing a connection: impacts of single-molecule force spectroscopy on in vivo tension sensing. *Biopolymers* **95**, 332-44 (2011).

fluorophores to the peptide/protein. The design is shown in Figure 6.1. Two cysteine residues are placed at the two ends of the peptide sequence of interest respectively. For proteins, the protein mutant carrying two exposed cysteine residues are generated through site-directed mutagenesis and the two cysteine positions are where the two DNA handles are attached. Two single strands of DNA with 5′-amine modifications are reacted with a heterobifunctional cross-linker succinimidyl 4-[N-maleimidomethyl] cyclohexane-1-carboxylate (SMCC) to produce maleimide-functionalized DNA handles which reacts with the two cysteine residues in the peptide or protein to generate a DNA-protein or DNA-peptide conjugate carrying two ssDNA handles. Next, the Cy3-strand and Cy5-biotin-strand of ssDNA are annealed to the previous product so that the DNA handles become double strands (Figure 6.1A). For fluorescence-force experiments, λ-DNA is then attached to the pre-annealed product as described in Chapter 2. Finally, the digoxigenin-labelled oligonucleotide complementary to the cohesive end-site of λ-DNA is added. Alternatively, Cecconi and coworkers also developed a similar method to attach two DNA handles to protein/peptide where a disulfide bond was generated between a thiol group present at the end of each DNA handle and a thiol group of a cysteine residue in the protein [206].

6.2 Calibrating the FRET-based *In-Vivo* Force Sensor

6.2.1 Calibrating a FRET-based *In-Vivo* Force Sensor

The first application for using our fluorescence-force spectroscopy to stretch single peptides is to calibrate a FRET-based *in-vivo* force sensor. Grashoff and coworkers developed a FRET-based tension sensor module that can be expressed inside the cell to report the forces transmitted from extracellular matrix to cytoskeleton through focal adhesions [101]. Focal adhesions are comprised of integrins (cell surface receptors), talin, vinculin and other proteins, connecting the extracellular matrix to actin cytoskeleton [207]. The transmission of the forces has been recently found significant to impact cell growth, differentiation, morphology and even protein expression inside the cell [208,209]. The FRET-based *in-vivo* tension sensor module (TSMod) that Grashoff and coworkers designed was to use two fluorophores, mTFP1 and venus (A206K) as donor and acceptor respectively, connected by a 40-amino-acid-long elastic peptide linker (Figure 6.2A). The elastic peptide linker was composed of eight repeats of amino acid motif GPGGA and was derived from the spider silk protein flagelliform which is composed of repetitive amino acid motifs [210]. If a force (or tension) is applied across the elastic TSMod, FRET efficiency should decrease because the distance between the two fluorophores increases (Figure 6.2A). Grashoff and coworkers applied this TSMod to report the force transmitted by vinculin, an intracellular force adhesion protein [101]. TSMod was inserted between the head and tail domains of the vinculin protein to form the vinculin tension sensor (VinTS) (Figure 6.2B). Vinculin consists of a head domain (Vh) that can connect to integrin through talin, and a tail domain (Vt) that can bind to the actin cytoskeleton. FRET values in the vinculin deficient cells expressing VinTS were determined using fluorescence lifetime imaging microscopy (FLIM) [211] with which the fluorescence of the fluorophores (mTFP1 and venus) can be differentiated from cellular autofluorescence more readily than with intensity-based measurements. The VinTS in the adherent cell showed longer fluorescence life times (corresponding to lower FRET efficiency; Figure 6.2B). However, a control construct, VinTL, containing the tension sensor module and vinculin head domain, but missing the tail domain required for interaction with the actin cytoskeleton, displayed only high FRET (Figure 6.2C; blue color, short mTFP1 lifetimes), indicating that VinTS was experiencing tension whereas VinTL is not.

Having known that VinTS indeed can detect the force that exists across the vinculin in the living cell, can we calibrate the TSMod inserted into the vinculin such that we can convert the FRET efficiency determined from FLIM into its corresponding forces? We therefore applied our fluorescence-force spectroscopy to calibrate TSMod. Fluorescent proteins have low photostability, which precludes single molecule FRET measurements. We therefore generated a version of TSMod using the organic fluorophores Cy3 and Cy5 (termed F40, Figure 6.3A). The Cy3-Cy5 FRET pair has a similar R_0 (Förster radius) as that of the mTFP1-venus FRET pair (~ 6 nm).The flagelliform linker (F40) was connected to a polymer-coated glass surface via 18 bp double-stranded (ds) DNA and to a bead held in optical tweezers through λ-DNA (Figure 6.1). Two DNA handles presented the fluorophores in close proximity to terminal cysteine residues of F40, allowing estimation of the linker end-to-end distance as a function of force from FRET measurements. FRET efficiency changes over multiple force cycles showed that F40 reached conformational equilibrium rapidly and displayed no hysteresis, indicating reversibility (Figures 6.3B). The zero force FRET efficiency of ~50% determined separately from single molecule TIR measurement (Figure 6.3C) matched the FRET value at the lowest force analyzed (0.25 pN, Figure 6.3D) indicating no adverse effects due to linkers or the optical tweezers. Together, these experiments showed that F40 is most sensitive at 1-6 pN (Figure 6.3C). These measurements were used to estimate the force sensitivity of TSMod, and to calculate forces across vinculin in living cells using FLIM microscopy data [101]. This analysis showed that the average force in stationary focal adhesions is ~2.5 pN [101].

6.2.2 Stretching Various FRET-based Force Sensors

In the design for stretching F40 (Figure 6.3), SMCC linkers, the terminal phosphate group at 5’end of DNA and the six-carbon chain for the amino modification of the DNA handles have to be considered but are actually not included in TSMod (we use a term ‘connecters’ later in this section to refer to those who are used to connect fluorophores to the elastic peptide but at the same time add some unwanted extension to the peptide length).Additionally, the radius of the flurophores should be considered as well. If the extension of the connecters greatly depends on the applied force as TSMod does, it would make the TSMod calibration inaccurate. In order to separate the extension changes of the connecters from that of the peptide as a function of applied force, we have to obstain the force-extension curves for several force sensor constructs containing different repeat numbers of the amino acid motif GPGGA. In addition, it would be useful to measure the FRET-force curves for different FRET-based force sensors containing different repeat numbers of the amino acid motif GPGGA, which should sense different ranges of forces using the FRET sensitive range (3-8 nm). We hereby made two more force sensors F25 and F50, containing five and ten repeats of GPGGA respectively. All the three force sensors (F25, F40 and F50) possess two terminal cysteine residues, which make them contain actually 27, 42 and 52 amino acids respectively (Figure 6.4A). Figure 6.4B shows the averaged FRET versus force curves for F25, F40 and F50 obtained from many stretching and relaxing cycles using fluorescence-force spectroscopy as we did in Figure 6.3B. In all the three force sensors, stretching and relaxing curves coincided and little hysteresis was observed. As mentioned in Chapter 3, we can use Equation (3.1) to convert FRET efficiencies to Cy3-Cy5 separation distance values and replot the same data in a different presentation of distance versus force (Figure 6.4C). All the three force sensors showed a linear elasticity as a Hooke's spring and the Cy3-Cy5 separation distance, $D_{total}(F)$ is given by

$$D_{total}(F) = a \cdot F + D_0 \qquad (6.1)$$

Where D_0 is the Cy3-Cy5 separation distance at zero force for the force sensor and a is the compliance (the inverse of stiffness) of the force sensor. From the linear fits in Figure 6.4C, we obtained D_0 and a for each force sensor.

In Figure 6.4D, we plot a as a function of N, the number of amino acids in the force sensor (N=27 for F25, N=42 for F40 and N=52 for F50). A linear fit can well describe the data (the red line, Figure 6.4D) so we have

$$a = (\varepsilon \cdot N + \gamma) \text{ nm pN}^{-1} \qquad (6.2)$$

where $\varepsilon = 0.012 \pm 0.0006$ nm pN^{-1} per amino acid and $\gamma = 0.00013 \pm 0.018$ nm pN^{-1}, obtained from the linear fit (errors represent standard errors from the linear fit, confidence level is 0.95). We consider that the Cy3-Cy5 separation distance for each force sensor construct consists of two parts: 1) the end-to-end distance of the elastic peptide and 2) the extension of the 'connecters' (i.e. the sum of the two distances from one end of the peptide to the center position of the fluoropore near that end). $\varepsilon \cdot N$ is the only term in Equation (6.2) that shows linear dependence on N, indicating that it should represent the compliance of the peptide (the amino-acid chain). And the constant γ hence represents the effective compliance of the 'connecters' (SMCC linkers, etc), which should be a constant for all the three force sensor constructs. ε is then the compliance of the peptide per amino acid, which is 0.012 nm pN^{-1} per amino acid. The compliance of the connecters (0.00013 nm pN^{-1}) is very small and even the value of the standard error (0.018 nm pN^{-1}) is equal to the compliance of only one or two amino acids. This indicates that the connecter to link the fluorophore to the end of the peptide is relatively stiff and its total extension (i.e. the sum of the two distances from one end of the peptide to the center position of the fluoropore near that end) depends little on force in the force range tested (< 20 pN).

In Figure 6.4E, we next plot D_0 as a function of N, the number of amino acids in the force sensor. A linear fit can describe the data as well (the red line, Figure 6.4E) so we have

$$D_0 = (d \cdot N + l) \text{ nm} \qquad (6.3)$$

where $d = 0.044 \pm 0.0017$ nm is the average extension of one amino acid at zero force, which is much smaller than the contour length of one amino acid (~ 0.38 nm) and is only half the extension derived previously when assuming the peptide is a random coil [212]. $l = 3.76 \pm 0.06$ nm, presenting the total extension of the connecters at zero force, which is not a small number compared to the extension of the elastic peptide at zero force.

In summary, we successfully used fluorescence-force spectroscopy to obtain the FRET-force curves of three FRET-based force sensors. F25, F40 and F50 behave like a Hooke's spring and can report the forces up to ~5 pN, ~7 pN and ~14 pN, respectively. But the sensitivity in the detectable range is lower for the force sensor that has a larger detectable force range. If we put Equations (6.2) and (6.3) into Equation (6.1), we get

$$D_{total} = (\varepsilon \cdot N + \gamma) \cdot F + (d \cdot N + l) = (\varepsilon \cdot F + d) \cdot N + (\gamma \cdot F + l) = D_{peptide} \cdot N + D_{connecters} \qquad (6.4)$$

where we define $D_{peptide} = \varepsilon \cdot F + d$ as the average extension of one amino acid at the force F, and $D_{connecters} = \gamma \cdot F + l$ as the effective extension of the two connecters on the either end of the peptide. Our data suggest that the peptide tends to coil up and likely in a folded form whereas the connecters are more extended to their contour length even at zero force.

6.2.3 Experimental Procedures

Expression and purification of the flagelliform peptide linker for force calibration

The flagelliform linker sequence (F40) flanked by a sequence containing a single cysteine and a thrombin cleavage site was inserted into pGEX-4T3. BL21(DE3) pLysS competent cells were transformed and expression was induced with 0.5 mM IPTG. The cell pellet was lysed using 2 mg/mL lysozyme and affinity purification of GST-F40 was performed using GSTrap 4B prepacked columns (GE Healthcare). GST-F40 was eluted in 10mM glutathione and thrombin was either added directly to a final concentration of 10mg/mL for 6h at 4°C, or elution fractions were frozen at -80°C. The thrombin/GST-F40 mixture was then separated by size exclusion on a Superdex75 column and further purified with reverse phase chromatography. The F40 peptide elution peak was analyzed and confirmed by mass spectrometry and speed vacuumed to dryness.

Preparation of the force sensors for fluorescence-force spectroscopy

Two handle DNAs with 5’-amine modifications (5’-CCC ACG CGC GACTAC CCA GC -3’ and 5’-GCC TCG CTG CCGTCG CCA-3’) were reacted with 200x molar excess of succinimidyl 4-[N-maleimidomethyl]cyclohexane-1-carboxylate (SMCC). Unreacted SMCC was removed by fast protein liquid chromatography (FPLC) purification and modified DNA handles were incubated with dried F40 peptide (1:1) in 50mM Tris buffer (pH 7.5) overnight at 4˚C. Annealing with Cy3- and Cy5-labelled strands was performed by incubation of 250 pmol of the DNA modified peptide (the force sensor), 250 pmol of biotinylated strand (5’-/biotin/-TGG CGA CGG CAG CGA GGC -/ Cy5/ 3’) and 250 pmol of single-stranded (ss) DNA containing a λ-DNA cos site (5’-GGG CGG CGA CCT GCT GGG TAG TCG CGC GTG GG/Cy3/-3’) in 10mM Tris-HCl (pH 8.0) and 50mM NaCl overnight at room temperature. For fluorescence-force experiments, λ-DNA (Promega) was attached to the pre-annealed product as described previously. Subsequently, the digoxigenin-labelled oligonucleotide complementary to the cohesive end site of λ-DNA was added (5’-AGG TCG CCG CCC TTT /digoxigenin/-3’). Thus, the complete construct for the force sensor calibration contained a single digoxigenin-tag on λ-DNA and a biotin-tag at the DNA-peptide conjugate.

Fluorescence-force spectroscopy

A sample assembly protocol for the fluorescence-force experiment was described in Chapter 2. Briefly, a solution of 50pM force sensor construct was immobilized on a coverslip surface coated with polyethyleneglycol, which eliminated non-specific surface adsorption of proteins and reduced surface interactions with DNA and microspheres[9]. The immobilization was mediated by biotin-Neutravidin binding between the biotinylated force sensor, Neutravidin, and biotinylated polymer. Next, anti-digoxigenin-coated 1μm polystyrene beads were added so that one bead could attach to the free end of each tethered molecule. For imaging, the buffer was: 10mM Tris (pH 7.5), 1x PBS, 0.5 % (wt/vol) D-glucose (Sigma), 165 U/ml glucose oxidase (Sigma), 2170 U/ml catalase

(Roche), 3 mM Trolox (Sigma), and 0.1% (vol/vol) Tween 20 (Sigma). All single molecule fluorescence-force experiments were performed at 22 ± 1°C. Once a tethered microsphere was trapped, the sample was moved in two orthogonal directions with the piezo-stage to roughly determine the tethered position of the peptide construct. The piezo-stage was then moved back and forth between a starting position (typically 13.5μm or 14μm separation between the tethered point and the trap centre) to an end position (16.8-16.9μm) at a constant speed of 455nm s^{-1} for several cycles. The confocal excitation beam was programmed to follow the motion of the tethered force sensor molecule so that the donor (Cy3) and acceptor (Cy5) fluorescence intensities were recorded with 44ms time resolution as a function of applied force.

Single-molecule TIR spectroscopy

Wide-field prism-type total internal reflection (TIR) spectroscopy described previously [9] was used to determine the zero force FRET value of the Cy3/Cy5 sensor in the same imaging buffer as used in fluorescence-force spectroscopy. A single-molecule FRET histogram was generated by averaging for 300 ms. Background, cross-talk and gamma corrections were considered for calculating the FRET efficiency [9].

6.3 Stretching Single Proteins

To further extend our fluorescence-force spectroscopy to stretch single proteins, we used the same strategy to link two DNA handles to IκBα, a protein that binds to and inhibits the NFκB transcription factor, which activates hundreds of genes [213]. IκBα contains six ankyrin repeat (AR) domains, a ~33-amino-acid structural motif that generally adopts a helix-loop-helix-β-hairpin/loop fold, among which four ARs (ARs 1–4) are structureally stable and two ARs (AR5–6) are weekly folded (or disordered). The two weakly folded ARs are crucial because they regulate the intracellular life time of IκBα and stabilization of the AR5–6 region (either upon NFκB binding to IκBα or return AR6 to the consensus sequence for stable ARs by mutating two residues Y254L/T257A) lengthened the intracellular half-life of IκBα [213,214]. The mechanical unfolding of ankyrin repeats have been investigated at the single protein level where the stately folded ankyrin repeats were unfolded at ~37 pN and refolded at ~32 pN [215,216].

In order to make the DNA handle linkage, we replaced wilde typle cysteins IκBα with serines introduced cysteine residues into a cysteine-free construct of IκBα: 1) one is at residue E128 in AR 2 (or at residue S166 in AR 3); 2) the other is at residue S262 in AR 6. The protein preparation procedures were described previously and this IκBα (hereafter referred to as IκBα) retained the function to bind to NFκB [213]. We followed the protocols used for generating the force sensor constructs to make IκBα/DNA conjugates for the fluorescence-force experiments (Figure 6.5A). Representative stretching and relaxing time traces of IκBα are shown in Figure 6.5B, obtained in the buffer containing 10mM Tris: HCl (pH 7.8), 150 mM NaCl, 0.5 % (wt/vol) D-glucose, 165 U/ml glucose oxidase, 2170 U/ml catalase, 3 mM Trolox, 0.5 mg/ml BSA and 0.1% (vol/vol) Tween 20. After averaging among many force cycles from several molecules, we plot the averaged FRET efficiency versus force curves for stretching and relaxing the single IκBα molecules (Figure 6.5C). FRET efficiency quickly decreases to zero at ~ 5 pN. After converting FRET to Cy3-Cy5 separation distance assuming $R_0 = 6$ nm, we replot distance versus force curves in Figure 6.5D. The averaged Cy3-Cy5 separation increases rapidly as a function of force for stretching. In the relaxing curve does not often coincide with the stretching curve. Surprisingly, for the relaxing curve, the Cy3-Cy5 distance recovered to a same value at a higher force (referred to as 'overshooting') compared to the stretching curve, which has never been observed from any mechanical unfolding experiment using single molecule force-based method. The energy cost to unfold the protein in the stretching circle cannot be smaller than the energy regained through the protein refolding in the relaxing circle. Considering that FRET can only monitor the Cy3-Cy5 separation distance up to ~10 nm, we were only able to monitor the initial stage of the protein unfolding. Therefore, it is possible that the stretching curve and relaxing curve could have a cross-over point at a force larger than 5 pN where FRET efficiency is zero and we are unable to detect it. Further investigation is needed to confirm this and a pure mechanical measurement seems promising to test the hypothesis. Because the weakly folded AR5 and AR6 of IκBα may be responsible for the 'overshooting' phenomenon, we performed fluorescence-force experiments for an IκBα mutant (E128C/S262C/Y254L /Y257A) where two more mutations were made at residues Y254 and Y257 to make AR5 and AR6 as stable as ARs 1-4 [214]. Figures 6.5E-G show the fluorescence-force time traces, averaged FRET-force curves, and Cy3-Cy5 distance versus force curves of the mutant. The stretching curve of the mutant is similar as that of IκBα but the 'overshooting' was abolished in the relaxing curve (Figures 6.5F and 6.5G). In the relaxing cycle, the molecule often recovered to a same Cy3-Cy5 distance value at lower force compared to the stretching cycle (Figure 6.5G), which is consistent with previous unfolding measurements for the anykrin repeats [215,216]. The 'overshooting' seems to be caused by the disordered AR5 and AR6 of IκBα. However, further investigation is clearly needed.

6.4 Figures

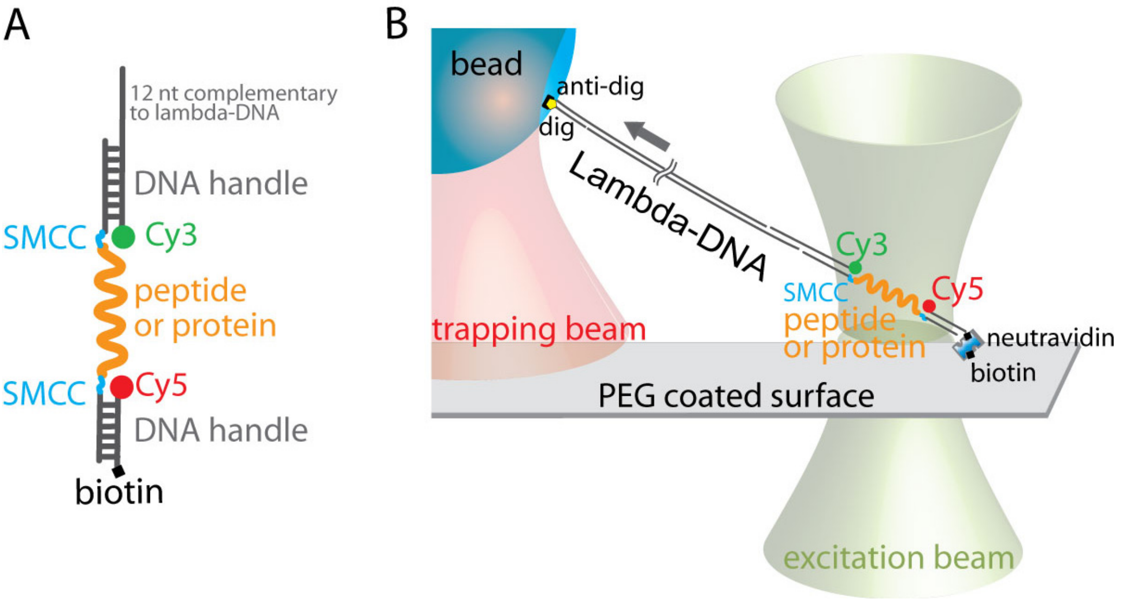

Figure 6.1 (A and B) Diagrams depicting how we extend our fluorescence-force spectroscopy to stretch single peptides or proteins.

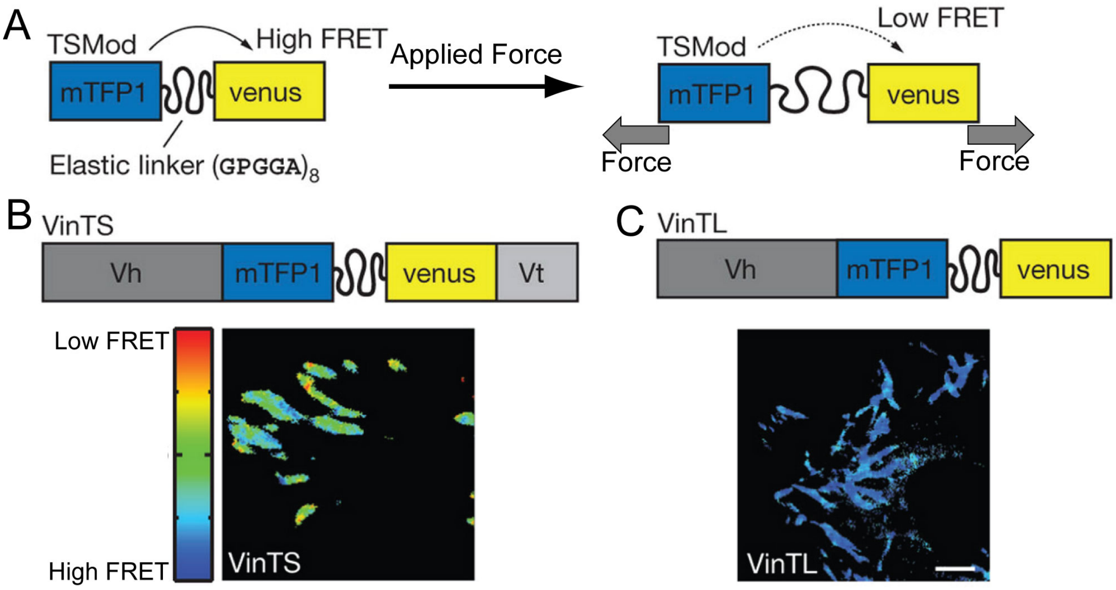

Figure 6.2 The figures are adopted from Ref. [101]. (A) The tension sensor module (TSMod) consists of two fluorophores separated by a flagelliform linker sequence $(GPGGA)_8$. At zero force, the elastic linker (i.e. the peptide) gives a relatively high FRET efficiency (left). When force across TSMod extends the elastic linker, FRET efficiency decreases (right). (B) A representative fluorescence lifetime image of cells expressing the vinculin tension sensor (VinTS) which consists of TSMod inserted after amino acid 883 of vinculin. The Color scale bar represents lifetimes of donor mTFP1, which can be converted into FRET values. Red represents low FRET and blue is high FRET. (C) A representative fluorescence lifetime image of cells expressing the tailless mutant of the vinculin tension sensor (VinTL). TSMod should not experience applied force without the ability to bind the actin cytoskeleton, giving mostly a blue color which indicates high FRET. Scale bar, 2 μm.

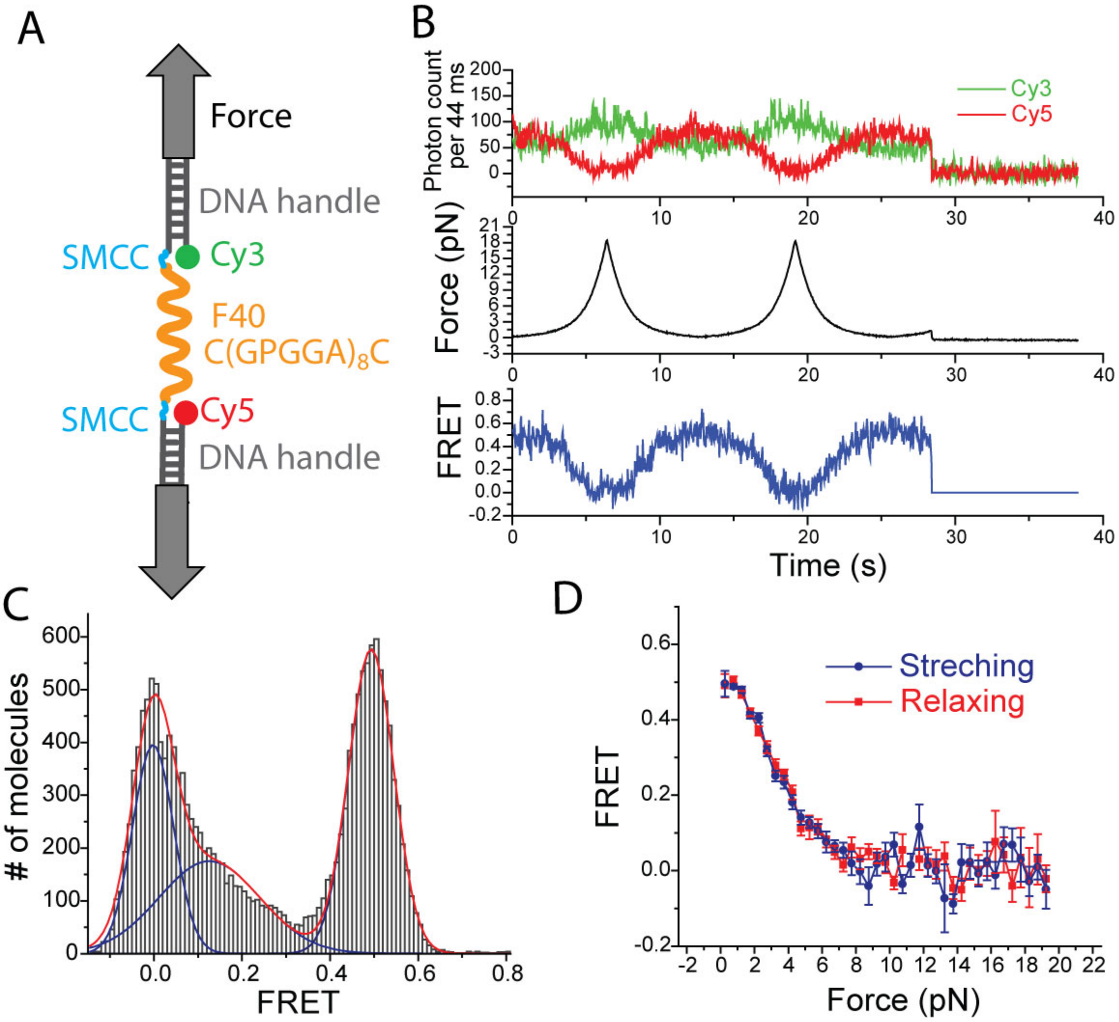

Figure 6.3 (A) A diagram that depicts F40. (B) Fluorescence-force time traces of peptide linker undergoing multiple stretching and relaxing cycles. FRET decreases as force increases and vice versa, as determined from anti-correlated Cy3 (green) and Cy5 (red) intensity. The tether broke at ~28 s. (C) Single-molecule FRET histogram of F40 at zero force. The peak at ~0.5 FRET represents F40. (D) Averaged FRET versus force curves of several molecules reveals little hysteresis upon stretching and relaxing. The force bin size for averaging is 0.3 pN. Error bars represent s.e.m.

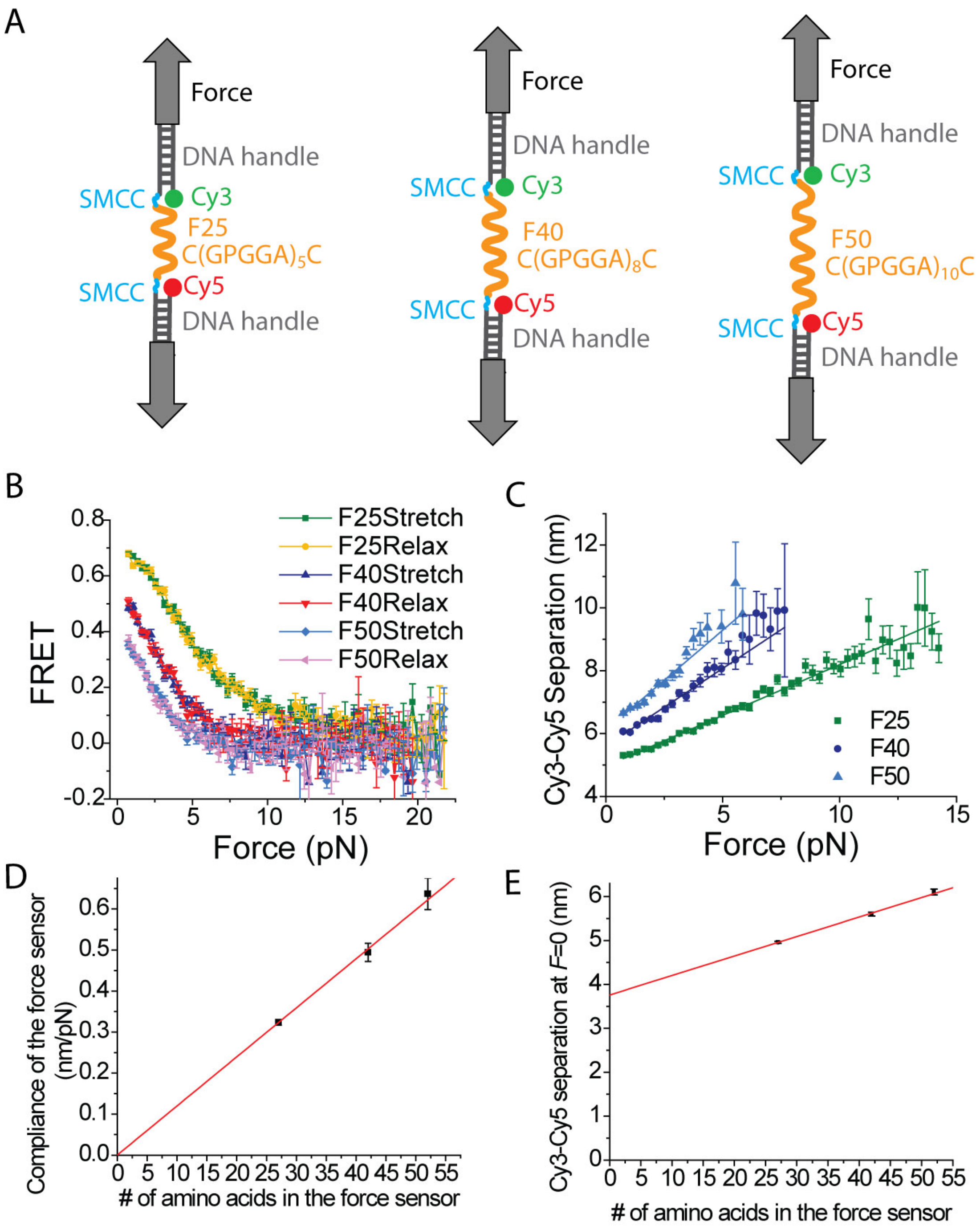

Figure 6.4 (A) Diagrams that depict F25, F40 and F50. (B) Averaged FRET versus force curves of several molecules from many stretching and relaxing cycles when the maximum force achieved was set to ~ 20 pN. The force bin size for averaging is 0.3 pN. (C) The separation distance between Cy3 and Cy5 as a function of applied force. Solid lines are the fit to straight lines. Error bars shown in (B) and (C) represent s.e.m. (D)

Compliance of the force sensor versus the number of amino acides in the force sensor. Red line is the linear fit. (E) The calculated Cy3-Cy5 distance at zero force versus the number of amino acides in the force sensor. Error bars shown in (D) and (E) represent the fitting standard errors obtained from the linear fits in (C).

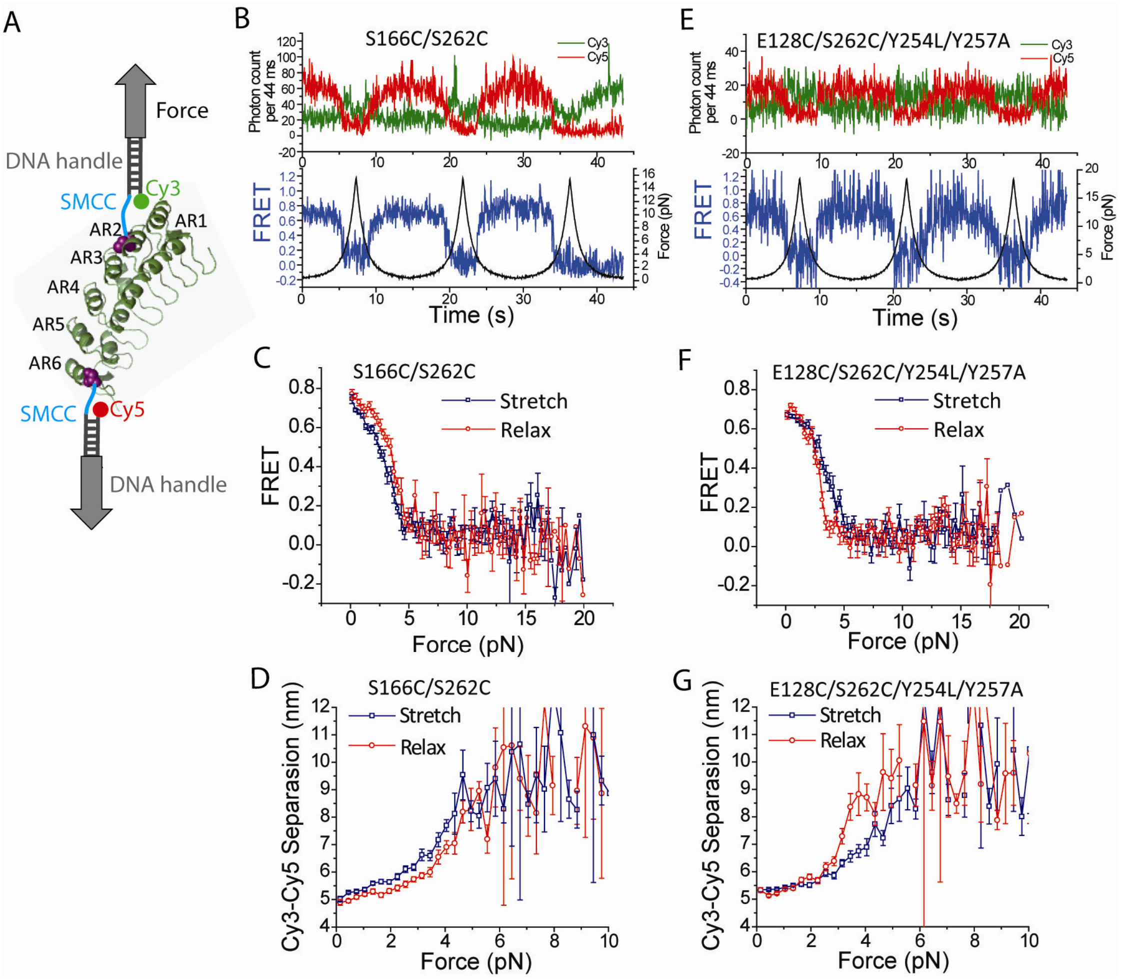

Figure 6.5 (A) A diagram that shows the experimental scheme to stretch IκBα. The purple spheres represent the two cysteine residues where the DNA handles are linked to. (B-D) Fluorescence-force time traces (B), averaged FRET-force curves (C) and Cy3-Cy5 separationi distance vs. force curves (D) of a single IκBα protein (two cysteine mutations S166C/S262C were made for the DNA handle linkage and all wild-type cysteines were replaced with serines) for several stretching and relaxing cycles. AR5 and AR6 are weakly folded in this mutant. (E-G) Fluorescence-force time traces (E), averaged FRET-

force curves (F) and Cy3-Cy5 separationi distance vs. force curves (G) of a single IκBα mutant (E128C/S262C/Y254L/Y257A) for several stretching and relaxing cycles. Beside the two cysteine mutantions E128C/S262C for the DNA handle linkage and the replacement of wilde type cysteines, two more mutantions (Y254L/Y257A) were made to make AR5 and AR6 as stable as ARs 1-4. The force bin size for averaging is 0.3 pN. Error bars represent s.e.m.

Chapter 7
Detecting Intramolecular Conformational Dynamics in a FRET-Insensitive Distance Range[‡‡]

7.1 Introduction

In our fluorescence-force spectroscopy, FRET is the only measure of the conformational dynamics of the biomolecule or biological complex, so the detection range is limited by the FRET sensitive distance range (3-10 nm). As mentioned in Chapter 1, FRET efficiency, E_{FRET}, is a measure of how much energy is transferred from the donor to the acceptor and is given by $E_{FRET} = 1/(1+(R/R_o)^6)$, where R is the distance between the donor and the accepter and R_o is the Förster radius at which $E_{FRET} = 0.5$ [10]. A typical value of R_o is 5-7 nm for the FRET pairs used in a single molecule experiment [9], making smFRET sensitive to the distance changes in the range of 3-10 nm [6]. Nanoparticle-induced lifetime modification has been used to serve as a nanoscopic ruler for the distance range beyond the upper limit of FRET sensitive range (> 10 nm) [217]. There have been previous attempts to monitor small distance changes in the 0-3 nm distance range but they are mostly based on time-resolved or time-correlated fluorescence spectroscopy using freely diffusing biomolecules and hence could not yield long time traces of a single biomolecule undergoing conformational changes [218-224]. For some FRET pairs, when the donor and acceptor come in close proximity (< 3 nm), their interactions cause complex fluorescence fluctuations [225]. Protein induced fluorescence enhancement, a recently reported single molecule assay, provides a means of monitoring the time-dependent intermolecular distance change between a fluorophore and a protein in the 0-3 nm range [226]. However, an equivalent method is missing for detecting the intramolecular conformational dynamics of single biomolecules in the smFRET

[‡‡] This work has been published as a paper:
Zhou, R., Kunzelmann, S., Webb M.R. and Ha, T. "Detecting intramolecular conformational dynamics of single molecules in short distance range with sub-nanometer sensitivity", Nano Letters , DOI: 10.1021/nl2032876 (2011)

insensitive distance range.

Therefore, developing a fluorescence-based method complementary to FRET for the detection of small comformational dynamics potentially extend our fluorescence-force spectroscopy to analyze more biological systems in which the intramolecular conformational changes are minimal. In addition, this complementary tool can be also used in the absence of the optical tweezers for characterizing nano-devices, nano-sensors and biological macromolecules at the single molecule level.

In this chapter, we use a ParM mutant, an engineered ADP-sensing protein [227], as a model system to illustrate the use of self-quenching between two identical tetramethylrhodamines (TMR) to study the intramolecular conformational dynamics in short distances. When in close proximity, the two TMRs can stack on each other to form a dimer in which their fluorescence emission is significantly quenched. Self-quenching of TMR due to stacking has been used in the ensemble studies to monitor the peptide cleavage by proteases [228,229], and intramolecular conformational changes of proteins [227,230,231] and nucleic acids [232]. This strategy has also been used to study molecular motors stepping on microtubules at both ensemble and single molecule levels [233,234]. In the previous attempts to utilize this approach to study titin unfolding/refolding at a single protein level, there were multiple TMRs attached to a titin molecule and rapid fluorescent enhancement induced by chemical denaturants was shown to be the result of direct action of the denaturants on TMR dimers rather than protein unfolding [235,236]. In this article, we present a generalizable surface-tethered single molecule assay for detecting conformational changes of individual biomolecules in a FRET inaccessible short range and in real time.

7.2 Experimental Results

7.2.1 Assay Design and Validation

The model system we use to demonstrate our assay is ParM, a bacterial actin homologue that forms F-actin-like filaments during plasmid segregation in *E. coli* [237]. ParM consists of two domains (I and II) between which is a cleft where the nucleotide binding site is located. ParM is in an open conformation in the absence of ADP whereas it changes to a closed conformation with ADP bound by closing the two domains (Figure

7.1A). The mutations T174A/T175N and K33A were made to increase the selectivity for ADP versus ATP and to inhibit filament formation, respectively [227]. To use TMR self-quenching as a reporter for the dynamics between the open and closed conformations, two cysteines residues were introduced (D63C/D224C; Figure 7.1A) which reacted with 5′-isomers of tetramethylrhodamine iodoacetamide (5-TMRIA) on either side of the nucleotide binding cleft (the natural, exposed cysteine in the wild-type protein was mutated to alanine, C287A). The two attachment positions (or cysteines) in the protein must be sufficiently close (~1.5 nm) and the cysteine side chains needs to adopt appropriate relative orientations for the two TMRs to dimerize in one of the ParM conformations but not in the other. In order to satisfy these requirements, several pairs of TMR labeling positions were tested through a screening process [227,230]. In general, such screening procedure would be needed to identify the optimum labeling positions even if structural information is available for a protein. In the previous ensemble measurement, the ParM mutant (His_6/K33A /D63C/T174A/T175N/D224C/C287A) developed as a ADP sensor showed ~ 15-fold fluorescence increase and the characteristic absorbance changes of the rhodamines in response to ADP binding [227], suggesting that distance change, estimated from the crystal structures, from 1.6 nm (ADP unbound, open conformation) to 2.1 nm (ADP bound, closed conformation) is enough to strongly affect the probability of rhodamines stacking.

We have developed multiple surface immobilization strategies for smFRET experiments where fluorescently labeled biomolecules are anchored onto a PEG (polyethylene glycol) coated surface with a low density such that individual molecules can be resolved as well-separated diffraction limited spots [9,238]. In our current design, ParM was surface-immobilized using an antibody against the $Histidine_6$-tag [238] to achieve specific binding and the total internal reflection fluorescence (TIRF) microscope [9] was used for sample illumination and data acquisition (Figure 7.1B). Upon ADP binding, one would expect the doubly TMR-labeled ParM to change from a fluorescently quenched to an unquenched state. The oxygen-scavenging system with Trolox was used for imaging to reduce photobleaching while preventing milliseconds time scale photophysical blinking of TMRs (Figure 7.2)[239].

We first validated the assay by comparing the TIRF images, obtained in the absence and presence of His_6-tagged ParM at different ADP concentrations (Figure 7.3A). Before adding ParM to the sample chamber containing a penta-His-antibody coated surface, the surface image showed ~30 fluorescent spots per imaging area (2,700 μm^2) presumably due to surface impurities. After anchoring the proteins to the surface and flushing away excess unbound proteins, we observed ~100 fluorescent spots on average per imaging area in the absence of ADP (Figure 7.3B). The additional ~70 spots observed beyond the surface impurity spots (~30) typically show a steady, continuous fluorescence emission over time with one photobleaching step (Figure 7.3B), which we assign to the proteins with only one active TMR attached. Either the protein is singly labeled or one of the two TMRs has been photobleached before data acquisition, but in either case TMR self-quenching would not occur. We then sequentially injected imaging buffers containing increasing ADP concentrations and determined the average number of fluorescent spots per imaging area, N. N increases with increasing ADP concentrations to a saturation value of ~290 (Figures 7.3C and 7.3D). This indicates a larger fraction of proteins is bound with ADP at high ADP concentrations because ADP binding converts ParM from a weakly-fluorescent (or quenched) state into a highly-fluorescent (or unquenched) state and the proteins in the quenched state cannot be detected by the automated algorithm to pick fluorescent spots. The hyperbolic fit to the data points yields a dissociation constant (K_d) of 20 ± 3 μM for ADP binding to the protein (Figure 2d), similar to the value of 30 ± 4 μM obtained from previous ensemble experiments [227]. In order to demonstrate that ParM proteins were immobilized on the surface through specific interactions rather than non-specific adsorption, we used a surface without penta-His-antibody coating and obtained ~ 40 fluorescent spots per imaging area in the presence of ADP, which is close to the ~ 30 spots of surface impurities (Figures 7.3A and 7.3C).

7.2.2 Detection of Protein Conformational Transitions

In the presence of ADP, two types of fluorescence-intensity versus time traces were observed: Type I molecules (around 100 per imaging area at all ADP concentrations tested) displayed steady (or continuous) fluorescence intensity over time until photobleaching (Figure 7.3B); Type II molecules (the number per imaging area increased from ~50 to ~200 as ADP concentration increased from 2 to 400 μM) display two-state transitions between a weakly-fluorescent state (nearly non-fluorescence) and a highly-fluorescent state. Figure 7.4A shows the representative intensity-time traces of Type II molecules with corresponding fluorescence intensity distributions at five different ADP concentrations. The weakly fluorescent state is not completely non-fluorescent (Figure 7.5) and the fluorescence emission in the highly-fluorescent state is 20 ± 5 (mean ± s.d) times larger than that in the weakly-fluorescent state, similar to the 15-fold difference between the unquenched and quenched states determined from ensemble measurements [227]. The dwell time of the weakly-fluorescent state (Δt_{off}) and the dwell time of the highly-fluorescent state (Δt_{on}) were collected from many Type II molecules. The histograms of Δt_{on} and Δt_{off} fit well with single exponential functions (Figure 7.4B). The transition rates between the two states at different ADP concentrations are plotted in Figure 7.6A. Here, $k_{\text{on}}=1/\tau_{\text{off}}$ and $k_{\text{off}}=1/\tau_{\text{on}}$, where τ_{on} and τ_{off} are the average dwell times obtained from the single exponential fits. k_{off} is independent of ADP concentration whereas k_{on} displays a linear dependence on ADP concentration. These data suggest that the two-state dynamics observed in the Type II molecules represent events of single ADP binding to and dissociation from a single ParM protein carrying two active TMRs, with the unquenched state being the ADP-bound state and the quenched state being the ADP-unbound state. Therefore, ADP dissociation rate is equal to k_{off}, which is 2.9 ± 0.04 s^{-1} (mean ± s.e.m.) and the bimolecular association rate between ADP and ParM is 0.082 ± 0.002 s^{-1} μM^{-1} (mean ± s.e.m.), yielding a dissociation constant $K_{\text{d}} = 35 \pm 1$ μM (mean ± s.e.m.). These values are all consistent with the values obtained previously by stopped-flow experiments [227].

To examine the heterogeneity further among different ParM molecules, we plotted the distribution of transition rates for each molecule obtained at five different ADP concentrations (Figure 7.6B). The scatter plot indicates that the rates of ParM conformational changes are heterogeneous among different molecules even with the same ADP concentration. The intermolecular heterogeneity has been ubiquitously observed in single-molecule studies for the conformational kinetics and enzymatic activity of biomolecules, possibly due to local environment differences, sampling of conformational sub-states or small imperfections during the protein synthesis [240-242].

7.2.3 Characterization of the Photobleaching of TMR Dimers

As mentioned above, a fraction of molecules (Type I) emitted steady/continuous fluorescence over time both in the absence and presence of ADP (Figure 7.3B). A large fraction of molecules initially showing two-state dynamics (Type II) switched to Type I behavior (Figure 7.7A). In contrast, none of the molecules initially showing Type I behavior switched to Type II behavior. The mechanism of TMR self-quenching is not well-understood, but we speculate that the self-quenching of TMR requires that both TMR monomers are not photobleached so that once one of the two TMRs is photobleached the remaining TMR emits steadily. The fluorescence intensity histogram for a molecule that changed from Type II to Type I behavior showed three peaks (Figure 7.7B). The peak at near zero fluorescence intensity (I_L) represents the molecule in the quenched state, whereas the peak at the high fluorescence intensity (I_H) represents the unquenched state. The peak at the middle fluorescence intensity (I_M) represents the fluorescence emission when the molecule switches into the 'steady' fluorescence state. After a dynamic molecule switches into the I_M state, only one more photobleaching event was observed (Figure 7.7A), indicating that only one active TMR is present in the I_M state whereas there are two active TMRs present in its initial dynamic phase. From many similar time traces, we collected I_H and I_M values from Gaussian fits of the intensity histograms and calculated the ratio I_M/I_H for each molecule. The distribution of the ratio I_M/I_H obtained from all molecules showed two Gaussian peaks centered at 0.35 and 0.61, indicating two different I_M levels (Figure 7.7C). We notice that the sum of the two peak values is ~1. Given the fact that the fluorescence level of a single TMR varies with environment (on D63C or D224C positions; data not shown), each of the two different intermediate fluorescence levels could represent the protein population containing either of the two active TMRs. The peak at I_M/I_H=0.61 has a larger population probably because the TMR at one position can be photobleached faster than the other despite the lower emission rate.

Finally, we asked whether TMR photobleaching occurs significantly also from the stacked state or occurs only when the TMR molecules are unstacked. We further analyzed the intensity time traces of the molecules that show conversion from a dynamic to a steady phase and determined the state immediately before the conversion event. We found the molecule could be either in quenched (I_L) or unquenched (I_H) state before the conversion to the I_M state at all the five ADP concentrations tested. Figure 7.7D shows that the percentage of the molecules observed to switch from I_H to I_M increases as the ADP concentration increases, whereas the percentage of the molecules that show I_L to I_M transition decreases. However, if we consider the average dwell time of the ADP bound and unbound states and normalize each percentage value by the fraction of time spent in the two states (see also Section 7.4 *Experimental Procedures*), we found that the normalized probabilities for I_L to I_M and I_H to I_M transitions are both essentially independent of ADP concentration (0.32 ± 0.03 and 0.68 ± 0.03 respectively). This suggests that the probability for the TMR photobleaching to occur in the quenched, stacked state is half that for the TMR photobleaching to occur in the unquenched, unstacked state. We find this observation peculiar because one would normally imagine that in the stacked state, non-radiative decay to the ground state would occur much faster and the likelihood of photobleaching per photo-excitation would greatly decrease.

The dissociation constant of free TMR dimers (5′-isomers) in aqueous solutions is very high, ~137 μM [243] and indirect evidence indicates that TMR stacking itself does not greatly affect the affinity for the ligand, ADP or P_i [227,230]. Overall, it is reasonable to assume that TMR stacking and unstacking rates do not limit the ParM conformational changes induced by ADP binding and dissociation, and are likely to occur on a much faster time scale than ADP binding and dissociation. There is likely to be a small but significant amount, for example 5%, of unstacked TMRs in rapid equilibrium with stacked TMRs in the apo (or weakly-fluoresent) state that could be responsible for the low fluorescence rather than the non-fluorescence. In addition, it is also possible that fluorescence quenching by stacking is not complete because of conformational constraints exerted on the TMRs by tethering them to the protein surface. Even the ADP bound, unquenched state may represent a rapid equilibrium between the stacked and unstacked states favoring the unstacked state.

7.3 Conclusions

In conclusion, we demonstrated a surface-tethered single molecule assay to study the intramolecular conformational dynamics of biomolecules in short distance range (1-3 nm) based on self-quenching of two TMRs. We have shown that a sub-nanometer distance change (between 1.6 and 2.1 nm) between the two TMRs attachment points on a ADP sensing protein caused by the protein conformational dynamics can be sensitively detected by ~20-fold fluorescence intensity change. This single molecule assay is applicable to the studies of small conformational dynamics of other nano-devices based on biomolecules at short distances as long as rhodamines are positioned correctly, through a screening process, to take advantage of the structural changes [230]. Our method based on fluorescence quenching of two stacked rhodamine should be able to extend the single molecule analysis of biomolecules and other nano-scale machineries to the FRET-insensitive distance range, opening up many new opportunities. In addition, our work provides new insights about photophysics of rhodamine dimers that could not have been obtained otherwise: (1) photobleaching of either of the two rhodamines eliminates quenching of the other rhodamine fluorophore and (2) photobleaching from the highly quenched, stacked state is only two-fold slower than from the unstacked state.

7. 4 Experimental Procedures

Sample Preparation

Flow chambers were prepared on mPEG-coated quartz slides doped with biotin-PEG as described [9,11]. 0.2 mg/ml neutravidin (Thermo) was incubated for 5 min to generate neutravidin-coated flow chambers and the unbound excess neutravidin molecules were flushed away. 10 nM of biotinylated penta-His antibody (Qiagen) was then incubated for 10 min on the neutrAvidin-coated surface followed by flushing away the unbound excess antibodies as previously described [238] (this step was omitted for the control experiment where we showed ParM proteins were indeed immobilized on surface through specific interactions). 1 nM of ParM was incubated for 5 min and the imaging buffer containing 30 mM Tris-HCl (pH 7.5), 25 mM KCl, 3 mM $MgCl_2$, 4 mM Trolox, 0.1 mg/ml BSA with an oxygen scavenging system (1 mg/ml glucose oxidase, 0.4% (w/v) D-glucose and 0.04 mg/ml catalase) was injected into the flow chamber for single-molecule data acquisition. The measurements were performed at room temperature (22 ± 1°C). ParM, labeled with rhodamines, at stock concentration of 322 μM was obtained and stored using standard buffer (30 mM Tris-HCl, 1 mM DTT, 150 mM KCl, 1 mM EDTA) as previously described [227] and diluted into 1 nM concentration right before each experiment.

Single-Molecule Data Acquisition

The prism type total internal reflection fluorescence microscopy (TIRF) [9,11] was used to acquire all the single-molecule data. Briefly, a Nd:YAG laser with 532 nm wavelength was guided through the prism to generate an evanescent field of illumination. A water-immersion objective (60×, numerical aperture 1.2, Olympus) was used to collect the signal and the scattered light was removed using a 550 nm long-pass filter. Although the laser was set up specifically for Cy3-Cy5 FRET experiment, this set up can be used for rhodamine, which has a similar spectroscopic profile to Cy3 fluorophore. The fluorescence signal was sent to a high-speed CCD camera (iXon DV 887-BI, Andor Technology). Time resolution of 0.03 sec was used for data acquisition.

Data Analysis

The florescent spots were determined using a custom DSL program described before [238]. The average number of the fluorescent spots per imaging area (2,700 μm^2) was calculated from 20 or more TIRF images taken from different regions. For the two-state fluorescence dynamics, the dwell times in each state were estimated from intensity-time traces (having at least ten turnovers; 50–100 sec long) using a custom MATLAB (Mathworks) routines using a thresholding criterion described before [244]. Dwell time histograms were built from 50-100 molecules at each ADP concentration and fitted to single exponential functions to obtain the average dwell times (τ_{on} and τ_{off}). Rate constants were estimated as the inverse of the average dwell times.

To obtain the normalized probabilities in Figure 7.7D, we consider the average life time of the state immediately before the molecule converts from a dynamic to a static phase (τ_{on} if the state was I_{H}, τ_{off} if the state was I_{L}. We define the percentage of the molecules that show I_{L} to I_{M} transition is x_i and the percentage of the molecules that show I_{H} to I_{M} transition is y_i at the ADP concentration of i (i = 2, 4, 10, 20, 40 µM; $x_i+y_i=1$). The normalized probability for the molecules that show I_{L} to I_{M} transition is given by $x_i' = \frac{x_i^f/\tau_{\mathrm{off}}}{x_i^f/\tau_{\mathrm{off}} + y_i^f/\tau_{\mathrm{on}}}$ and the normalized probability for the molecules that show I_{H} to I_{M} transition is given by $y_i' = \frac{y_i^f/\tau_{\mathrm{on}}}{x_i^f/\tau_{\mathrm{off}} + y_i^f/\tau_{\mathrm{on}}}$, where $x_i'+ y_i'=1$.

7.5 Figures

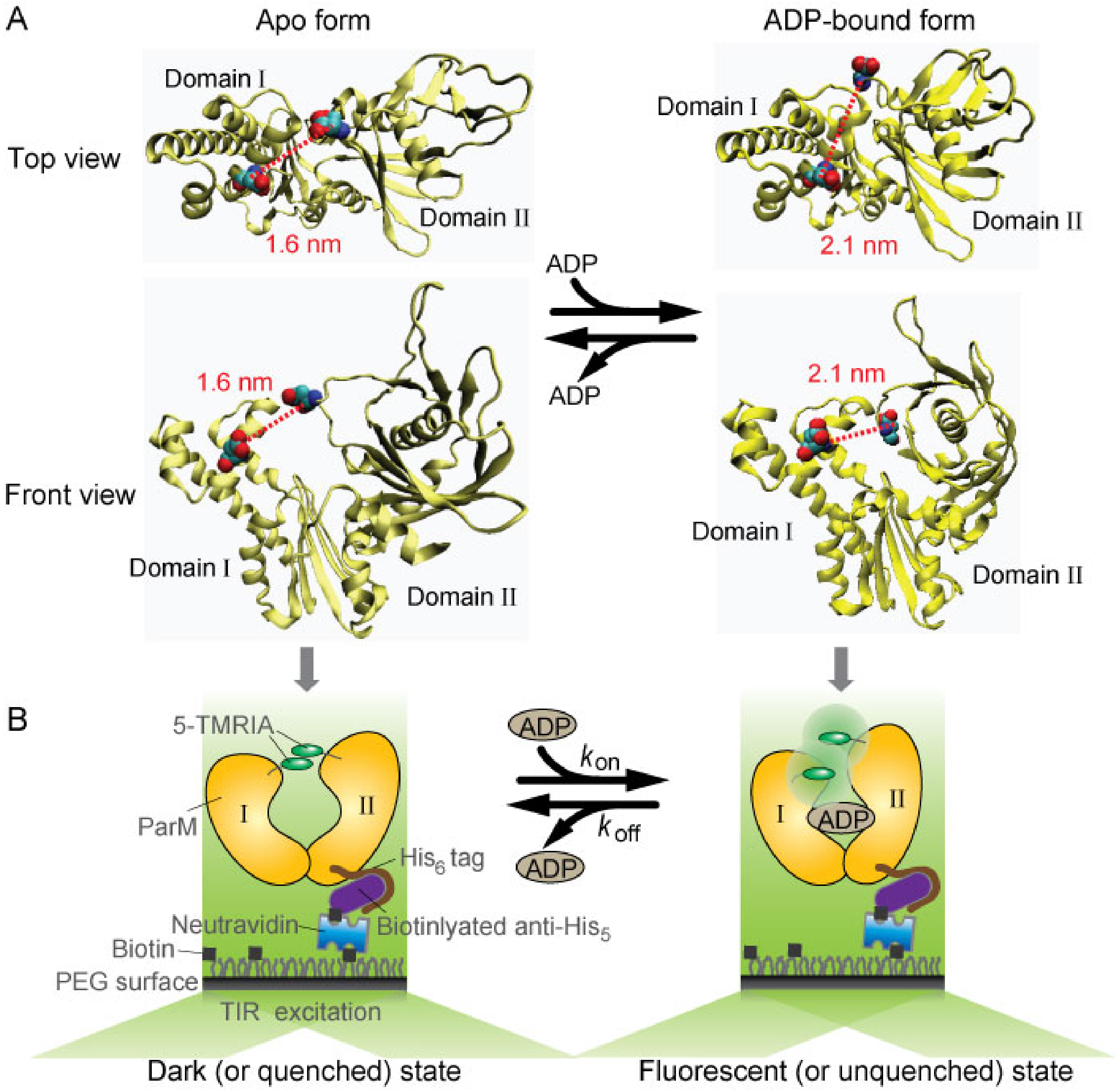

Figure 7.1 (A) The top and front views of ParM apo structure (left, PDB entry 1MWM) and the ADP-bound ParM structure (right, PDB entry 1MWK). The positions of the two cysteine mutations and the distance between them are shown (1.6 nm for the quenched state and 2.1 nm for the unquenched state; the distances were measured between cysteine α-carbons). (B) The experimental scheme that shows how the protein is anchored onto the PEG-coated surface through anti-His_5/His_6-tag and biotin/neutravidin interactions (also see Section 7.4 *Experimental Procedure*).

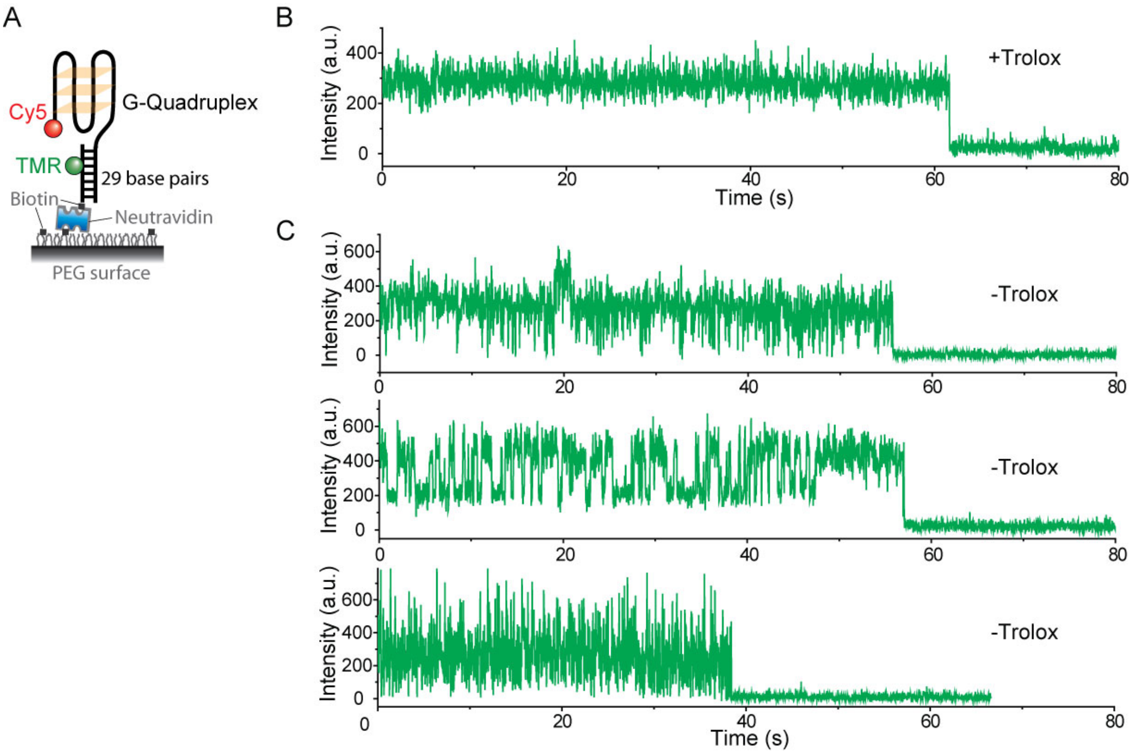

Figure 7.2 A TMR-labeled DNA construct previously used for G-Quadruplex study [245,246] was used to test whether oxygen removal and trolox addition in the imaging buffer sufficiently suppress the blinking of TMRs and increase the photostability of TMRs. (A) The experimental scheme. The TMR-labeled DNA molecules were immobilized on PEG surface via biotin-nertravidin interactions. The sample preparation is as described previously and the same single molecule TIR setup was used for the data acquisition as we used for the ParM experiments [245,246]. The Cy5 fluorophore on the DNA constructs was photobleached before data acquisition by directly exciting Cy5 using a 633 nm laser for the surface-immobilized DNA constructs. (B) A representative fluorescence-intensity time trace of a single TMR-labeled DNA molecule that shows one-step photobleaching in the buffer that we used for the ParM experiments (30 mM Tris-HCl (pH 7.5), 25 mM KCl, 3 mM $MgCl_2$, 4 mM Trolox, 0.1 mg/ml BSA, 1 mg/ml glucose oxidase, 0.4% (w/v) D-glucose, 0.04 mg/ml catalase) . (C) Representative fluorescence-intensity time traces of a single TMR-labeled DNA molecule that show one-step photobleaching in the buffer without trolox addition (30 mM Tris-HCl (pH 7.5), 25 mM KCl, 3 mM $MgCl_2$, 0.1 mg/ml BSA, 1 mg/ml glucose oxidase, 0.4% (w/v) D-glucose, 0.04 mg/ml catalase). Our data suggest the addition of trolox indeed suppressed the blinking of TMRs and hence

increased the photostability of TMRs. This result is similar as what we observed for Cyanine dyes [239].

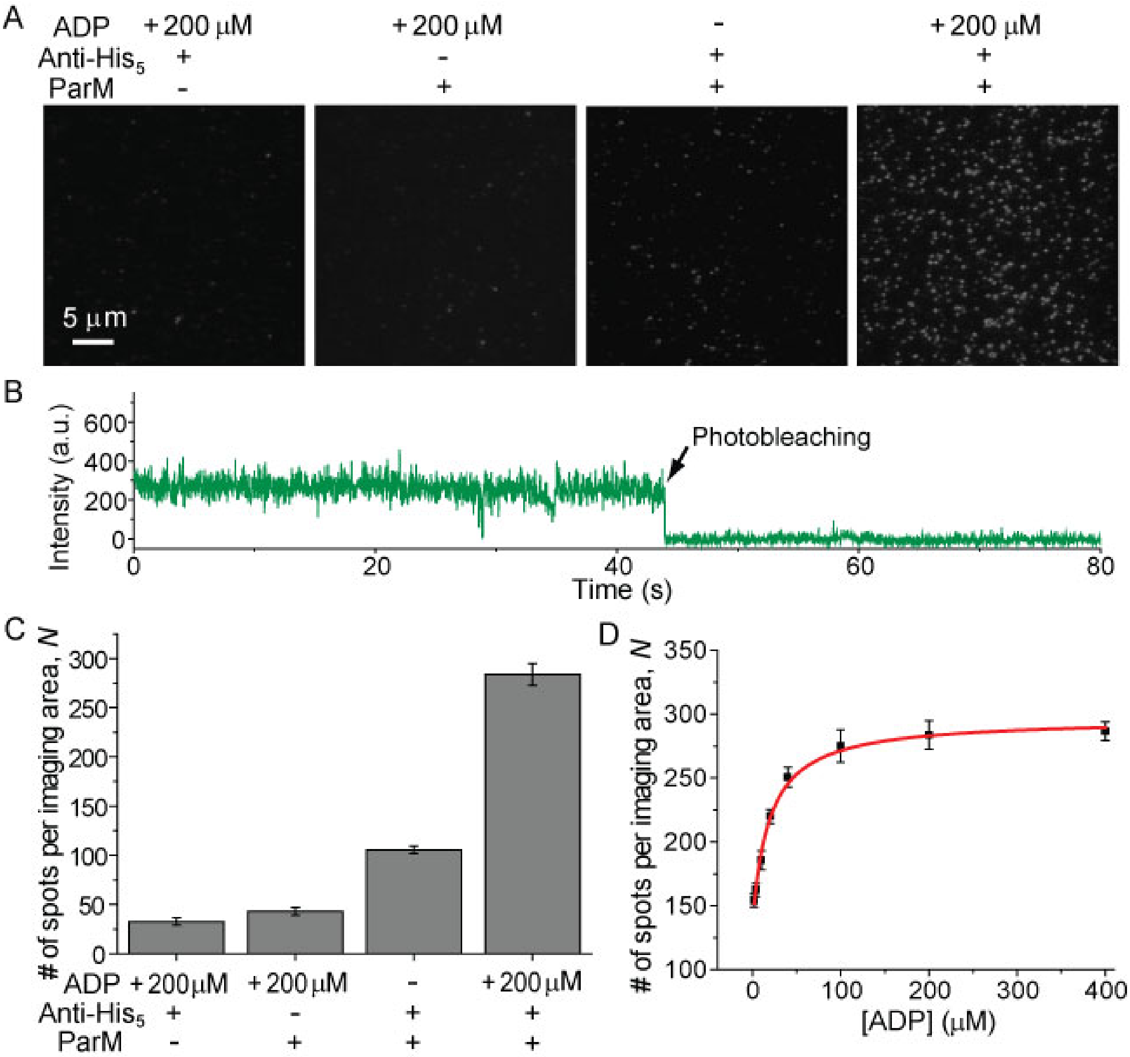

Figure 7.3 (A) Representative TIRF images taken in the absence and presence of ParM with the indicated ADP concentrations and surface conditions (penta-His-antibody coated surface or not). (B) A representative fluorescence-intensity time trace for the molecules in the absence of ADP, showing steady and continuous fluorescence over time. (C) The average number of fluorescent spots per imaging area determined in the absence and presence of ParM and/or ADP. (D) The average number of fluorescence spots per imaging area as a function of the ADP concentration. The red line is the fit to a hyperbola.

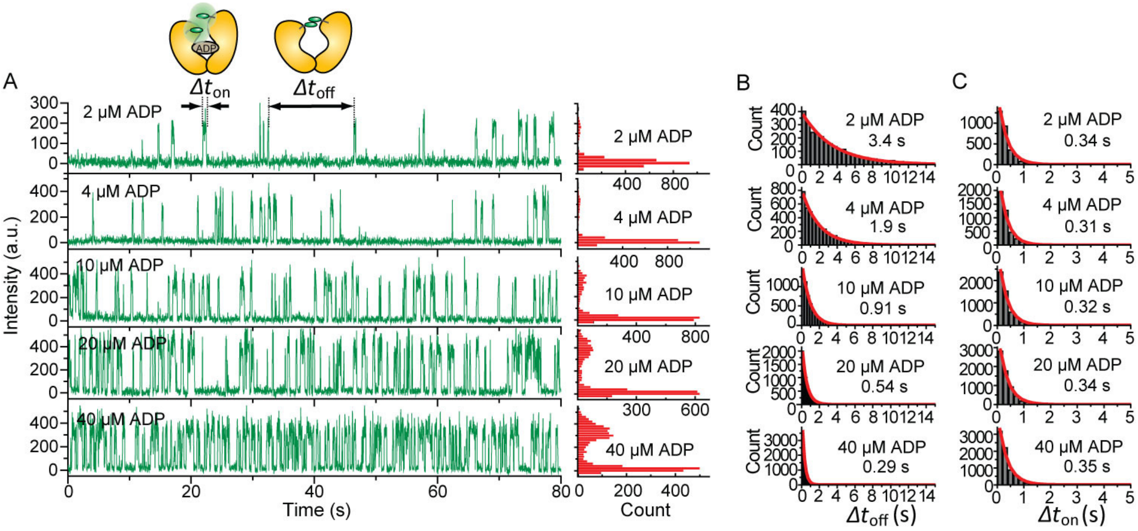

Figure 7.4 (A) Representative fluorescence-intensity time traces for the molecules showing two-state dynamics at five different ADP concentrations with the corresponding fluorescence intensity distributions. (B and C) Dwell time analysis for the two states respectively at the five ADP concentrations. The dwell time histograms were built from 50-100 molecules at each ADP concentration. The red lines are the single exponential fits to the dwell time histograms. τ_{on} or τ_{off} obtained from the fit is shown next to each histogram.

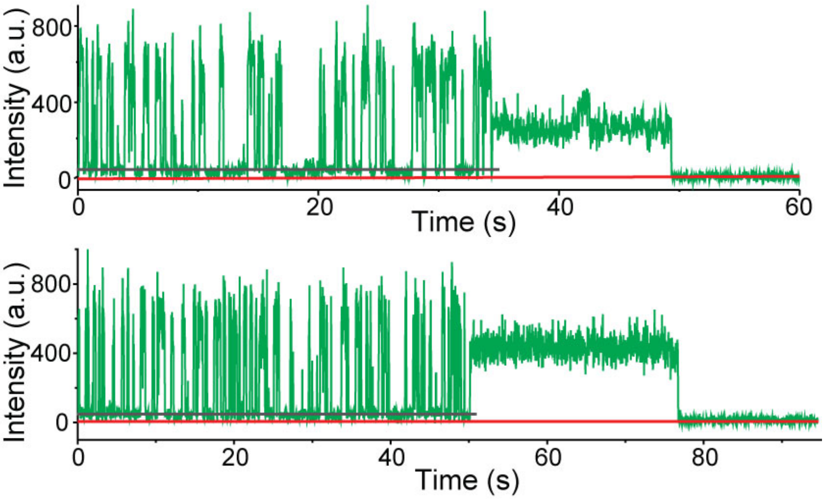

Figure 7.5 Representative fluorescence-intensity time traces of a single ParM-based ADP sensor obtained at 20 μM ADP. After one of the two TMRs on the protein is photobleached, the fluorescence emission of the protein goes into an intermediate fluorescence level. Later after the second TMR is photobleached, the fluorescence

emission goes down to a background value which has been corrected to zero. The red solid line shows the zero background value. The average fluorescence emission in the quenched (or apo) state (gray solid lines) typically shows a non-zero value (above the red line).

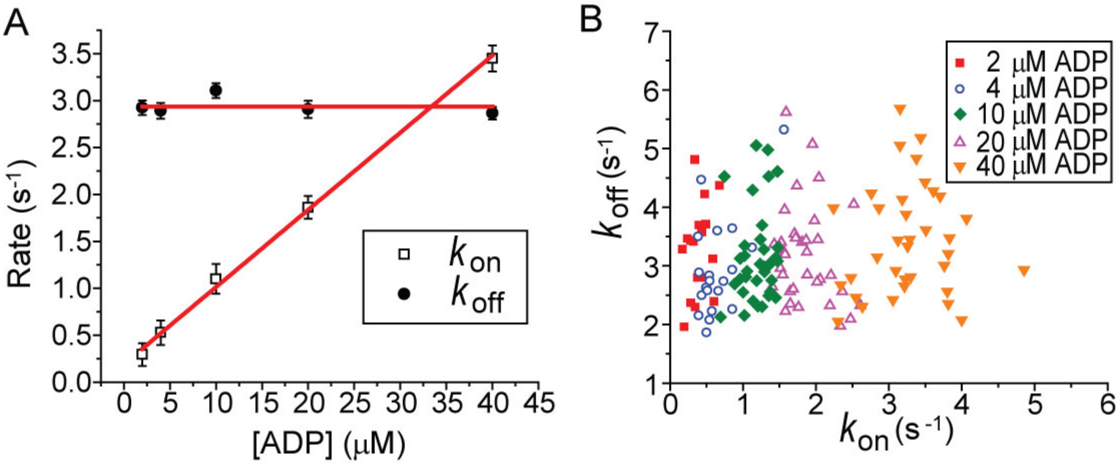

Figure 7.6 (A) The transition rates between the quenched and unquenched states at five ADP concentrations. The best fit horizontal was performed for k_{off} and the best linear fit was performed for k_{on}. (B) Scatter plots of the transition rates among many different individual molecules at five ADP concentrations.

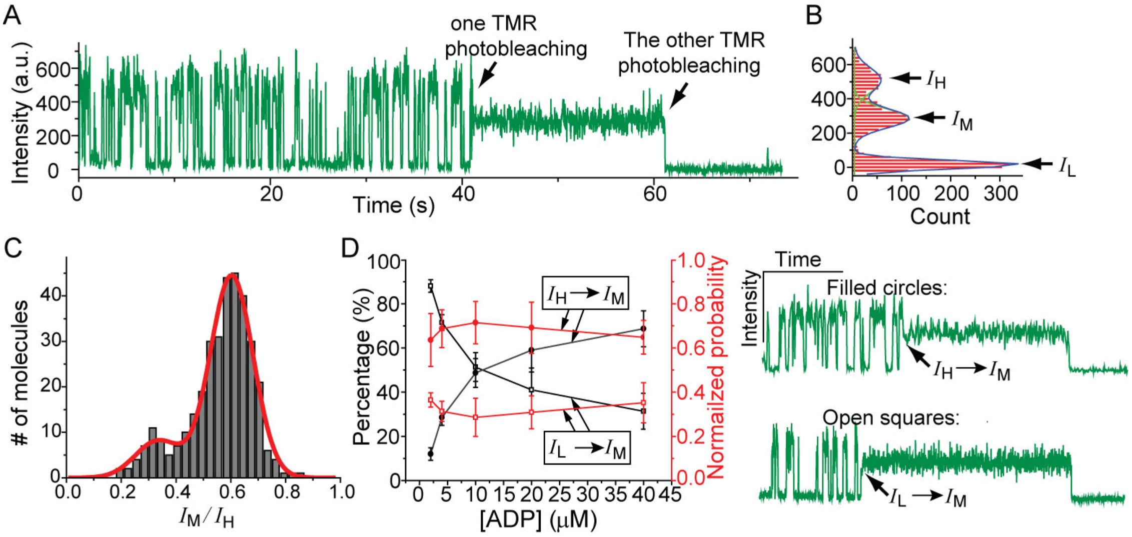

Figure 7.7 (A and B) A representative fluorescence-intensity time trace for the molecules showing conversion from two-state dynamics to steady fluorescence and the corresponding fluorescence intensity distribution (This trace was taken at 20 μM ADP). (C) Distribution of the ratio I_M/I_H built from 343 molecules that show the type of time trace in a). The red line is the fit to the sum of two Gaussian peaks. (D) The percentages of the molecules that convert from the unquenched to the I_M state or from the quenched to the I_M state when the molecule switches from a dynamic to a steady phase at five ADP concentrations, with calculated probabilities normalized to the average dwell time of the state before the conversion. The example conversion traces (from I_H to I_M, from I_L to I_M) are shown in the right.

Appendix A
Stretching a Mobile HJ Bound by a HJ Resolvase

A.1 Introduction

In Chapter 5, we use fluorescence-force spectroscopy to stretch DNA Holliday junctions (HJs) where the designed HJ constructs are all immobile. In fact, if the opposing arms of a HJ contain homologous sequences in the junction core region, the branch point of a HJ may migrate spontaneously through a process called branch migration. In the cell, brach migration is catalyzed by enzymes (such as helicases). At a later time point, the HJ needs to be cleaved to two nicked DNA double strands. There is a class of proteins called Holliday junction resolvase to selectively bind to HJs and accomplish the cleavage. In bacteriophage T7, T7 endonuclease I (endo I) is the encoded HJ resolvase and is a stable dimmer of identical 149 amino acids subunits [247]. Endo I preferentially binds to HJs with high affinity and cleaves the two continuous DNA strands adjacent to the crossover point in the presence of Mg^{2+} ions [248]. The crystal structures of endo I alone or in complex with a synthetic four-way DNA junction (Figure A.1) have been resolved [247,249,250] . Upon endo I binding to the HJ, the structure of the junction is distorted and is different from the structure of *iso*I (or *iso*II) (Figure A1). There are also two possible binding directions for endo I which correspond to the two possible cleavage products [251] (Figure A.2). Each endo I monomer has one active site which contains two ion binding sites (Sites 1 and 2). The active site for the cleavage activity contains three acidic side chains (Glu20, Asp55 and Glu65) and a lysine (Lys67), very similar to that of many type II restriction enzymes such as *Bgl*I (Figure A.1D; the scissile phosphate bond shown by the black arrow). The metal ion at site 1 is coordinated by Asp 55, Glu 65 and Thr 66, whereas the metal ion at site 2 is coordinated by Asp 55 [249,250]. The hydrolytic water molecule was thought to be coordinated by the ion at site 1 to carry out in-line nucleophilic attack on the scissile phosphate. The negatively charged transition state is stabilized by the ion at site 2 and Lys67. Glu20 may have a more general electrostatic role. Although T7 endo I is a structure-specific enzyme, the catalytic domain of T7 Endo I is a non-specific nicking endonuclease and shows no sequence preference [252].

A.2 Stretching the Naked Mobile HJ

The spontaneous branch migration of Holliday junction (HJ) with 1 bp step size has been reported previously [253]. We took the same mobile HJ construct (Figure A.3A; refered to as mmHJ). The mobile HJ is capable of branch migration with 5 bp of identical sequence (the pink region in Fig.9a) in the opposite arms so that six spontaneous migration steps are expected and the distance between Cy3 and Cy5 may range from 10 to 20 bp during the migration. The force applied through the two opposing arms of the HJ can bias the spontaneous migration, which has implications on how much of helicase-catalyzed branch migration could be attributable to spontaneous branch migration. We applied five sequential stretching cycles. The FRET efficiency decreased from ~ 0.35 to 0.1 as increasing force in absence of divalent ions (2 mM EDTA; Figure A.3B). In the presence of divalent ions, FRET efficiency started with a higher initial value (~0.45; this difference comes from the structure difference between the open state and the stacking conformer of HJs) and decreased (Figures A.3B and A.3C). The stretching curves at high Mg^{2+} displayed more fluctuations because it is known that increasing divalent ions can slow down the spontaneous branch migration [175,253] whereas in the absence of Mg^{2+} the dynamics were too fast to be observed in our given time resolution (~ 44 ms). We found a relatively high force (> 15 pN in the absence of Mg^{2+}, > 20 pN in te presence of Mg^{2+}) is required to completely bias the spontaneous migration which means the helicases need to actively apply high enough force to prevent the migration from going backwards. This is consistent with previous work where a 23 pN stall force was found to halt RuvAB-directed branch migration [254].

A.3 Stretching the Mobile HJ bound by T7 Endo I

We next tested the T7 endonuclease I binding to the mobile HJ construct described above (Figure A.4; inserted cartoon shows the stretching direction). To prevent the cleavage, we used a catalytically impaired mutant of the protein (K67A). In the presence of 10 mM

Ca^{2+} or Mg^{2+}, FRET fluctuations induced by spontaneous branch migration was previously observed for the mobile HJ construct we used (mmHJ) [253]. We found such fast FRET fluctuations induced by spontaneous branch migration were completely stopped upon the binding of endo I to HJ, indicating that endo I binding halts the spontaneous branch migration (Figure A.4). Then we asked the question if the force-induced branch migration can occur even after endo I binds to the HJ. We observed that FRET efficiency decreased as the force increased at 10 mM Mg^{2+} (Scenario 1; Figure A.5A). The initial FRET values from different molecules are different, suggesting endo I can bind at different branch points which can migrate within 5 bp freely before the protein binds. We think the force-induced FRET decrease is not due to branch migration but represents the force-induced deformation of the HJ or protein because the FRET always jumped back to a same initial value once the force was released in Scenario 1. To confirm this, we tested an immobile HJ (termed imHJ) which contains no any identical sequence in the opposite arms. Indeed, we observed the similar force-induced FRET decrease as shown in Scenario 1 for the mobile HJ in the same ionic condition (Figure A.5B). Endo I binding displayed strong divalent ion dependence and we may divide all the individual fluorescence-force time traces into three scenarios (Figure A.5A): (Scenario 1) the FRET time trace is very repetitive in each force cycle and there is no any abrupt FRET change within each force cycle. Although the initial FRET value in a force cycle for different molecules could be different, FRET jumped back to a same initial value once the force was released for the same molecule; (Scenario 2) in the time trace of a HJ molecule, once we released the force, FRET frequently jumped to a value which was different from that of the previous force cycle; (Scenario 3) The time trace of a HJ molecule shows many adrupt FRET changes even within each force cycle. The averaged FRET-force curves for different ionic conditions are shown in Figure A.5B, which show the ionic concentration dependence. The abrupt FRET changes are related to the stability of endo I binding to HJ and the binding stability increases as increasing Mg^{2+} or Ca^{2+} concentrations.

A.4 Figures

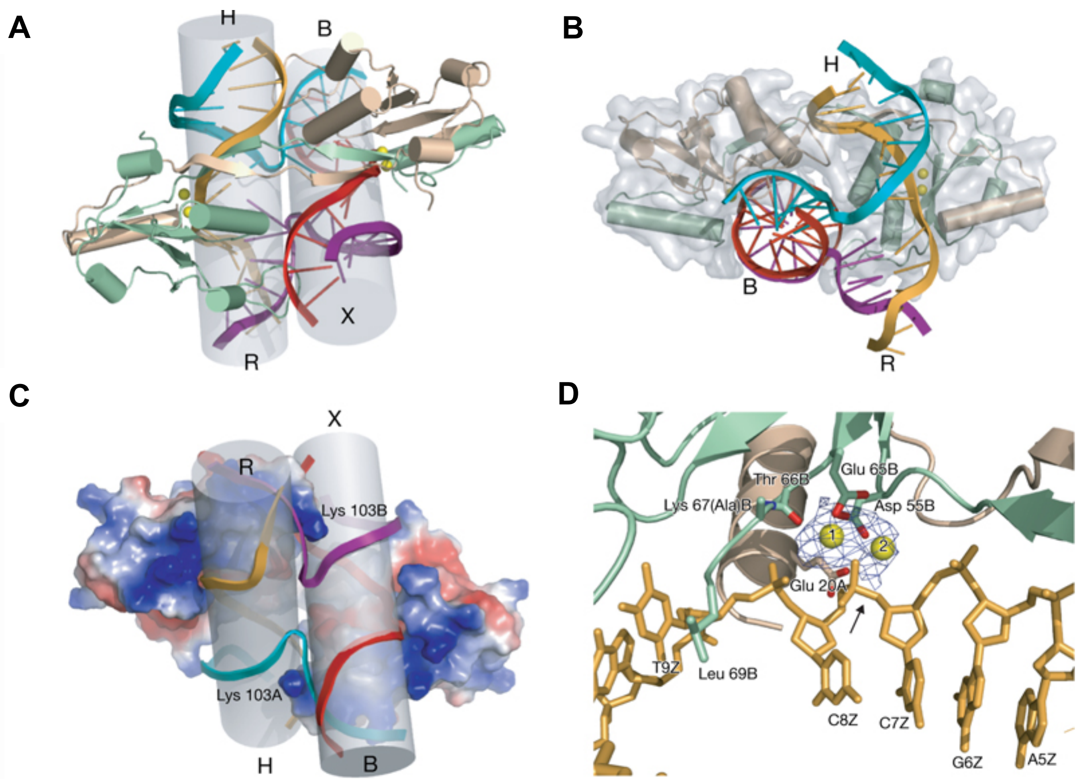

Figure A1 Crystal structure of the HJ resolvase phage T7 endonuclease I in complex with a synthetic four-way HJ and the active site of T7 endonulcease I (Adopted from Ref.[249]) .

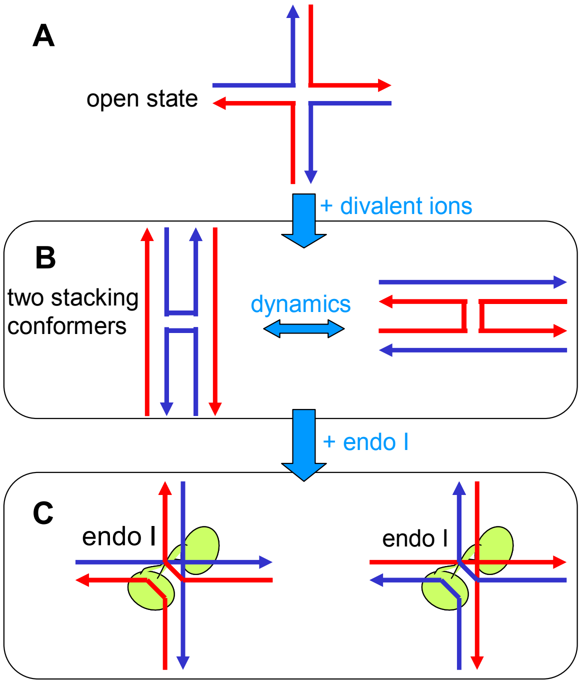

Figure A.2 Structure diagrams of a Holliday junction in the (A) absence and (B) presence of divalent ions. (C) Two possible binding directions of T7 endo I to the junctions.

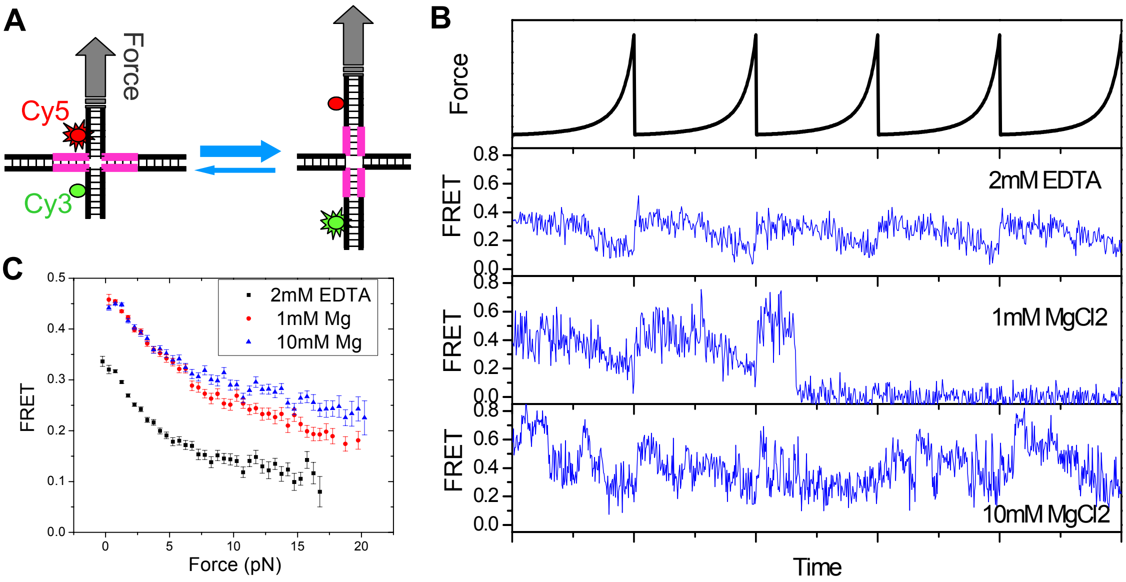

Figure A.3 Force-induced HJ branch migration. (A) Experimental Scheme. The force was applied to two opposite arms of the mobile HJ. (B) Force-fluoresence time traces for five stretching cycles at different Mg^{2+} concentrations. (C) Averaged FRET-force curves from several molecules and force cycles.

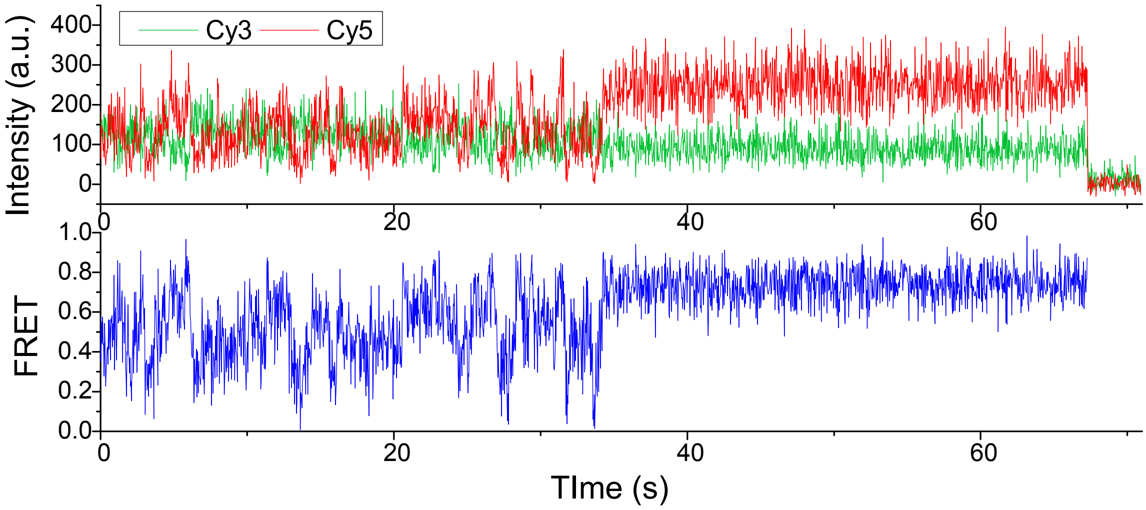

Figure A.4 Representative single molecule time traces of Cy3-Cy5 labeled mobile HJ upon the addition of 10 nM of T7 endo I at the time point of ~ 30 s. 10 mM Ca^{2+} were present both before and after the addition of the protein. Fast FRET fluctuation stops at about 33 s.

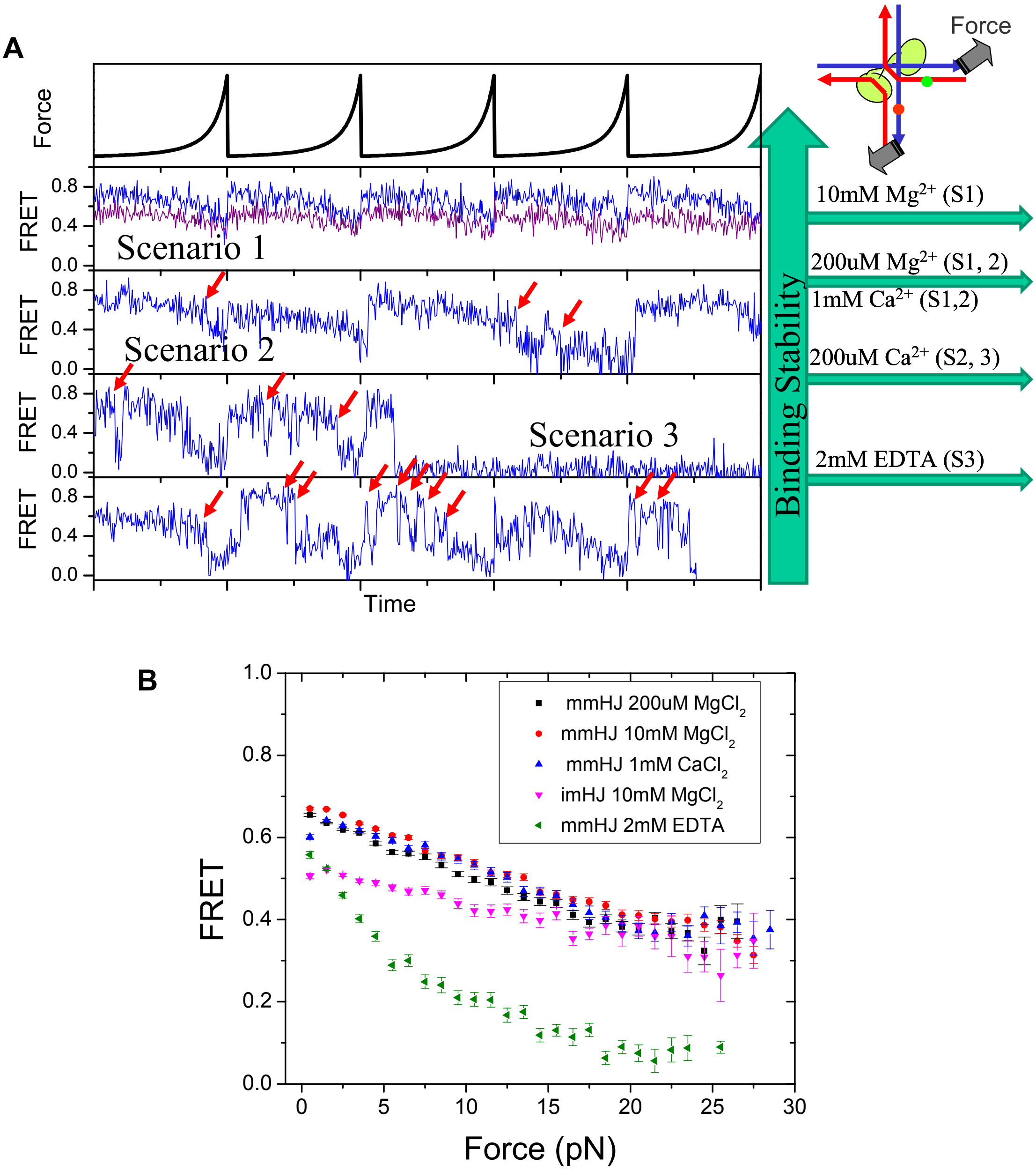

Figure A.5 (A) Representative fluorescence-force time traces in different ion conditions. The red arrows indicate abrupt FRET changes. (B) The averaged FERT-force curves for stretching the single mobile Holiday junction (mmHJ) bound by endo I (K67A) in different and the averaged FRET-force curve for stretching the single immobile Holliday junction (imHJ) bound by endo I (K67A) in the presence of 10 mM $MgCl_2$.

Appendix B
Probing the Orientation of Cyanine Fluorophores Terminally Attached to DNA

B.1 Experimental Design

It has been previously shown that the fluorophores, indocarbocyanine-3 (Cy3) or indocarbocyanine-5 (Cy5) terminally attached to the 5' terminus of the duplex DNA, are stacked onto the end of the DNA helix [255-257]. Here, we adopt a previously developed polarization modulation method [258] in combination with our fluorescence-force spectroscopy to test whether the Cy3 linked to 5'-end of a DNA duplex is indeed stably stacked. In the polarization modulation method [258], the polarization direction of a linearly polarized excitation laser beam was modulated (or rotated) in order to measure the projected dipole orientation in the *xy* plane of a single fluorophore linked to a short single-stranded DNA molecule, and the DNA-fluorophore complex was nonspecifically adsorbed to a silanized glass surface. In our fluorescence-force spectroscopy, a 22 base pair DNA duplex with Cy3 attached to the 5' end was specifically attached to surface through neutravidin-biotin interactions so that DNA duplex is free to rotate and tumble (Figure B.3A). The 22 bp DNA duplex construct was made by annealing two single strands 5'-<u>GGGCGGCGACCT</u>CCCACCGCTCGTGCTGCTACGG/iSp18/TTTTTTTTTT-/Biotin/-3' and 5'-/Cy3/CCG TAGCAGCACGAGCGGTGGG-3' (from IDT DNA Technologies), where the sequence underlined is the 12 nt cohesive end site of λ-DNA and /iSp18/ represents an internal spacer used to minimize the interaction between the PEG surface and the 22 bp duplex. In our setup, a combination of a polarizing beam splitter and a half wave plate is used to control the excitation laser power, and a second half wave plate is added into the beam path such that we can modulate the polarization direction of the excitation laser in the *xy* sample plane by rotating the second half wave plate manually. According to the dipole approximation, the intensity of the emission signal of the single fluorophore, *I*, has the following formula [258],

$$I \propto \left| \vec{\mu} \cdot \vec{E} \right|^2 \qquad \text{(B.1)}$$

where $\vec{\mu}$ is the molecular transition dipole and $\vec{E}$ is the excitation laser field. Therefore if single Cy3 fluorophore can be fixed in the *xy* plane and the excitation polarization angle (θ) is modulated graduatlly, the detected emission intensity of Cy3 is proportional to $(cos\theta)^2$.

However, even the Cy3 is indeed stacked to the 5' terminus of the DNA duplex, we cannot observe such modulations in the Cy3 emission intensity with the time resolution of our instrument by modulating the excitation polarization, because the DNA duplex itself, along with the dipole orientation of the Cy3, is free to rotate and tumble very fast on a smaller time scale at zero force. Therefore, using optical tweezers to apply a force to both ends of the DNA duplex is necessary to eliminate the tumbling of the duplex. With enough tension applied, we expect to see the Cy3 emission inetensity changes when modulating the excitation polarization direction if Cy3 is indeed stacked on the DNA terminus.

B.2 Experimental Results

The experimental scheme is shown in Figure B.1A. Once a surface-tethered bead was trapped, the coverslip surface was moved back and forth with the piezo-stage to roughly determine the tethered position by finding the central position of the stretching curves in two orthogonal directions in the *xy* plane. The origin of the piezo stage was then reset to this central position which is where the Cy3-labeled DNA is located. Next, the coverslip surface was moved along *x*-axis to three different positions (displaced by 10, 14 and 16.5 μm from the stage origin, corresponding to applied forces of ~ 0, 0.9 and 15 pN respectively). At each stage displacement, the Cy3 signal from the stretched DNA molecule was recorded by the APD for 10 seconds while the polarization direction of the 532 nm excitation laser was modulated by rotating the second half wave plate. At zero force, Cy3 emission did not change as the function of time. However, at 0.9 and 15 pN, the periodic intensity change of Cy3 emission was observed (Figure B.3B), indicating that Cy3 is indeed stacked on the terminus of the duplex DNA.

Next, we designed another similar experiment using fluorescence-force spectroscopy where we rotated the the dipole orientation of Cy3 about *z*-axis by rotating the optical trap rather than rotating the polarization direction of the excitation laser (Figure B.2A). After the origin of the piezo stage was reset the central position of the x and y stretching curves as described above, the optical trap was moved along *x*-axis by ~ 16 μm (corresponding to ~ 5 pN). We then started recorded Cy3 signal from the tethered molecule and at a later time point we started rotating the optical trap with a constant speed. A representative time trace recorded is shown in Figure B.2B. After some time point, the Cy3 signal begins to fluctuate periodically similar to the time traces we obtained in Figure B.1B. We can fit the time trace with a cosine square function,

$$I(t) = I_0 + A \cdot \cos^2\left(\pi \frac{t - t_0}{w}\right) \qquad \text{(B.2)}$$

We obtained w=5.06 ± 0.03 s from the fit (red line; Figure B.2B).

These results indicate that the Cy3 fluorophore attached to the 5' terminus of DNA is indeed stacked such that the orientation of the transition dipole moment is largely restricted.

B.3 Figures

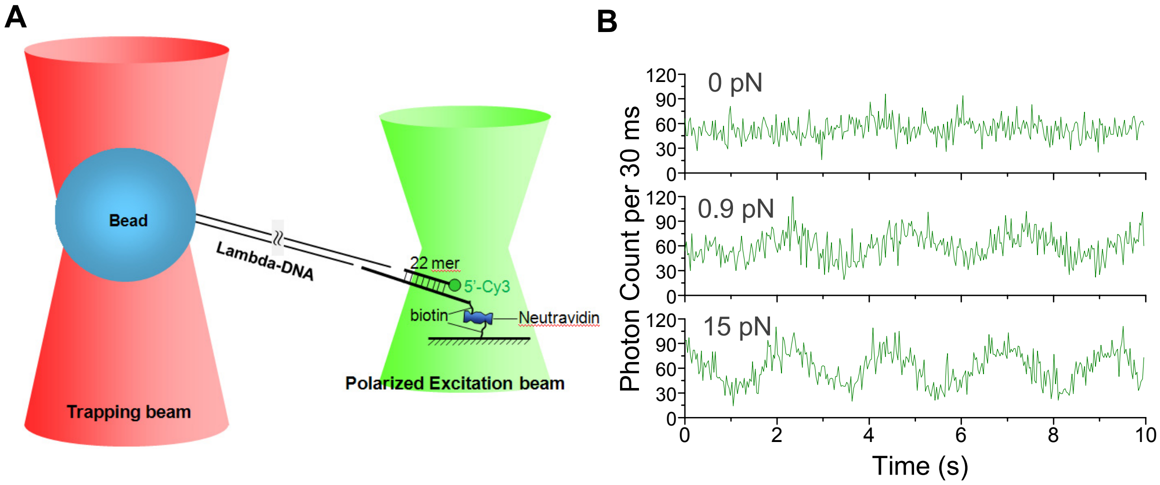

Figure B.1 (A) Experimental scheme. The polarization direction of the excitation laser beam was rotated by rotating the half wavelength plate manually. (B) The Cy3 signal from a single Cy3 fluorophore that is attached to the DNA duplex as a function of time at the different forces applied to the DNA duplex.

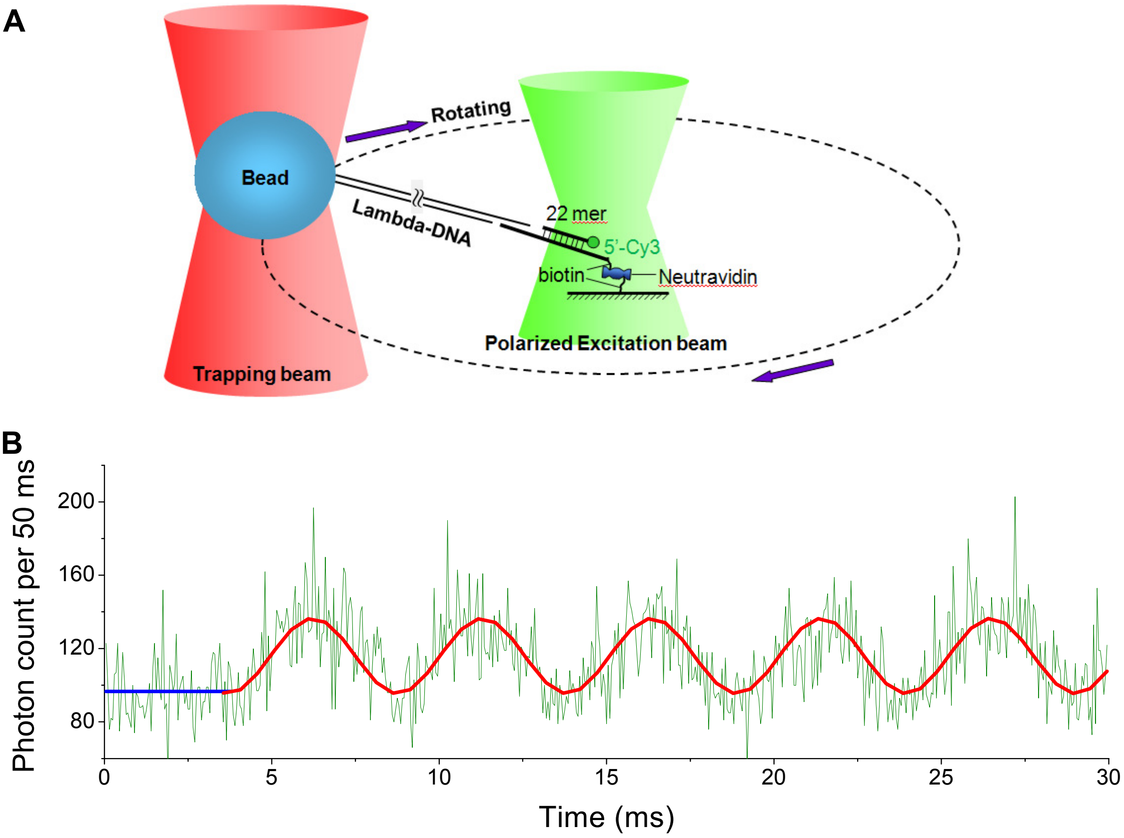

Figure B.2 (A) Experimental scheme. The polarization direction of the excitation laser beam was fixed whereas the optical trap was rotated by rotating the half wavelength plate manually. (B) The Cy3 signal from a single Cy3 fluorophore that is attached to the DNA duplex as a function of time (green trace). At time point $t = {\sim}3.8$ s, we started rotated the optical trap. The red trace is the fit to the cosine square function ($t > 3.8$ s).And the blue line indicates the mean value of the Cy3 signal before the optical trap started to rotate ($t < 3.8$ s).

References

1. Jablonski, A. Uber den Mechanismus der Photolumineszenz von Farbstoffphosphoren. *Zeitschrift fur Physik* **94**, 38-46 (1935).
2. Lakowicz, J. R. *Principles of Fluorescence Spectroscopy* (Kluwer Academic/Plenum Publishers, New York, 1999).
3. Forster, T. Experimental and Theoretical Investigation of the Intermolecular Transfer of Electronic Excitation Energy. *Zeitschrift Naturforsch A* **4**, 321-327 (1949).
4. Selvin, P. R. Lanthanide-based resonance energy transfer. *IEEE Journal of Selected Topics in Quantum Electronics: Lasers in Biology* **2**, 1077-1087 (1996).
5. Clegg, R. M. in *Methods in Enzymology* (eds. Lilley, D. M. J. & Dahlberg, J.) 353-388 (Academic Press, New York, 1992).
6. Ha, T. Single-molecule fluorescence methods for the study of nucleic acids. *Curr Opin Struct Biol* **11**, 287-92 (2001).
7. Ha, T. Single-molecule fluorescence resonance energy transfer. *Methods* **25**, 78-86 (2001).
8. Joo, C., Balci, H., Ishitsuka, Y., Buranachai, C. & Ha, T. Advances in single-molecule fluorescence methods for molecular biology. *Annu Rev Biochem* **77**, 51-76 (2008).
9. Roy, R., Hohng, S. & Ha, T. A practical guide to single-molecule FRET. *Nat Methods* **5**, 507-16 (2008).
10. Ha, T. et al. Probing the interaction between two single molecules: fluorescence resonance energy transfer between a single donor and a single acceptor. *Proc Natl Acad Sci U S A* **93**, 6264-8 (1996).
11. Joo, C. & Ha, T. in *Single molecule techniques: A laboratory manual* (eds. Selvin, P. R. & Ha, T.) 507 (Cold Spring Harbor Laboratory Press, New York, 2008).
12. Ha, T., Chemla, D. S., Enderle, T. & Weiss, S. Single molecule spectroscopy with automated positioning. *Applied Physics Letters* **70**, 782-784 (1997).
13. Ashkin, A., Dziedzic, J. M., Bjorkholm, J. E. & Chu, S. Observation of a Single-Beam Gradient Force Optical Trap for Dielectric Particles. *Optics Letters* **11**, 288-290 (1986).
14. Finer, J. T., Simmons, R. M. & Spudich, J. A. Single Myosin Molecule Mechanics - Piconewton Forces and Nanometer Steps. *Nature* **368**, 113-119 (1994).
15. Svoboda, K., Schmidt, C. F., Schnapp, B. J. & Block, S. M. Direct Observation of Kinesin Stepping by Optical Trapping Interferometry. *Nature* **365**, 721-727 (1993).
16. Visscher, K., Schnitzer, M. J. & Block, S. M. Single kinesin molecules studied with a molecular force clamp. *Nature* **400**, 184-189 (1999).
17. Kojima, H., Muto, E., Higuchi, H. & Yanagida, T. Mechanics of single kinesin molecules measured by optical trapping nanometry. *Biophysical Journal* **73**, 2012-2022 (1997).
18. Smith, S. B., Cui, Y. & Bustamante, C. Overstretching B-DNA: the elastic response of individual double-stranded and single-stranded DNA molecules. *Science* **271**, 795-9 (1996).

19. Woodside, M. T., Garcia-Garcia, C. & Block, S. M. Folding and unfolding single RNA molecules under tension. *Curr Opin Chem Biol* **12**, 640-6 (2008).

20. Woodside, M. T. et al. Nanomechanical measurements of the sequence-dependent folding landscapes of single nucleic acid hairpins. *Proc Natl Acad Sci U S A* **103**, 6190-5 (2006).

21. Smith, D. E. et al. The bacteriophage phi 29 portal motor can package DNA against a large internal force. *Nature* **413**, 748-752 (2001).

22. Fuller, D. N., Raymer, D. M., Kottadiel, V. I., Rao, V. B. & Smith, D. E. Single phage T4 DNA packaging motors exhibit large force generation, high velocity, and dynamic variability. *Proc Natl Acad Sci U S A* **104**, 16868-73 (2007).

23. Kellermayer, M. S., Smith, S. B., Granzier, H. L. & Bustamante, C. Folding-unfolding transitions in single titin molecules characterized with laser tweezers. *Science* **276**, 1112-6 (1997).

24. Tskhovrebova, L., Trinick, J., Sleep, J. A. & Simmons, R. M. Elasticity and unfolding of single molecules of the giant muscle protein titin. *Nature* **387**, 308-12 (1997).

25. Shank, E. A., Cecconi, C., Dill, J. W., Marqusee, S. & Bustamante, C. The folding cooperativity of a protein is controlled by its chain topology. *Nature* **465**, 637-U134 (2010).

26. Kim, J., Zhang, C. Z., Zhang, X. & Springer, T. A. A mechanically stabilized receptor-ligand flex-bond important in the vasculature. *Nature* **466**, 992-5.

27. Wang, M. D. et al. Force and velocity measured for single molecules of RNA polymerase. *Science* **282**, 902-907 (1998).

28. Wuite, G. J. L., Smith, S. B., Young, M., Keller, D. & Bustamante, C. Single-molecule studies of the effect of template tension on T7 DNA polymerase activity. *Nature* **404**, 103-106 (2000).

29. Pease, P. J. et al. Sequence-directed DNA translocation by purified FtsK. *Science* **307**, 586-590 (2005).

30. Greenleaf, W. J., Woodside, M. T. & Block, S. M. High-resolution, single-molecule measurements of biomolecular motion. *Annu Rev Biophys Biomol Struct* **36**, 171-90 (2007).

31. Bustamante, C., Macosko, J. C. & Wuite, G. J. Grabbing the cat by the tail: manipulating molecules one by one. *Nat Rev Mol Cell Biol* **1**, 130-6 (2000).

32. Moffitt, J. R., Chemla, Y. R., Smith, S. B. & Bustamante, C. Recent advances in optical tweezers. *Annu Rev Biochem* **77**, 205-28 (2008).

33. Abbondanzieri, E. A., Greenleaf, W. J., Shaevitz, J. W., Landick, R. & Block, S. M. Direct observation of base-pair stepping by RNA polymerase. *Nature* **438**, 460-465 (2005).

34. Moffitt, J. R., Chemla, Y. R., Izhaky, D. & Bustamante, C. Differential detection of dual traps improves the spatial resolution of optical tweezers. *Proceedings of the National Academy of Sciences of the United States of America* **103**, 9006-9011 (2006).

35. Carter, A. R., Seol, Y. & Perkins, T. T. Precision Surface-Coupled Optical-Trapping Assay with One-Basepair Resolution. *Biophysical Journal* **96**, 2926-2934 (2009).

36. Clausen-Schaumann, H., Seitz, M., Krautbauer, R. & Gaub, H. E. Force spectroscopy with single bio-molecules. *Curr Opin Chem Biol* **4**, 524-30 (2000).
37. Neuman, K. C., Lionnet, T. & Allemand, J. F. Single-molecule micromanipulation techniques. *Annual Review of Materials Research* **37**, 33-67 (2007).
38. Neuman, K. C. & Nagy, A. Single-molecule force spectroscopy: optical tweezers, magnetic tweezers and atomic force microscopy. *Nature Methods* **5**, 491-505 (2008).
39. Amit, R., Gileadi, O. & Stavans, J. Direct observation of RuvAB-catalyzed branch migration of single Holliday junctions. *Proceedings of the National Academy of Sciences of the United States of America* **101**, 11605-11610 (2004).
40. Lee, J.-B. et al. DNA primase acts as a molecular brake in DNA replication. *Nature* **439**, 621-624 (2006).
41. van Mameren, J. et al. Counting RAD51 proteins disassembling from nucleoprotein filaments under tension. *Nature* **457**, 745-748 (2009).
42. Grashoff, C. et al. Measuring mechanical tension across vinculin reveals regulation of focal adhesion dynamics. *Nature* **466**, 263-266 (2010).
43. Kamimura, S. & Takahashi, K. Direct Measurement of the Force of Microtubule Sliding in Flagella. *Nature* **293**, 566-568 (1981).
44. Kishino, A. & Yanagida, T. Force Measurements by Micromanipulation of a Single Actin Filament by Glass Needles. *Nature* **334**, 74-76 (1988).
45. Cluzel, P. et al. DNA: an extensible molecule. *Science* **271**, 792-4 (1996).
46. Zlatanova, J. & Leuba, S. H. Chromatin fibers, one-at-a-time. *Journal of Molecular Biology* **331**, 1-19 (2003).
47. Rief, M., Gautel, M., Oesterhelt, F., Fernandez, J. M. & Gaub, H. E. Reversible unfolding of individual titin immunoglobulin domains by AFM. *Science* **276**, 1109-1112 (1997).
48. Carrion-Vazquez, M. et al. Mechanical and chemical unfolding of a single protein: A comparison. *Proceedings of the National Academy of Sciences of the United States of America* **96**, 3694-3699 (1999).
49. Lee, G. U., Chrisey, L. A. & Colton, R. J. Direct Measurement of the Forces between Complementary Strands of DNA. *Science* **266**, 771-773 (1994).
50. Merkel, R., Nassoy, P., Leung, A., Ritchie, K. & Evans, E. Energy landscapes of receptor-ligand bonds explored with dynamic force spectroscopy. *Nature* **397**, 50-53 (1999).
51. Grandbois, M., Beyer, M., Rief, M., Clausen-Schaumann, H. & Gaub, H. E. How strong is a covalent bond? *Science* **283**, 1727-1730 (1999).
52. Lee, C. K., Wang, Y. M., Huang, L. S. & Lin, S. M. Atomic force microscopy: Determination of unbinding force, off rate and energy barrier for protein-ligand interaction. *Micron* **38**, 446-461 (2007).
53. Hinterdorfer, P. & Dufrene, Y. F. Detection and localization of single molecular recognition events using atomic force microscopy. *Nature Methods* **3**, 347-355 (2006).
54. Lee, G. U., Kidwell, D. A. & Colton, R. J. Sensing Discrete Streptavidin Biotin Interactions with Atomic-Force Microscopy. *Langmuir* **10**, 354-357 (1994).

55. Florin, E. L., Moy, V. T. & Gaub, H. E. Adhesion Forces between Individual Ligand-Receptor Pairs. *Science* **264**, 415-417 (1994).
56. Leckband, D. & Israelachvili, J. Intermolecular forces in biology. *Quarterly Reviews of Biophysics* **34**, 105-267 (2001).
57. Lim, C. T., Zhou, E. H., Li, A., Vedula, S. R. K. & Fu, H. X. Experimental techniques for single cell and single molecule biomechanics. *Materials Science & Engineering C-Biomimetic and Supramolecular Systems* **26**, 1278-1288 (2006).
58. Evans, E., Ritchie, K. & Merkel, R. Sensitive force technique to probe molecular adhesion and structural linkages at biological interfaces. *Biophys J* **68**, 2580-7 (1995).
59. Simson, D. A., Ziemann, F., Strigl, M. & Merkel, R. Micropipet-based pico force transducer: in depth analysis and experimental verification. *Biophys J* **74**, 2080-8 (1998).
60. Chesla, S. E., Selvaraj, P. & Zhu, C. Measuring two-dimensional receptor-ligand binding kinetics by micropipette. *Biophys J* **75**, 1553-72 (1998).
61. Smith, S. B., Finzi, L. & Bustamante, C. Direct Mechanical Measurements of the Elasticity of Single DNA-Molecules by Using Magnetic Beads. *Science* **258**, 1122-1126 (1992).
62. Yan, J. et al. Micromanipulation studies of chromatin fibers in Xenopus egg extracts reveal ATP-dependent chromatin assembly dynamics. *Molecular Biology of the Cell* **18**, 464-474 (2007).
63. Strick, T. R., Allemand, J. F., Bensimon, D., Bensimon, A. & Croquette, V. The elasticity of a single supercoiled DNA molecule. *Science* **271**, 1835-1837 (1996).
64. Koster, D. A., Crut, A., Shuman, S., Bjornsti, M. A. & Dekker, N. H. Cellular Strategies for Regulating DNA Supercoiling: A Single-Molecule Perspective. *Cell* **142**, 519-530 (2010).
65. Revyakin, A., Liu, C. Y., Ebright, R. H. & Strick, T. R. Abortive initiation and productive initiation by RNA polymerase involve DNA scrunching. *Science* **314**, 1139-1143 (2006).
66. Dessinges, M. N., Lionnet, T., Xi, X. G., Bensimon, D. & Croquette, V. Single-molecule assay reveals strand switching and enhanced processivity of UvrD. *Proceedings of the National Academy of Sciences of the United States of America* **101**, 6439-6444 (2004).
67. Lionnet, T., Spiering, M. M., Benkovic, S. J., Bensimon, D. & Croquette, V. Real-time observation of bacteriophage T4 gp41 helicase reveals an unwinding mechanism. *Proceedings of the National Academy of Sciences of the United States of America* **104**, 19790-19795 (2007).
68. Kim, S. J., Blainey, P. C., Schroeder, C. M. & Xie, X. S. Multiplexed single-molecule assay for enzymatic activity on flow-stretched DNA. *Nature Methods* **4**, 397-399 (2007).
69. van Oijen, A. M. et al. Single-Molecule Kinetics of Î» Exonuclease Reveal Base Dependence and Dynamic Disorder. *Science* **301**, 1235-1238 (2003).
70. Bustamante, C., Bryant, Z. & Smith, S. B. Ten years of tension: single-molecule DNA mechanics. *Nature* **421**, 423-7 (2003).
71. La Porta, A. & Wang, M. D. Optical torque wrench: angular trapping, rotation, and torque detection of quartz microparticles. *Phys Rev Lett* **92**, 190801 (2004).

72. EssevazRoulet, B., Bockelmann, U. & Heslot, F. Mechanical separation of the complementary strands of DNA. *Proceedings of the National Academy of Sciences of the United States of America* **94**, 11935-11940 (1997).
73. Rief, M., Clausen-Schaumann, H. & Gaub, H. E. Sequence-dependent mechanics of single DNA molecules. *Nature Structural Biology* **6**, 346-349 (1999).
74. Bustamante, C., Chemla, Y. R., Forde, N. R. & Izhaky, D. Mechanical processes in biochemistry. *Annu Rev Biochem* **73**, 705-48 (2004).
75. Li, P. T. X., Vieregg, J. & Tinoco, I. How RNA unfolds and refolds. *Annual Review of Biochemistry* **77**, 77-100 (2008).
76. Zhu, C., Bao, G. & Wang, N. Cell mechanics: Mechanical response, cell adhesion, and molecular deformation. *Annual Review of Biomedical Engineering* **2**, 189-226 (2000).
77. Borgia, A., Williams, P. M. & Clarke, J. Single-molecule studies of protein folding. *Annual Review of Biochemistry* **77**, 101-125 (2008).
78. Moy, V. T., Florin, E. L. & Gaub, H. E. Intermolecular Forces and Energies between Ligands and Receptors. *Science* **266**, 257-259 (1994).
79. Weisel, J. W., Shuman, H. & Litvinov, R. I. Protein-protein unbinding induced by force: single-molecule studies. *Curr Opin Struct Biol* **13**, 227-35 (2003).
80. Liu, W. et al. Single molecule mechanical probing of the SNARE protein interactions. *Biophys J* **91**, 744-58 (2006).
81. Yersin, A. et al. Interactions between synaptic vesicle fusion proteins explored by atomic force microscopy. *Proceedings of the National Academy of Sciences of the United States of America* **100**, 8736-8741 (2003).
82. Huang, J. et al. The kinetics of two-dimensional TCR and pMHC interactions determine T-cell responsiveness. *Nature* **464**, 932-6.
83. Evans, E. Probing the relation between force - Lifetime - and chemistry in single molecular bonds. *Annual Review of Biophysics and Biomolecular Structure* **30**, 105-128 (2001).
84. Liphardt, J., Dumont, S., Smith, S. B., Tinoco, I., Jr. & Bustamante, C. Equilibrium information from nonequilibrium measurements in an experimental test of Jarzynski's equality. *Science* **296**, 1832-5 (2002).
85. del Rio, A. et al. Stretching single talin rod molecules activates vinculin binding. *Science* **323**, 638-41 (2009).
86. Ishijima, A. et al. Multiple- and single-molecule analysis of the actomyosin motor by nanometer piconewton manipulation with a microneedle: Unitary steps and forces. *Biophysical Journal* **70**, 383-400 (1996).
87. Gennerich, A., Carter, A. P., Reck-Peterson, S. L. & Vale, R. D. Force-induced bidirectional stepping of cytoplasmic dynein. *Cell* **131**, 952-65 (2007).
88. Seidel, R. & Dekker, C. Single-molecule studies of nucleic acid motors. *Current Opinion in Structural Biology* **17**, 80-86 (2007).
89. Jiang, G. Y., Giannone, G., Critchley, D. R., Fukumoto, E. & Sheetz, M. P. Two-piconewton slip bond between fibronectin and the cytoskeleton depends on talin. *Nature* **424**, 334-337 (2003).
90. Balaban, N. Q. et al. Force and focal adhesion assembly: a close relationship studied using elastic micropatterned substrates. *Nature Cell Biology* **3**, 466-472 (2001).

91. Zlatanova, J., Lindsay, S. M. & Leuba, S. H. Single molecule force spectroscopy in biology using the atomic force microscope. *Progress in Biophysics and Molecular Biology* **74**, 37-61.
92. Moffitt, J. R., Chemla, Y. R., Izhaky, D. & Bustamante, C. Differential detection of dual traps improves the spatial resolution of optical tweezers. *Proc Natl Acad Sci U S A* **103**, 9006-11 (2006).
93. Dijk, M. A., Kapitein, L. C., Mameren, J., Schmidt, C. F. & Peterman, E. J. Combining optical trapping and single-molecule fluorescence spectroscopy: enhanced photobleaching of fluorophores. *J Phys Chem B* **108**, 6479-84 (2004).
94. Lang, M. J., Fordyce, P. M. & Block, S. M. Combined optical trapping and single-molecule fluorescence. *J Biol* **2**, 6 (2003).
95. Lang, M. J., Fordyce, P. M., Engh, A. M., Neuman, K. C. & Block, S. M. Simultaneous, coincident optical trapping and single-molecule fluorescence. *Nat Methods* **1**, 133-9 (2004).
96. Funatsu, T. et al. Imaging and nano-manipulation of single biomolecules. *Biophys Chem* **68**, 63-72 (1997).
97. Ishijima, A. et al. Simultaneous observation of individual ATPase and mechanical events by a single myosin molecule during interaction with actin. *Cell* **92**, 161-71 (1998).
98. Harada, Y. et al. Single molecule imaging and nanomanipulation of biomolecules. *Methods Cell Biol* **55**, 117-28 (1998).
99. Hohng, S. et al. Fluorescence-force spectroscopy maps two-dimensional reaction landscape of the holliday junction. *Science* **318**, 279-83 (2007).
100. Hohng, S. et al. Fluorescence-force spectroscopy maps two-dimensional reaction landscape of the holliday junction. *Science* **318**, 279-283 (2007).
101. Grashoff, C. et al. Measuring mechanical tension across vinculin reveals regulation of focal adhesion dynamics. *Nature* **466**, 263-U143 (2010).
102. Zhou, R. et al. SSB Functions as a Sliding Platform that Migrates on DNA via Reptation. *Cell* **146**, 222-232 (2011).
103. Neuman, K. C., Abbondanzieri, E. A. & Block, S. M. Measurement of the effective focal shift in an optical trap. *Optics Letters* **30**, 1318-1320 (2005).
104. Lang, M. J., Asbury, C. L., Shaevitz, J. W. & Block, S. M. An automated two-dimensional optical force clamp for single molecule studies. *Biophys J* **83**, 491-501 (2002).
105. Happel, J. & Brenner, H. *Low Reynolds number hydrodynamics: with special applications to particulate media* (Kluwer Academic Print on Demand, 1983).
106. Pralle, A., Florin, E. L., Stelzer, E. H. K. & Horber, J. K. H. Local viscosity probed by photonic force microscopy. *Applied Physics a-Materials Science & Processing* **66**, S71-S73 (1998).
107. Berg-Sørensen, K. & Flyvbjerg, H. Power spectrum analysis for optical tweezers. *Review of Scientific Instruments* **75**, 594 (2004).
108. Hohng, S., Joo, C. & Ha, T. Single-molecule three-color FRET. *Biophys J* **87**, 1328-37 (2004).
109. Bustamante, C., Marko, J. F., Siggia, E. D. & Smith, S. Entropic elasticity of lambda-phage DNA. *Science* **265**, 1599-600 (1994).

110. Selvin, P. R. & Ha, T. *Single Molecule Techniques: A Laboratory Manual* (Cold Spring Harbor Laboratory Press, 2007).
111. Myong, S., Rasnik, I., Joo, C., Lohman, T. M. & Ha, T. Repetitive shuttling of a motor protein on DNA. *Nature* **437**, 1321-5 (2005).
112. Yokota, H. et al. Single-molecule Visualization of Binding Modes of Helicase to DNA on PEGylated Surfaces. *Chemistry Letters* **38**, 308-309 (2009).
113. Richard, D. J. et al. Single-stranded DNA-binding protein hSSB1 is critical for genomic stability. *Nature* **453**, 677-81 (2008).
114. Kowalczykowski, S. C., Dixon, D. A., Eggleston, A. K., Lauder, S. D. & Rehrauer, W. M. Biochemistry of homologous recombination in Escherichia coli. *Microbiol Rev* **58**, 401-65 (1994).
115. Kuzminov, A. Recombinational repair of DNA damage in Escherichia coli and bacteriophage lambda. *Microbiol Mol Biol Rev* **63**, 751-813, table of contents (1999).
116. Meyer, R. R. & Laine, P. S. The single-stranded DNA-binding protein of Escherichia coli. *Microbiol Rev* **54**, 342-80 (1990).
117. Shereda, R. D., Kozlov, A. G., Lohman, T. M., Cox, M. M. & Keck, J. L. SSB as an organizer/mobilizer of genome maintenance complexes. *Crit Rev Biochem Mol Biol* **43**, 289-318 (2008).
118. Raghunathan, S., Kozlov, A. G., Lohman, T. M. & Waksman, G. Structure of the DNA binding domain of E. coli SSB bound to ssDNA. *Nat Struct Biol* **7**, 648-52 (2000).
119. Raghunathan, S., Ricard, C. S., Lohman, T. M. & Waksman, G. Crystal structure of the homo-tetrameric DNA binding domain of Escherichia coli single-stranded DNA-binding protein determined by multiwavelength x-ray diffraction on the selenomethionyl protein at 2.9-A resolution. *Proc Natl Acad Sci U S A* **94**, 6652-7 (1997).
120. Lohman, T. M. & Ferrari, M. E. Escherichia coli single-stranded DNA-binding protein: multiple DNA-binding modes and cooperativities. *Annu Rev Biochem* **63**, 527-70 (1994).
121. Roy, R., Kozlov, A. G., Lohman, T. M. & Ha, T. Dynamic structural rearrangements between DNA binding modes of E. coli SSB protein. *J Mol Biol* **369**, 1244-57 (2007).
122. Griffith, J. D., Harris, L. D. & Register, J., 3rd. Visualization of SSB-ssDNA complexes active in the assembly of stable RecA-DNA filaments. *Cold Spring Harb Symp Quant Biol* **49**, 553-9 (1984).
123. Reyes-Lamothe, R., Sherratt, D. J. & Leake, M. C. Stoichiometry and Architecture of Active DNA Replication Machinery in Escherichia coli. *Science* **328**, 498-501 (2010).
124. Roy, R., Kozlov, A. G., Lohman, T. M. & Ha, T. SSB protein diffusion on single-stranded DNA stimulates RecA filament formation. *Nature* **461**, 1092-7 (2009).
125. Murphy, M. C., Rasnik, I., Cheng, W., Lohman, T. M. & Ha, T. Probing single-stranded DNA conformational flexibility using fluorescence spectroscopy. *Biophys J* **86**, 2530-7 (2004).
126. Ha, T. et al. Initiation and re-initiation of DNA unwinding by the Escherichia coli Rep helicase. *Nature* **419**, 638-41 (2002).

127. Bustamante, C., Smith, S. B., Liphardt, J. & Smith, D. Single-molecule studies of DNA mechanics. *Curr Opin Struct Biol* **10**, 279-85 (2000).
128. Kulic, I. M. & Schiessel, H. Nucleosome repositioning via loop formation. *Biophys J* **84**, 3197-211 (2003).
129. Polach, K. J. & Widom, J. Mechanism of protein access to specific DNA sequences in chromatin: a dynamic equilibrium model for gene regulation. *J Mol Biol* **254**, 130-49 (1995).
130. Ha, T. & Xu, J. Photodestruction intermediates probed by an adjacent reporter molecule. *Phys Rev Lett* **90**, 223002 (2003).
131. Kozlov, A. G. & Lohman, T. M. Stopped-flow studies of the kinetics of single-stranded DNA binding and wrapping around the Escherichia coli SSB tetramer. *Biochemistry* **41**, 6032-44 (2002).
132. Dudko, O. K., Hummer, G. & Szabo, A. Intrinsic rates and activation free energies from single-molecule pulling experiments. *Phys Rev Lett* **96**, 108101 (2006).
133. Dudko, O. K., Hummer, G. & Szabo, A. Theory, analysis, and interpretation of single-molecule force spectroscopy experiments. *Proc Natl Acad Sci U S A* **105**, 15755-60 (2008).
134. Greenleaf, W. J., Frieda, K. L., Foster, D. A., Woodside, M. T. & Block, S. M. Direct observation of hierarchical folding in single riboswitch aptamers. *Science* **319**, 630-3 (2008).
135. Lohman, T. M., Green, J. M. & Beyer, R. S. Large-scale overproduction and rapid purification of the Escherichia coli ssb gene product. Expression of the ssb gene under lambda PL control. *Biochemistry* **25**, 21-5 (1986).
136. van Mameren, J. et al. Counting RAD51 proteins disassembling from nucleoprotein filaments under tension. *Nature* **457**, 745-8 (2009).
137. Gorman, J. & Greene, E. C. Visualizing one-dimensional diffusion of proteins along DNA. *Nat Struct Mol Biol* **15**, 768-74 (2008).
138. Romer, R., Schomburg, U., Krauss, G. & Maass, G. Escherichia coli single-stranded DNA binding protein is mobile on DNA: 1H NMR study of its interaction with oligo- and polynucleotides. *Biochemistry* **23**, 6132-7 (1984).
139. Kuznetsov, S. V., Kozlov, A. G., Lohman, T. M. & Ansari, A. Microsecond dynamics of protein-DNA interactions: direct observation of the wrapping/unwrapping kinetics of single-stranded DNA around the E. coli SSB tetramer. *J Mol Biol* **359**, 55-65 (2006).
140. de Gennes, P. G. Reptation of a Polymer Chain in the Presence of Fixed Obstacles. *The Journal of Chemical Physics* **55**, 572-579 (1971).
141. Perkins, T. T., Smith, D. E. & Chu, S. Direct observation of tube-like motion of a single polymer chain. *Science* **264**, 819-22 (1994).
142. Sukhishvili, S. A. et al. Materials science. Diffusion of a polymer 'pancake'. *Nature* **406**, 146 (2000).
143. Schiessel, H., Widom, J., Bruinsma, R. F. & Gelbart, W. M. Polymer reptation and nucleosome repositioning. *Phys Rev Lett* **86**, 4414-7 (2001).
144. Kantake, N., Madiraju, M. V., Sugiyama, T. & Kowalczykowski, S. C. Escherichia coli RecO protein anneals ssDNA complexed with its cognate

ssDNA-binding protein: A common step in genetic recombination. *Proc Natl Acad Sci U S A* **99**, 15327-32 (2002).

145. Umezu, K. & Kolodner, R. D. Protein interactions in genetic recombination in Escherichia coli. Interactions involving RecO and RecR overcome the inhibition of RecA by single-stranded DNA-binding protein. *J Biol Chem* **269**, 30005-13 (1994).

146. Cox, M. M. Regulation of bacterial RecA protein function. *Crit Rev Biochem Mol Biol* **42**, 41-63 (2007).

147. Sakai, A. & Cox, M. M. RecFOR and RecOR as distinct RecA loading pathways. *J Biol Chem* **284**, 3264-72 (2009).

148. Manfredi, C., Carrasco, B., Ayora, S. & Alonso, J. C. Bacillus subtilis RecO nucleates RecA onto SsbA-coated single-stranded DNA. *J Biol Chem* **283**, 24837-47 (2008).

149. Hobbs, M. D., Sakai, A. & Cox, M. M. SSB protein limits RecOR binding onto single-stranded DNA. *J Biol Chem* **282**, 11058-67 (2007).

150. Ryzhikov, M., Koroleva, O., Postnov, D., Tran, A. & Korolev, S. Mechanism of RecO recruitment to DNA by single-stranded DNA binding protein. *Nucleic Acids Research* (2011).

151. Luisi-DeLuca, C. & Kolodner, R. Purification and characterization of the Escherichia coli RecO protein. Renaturation of complementary single-stranded DNA molecules catalyzed by the RecO protein. *J Mol Biol* **236**, 124-38 (1994).

152. Kozlov, A. G., Cox, M. M. & Lohman, T. M. Regulation of Single-stranded DNA Binding by the C Termini of Escherichia coli Single-stranded DNA-binding (SSB) Protein. *Journal of Biological Chemistry* **285**, 17246-17252 (2010).

153. Lohman, T. M. Kinetics and mechanism of dissociation of cooperatively bound T4 gene 32 protein-single-stranded nucleic acid complexes. 1. Irreversible dissociation induced by sodium chloride concentration jumps. *Biochemistry* **23**, 4656-65 (1984).

154. Chrysogelos, S. & Griffith, J. Escherichia coli single-strand binding protein organizes single-stranded DNA in nucleosome-like units. *Proc Natl Acad Sci U S A* **79**, 5803-7 (1982).

155. Luger, K., Mader, A. W., Richmond, R. K., Sargent, D. F. & Richmond, T. J. Crystal structure of the nucleosome core particle at 2.8 A resolution. *Nature* **389**, 251-60 (1997).

156. Beard, P. Mobility of histones on the chromosome of simian virus 40. *Cell* **15**, 955-67 (1978).

157. Ranjith, P., Yan, J. & Marko, J. F. Nucleosome hopping and sliding kinetics determined from dynamics of single chromatin fibers in Xenopus egg extracts. *Proc Natl Acad Sci U S A* **104**, 13649-54 (2007).

158. Mihardja, S., Spakowitz, A. J., Zhang, Y. & Bustamante, C. Effect of force on mononucleosomal dynamics. *Proc Natl Acad Sci U S A* **103**, 15871-6 (2006).

159. Brower-Toland, B. D. et al. Mechanical disruption of individual nucleosomes reveals a reversible multistage release of DNA. *Proc Natl Acad Sci U S A* **99**, 1960-5 (2002).

160. Li, G., Levitus, M., Bustamante, C. & Widom, J. Rapid spontaneous accessibility of nucleosomal DNA. *Nat Struct Mol Biol* **12**, 46-53 (2005).

161. Hodges, C., Bintu, L., Lubkowska, L., Kashlev, M. & Bustamante, C. Nucleosomal fluctuations govern the transcription dynamics of RNA polymerase II. *Science* **325**, 626-8 (2009).

162. Kulic, I. M. & Schiessel, H. Chromatin dynamics: nucleosomes go mobile through twist defects. *Phys Rev Lett* **91**, 148103 (2003).

163. Makharashvili, N., Koroleva, O., Bera, S., Grandgenett, D. P. & Korolev, S. A novel structure of DNA repair protein RecO from Deinococcus radiodurans. *Structure* **12**, 1881-9 (2004).

164. Makharashvili, N., Mi, T., Koroleva, O. & Korolev, S. RecR-mediated modulation of RecF dimer specificity for single- and double-stranded DNA. *J Biol Chem* **284**, 1425-34 (2009).

165. Kumaran, S., Kozlov, A. G. & Lohman, T. M. Saccharomyces cerevisiae replication protein A binds to single-stranded DNA in multiple salt-dependent modes. *Biochemistry* **45**, 11958-73 (2006).

166. Kozlov, A. G., Jezewska, M. J., Bujalowski, W. & Lohman, T. M. Binding Specificity of Escherichia coil Single-Stranded DNA Binding Protein for the chi Subunit of DNA pol III Holoenzyme and PriA Helicase. *Biochemistry* **49**, 3555-3566 (2010).

167. Kim, H. D. et al. Mg2+-dependent conformational change of RNA studied by fluorescence correlation and FRET on immobilized single molecules. *Proc Natl Acad Sci U S A* **99**, 4284-9 (2002).

168. Joo, C., McKinney, S. A., Lilley, D. M. & Ha, T. Exploring rare conformational species and ionic effects in DNA Holliday junctions using single-molecule spectroscopy. *J Mol Biol* **341**, 739-51 (2004).

169. Chase, J. W. & Williams, K. R. Single-stranded DNA binding proteins required for DNA replication. *Annu Rev Biochem* **55**, 103-36 (1986).

170. Liu, Y. & West, S. C. Happy Hollidays: 40th anniversary of the Holliday junction. *Nat Rev Mol Cell Biol* **5**, 937-44 (2004).

171. Duckett, D. R. et al. The structure of the Holliday junction, and its resolution. *Cell* **55**, 79-89 (1988).

172. Lilley, D. M. J. Structure of helical junctions in nucleic acids. *Quarterly Reviews of Biophysics* **33**, 109-159 (2000).

173. Eichman, B. F., Vargason, J. M., Mooers, B. H. M. & Ho, P. S. The Holliday junction in an inverted repeat DNA sequence: Sequence effects on the structure of four-way junctions. *Proceedings of the National Academy of Sciences of the United States of America* **97**, 3971-3976 (2000).

174. McKinney, S. A., Declais, A. C., Lilley, D. M. & Ha, T. Structural dynamics of individual Holliday junctions. *Nat Struct Biol* **10**, 93-7 (2003).

175. McKinney, S. A., Freeman, A. D., Lilley, D. M. & Ha, T. Observing spontaneous branch migration of Holliday junctions one step at a time. *Proc Natl Acad Sci U S A* **102**, 5715-20 (2005).

176. Grainger, R. J., Murchie, A. I. H. & Lilley, D. M. J. Exchange Between Stacking Conformers in a Four-Way DNA Junction. *Biochemistry* **37**, 23-32 (1998).

177. Stryer, L. & Haugland, R. P. Energy transfer: a spectroscopic ruler. *Proc. Natl. Acad. Sci., USA* **58**, 719-726 (1967).

178. Ha, T. et al. Probing the interaction between two single molecules - fluorescence resonance energy transfer between a single donor and a single acceptor. *Proceedings of the National Academy of Sciences of the United States of America* **93**, 6264-6268 (1996).
179. Ha, T. Single molecule fluorescence resonance energy transfer. *Methods* **25**, 78 (2001).
180. Ashkin, A., Dziedzic, J. M., Bjorkholm, J. E. & Chu, S. Observation of a single-beam gradient force optical trap for dielectric particles. *Optics Letters* **11**, 288-290 (1986).
181. Kapanidis, A. N. et al. Initial transcription by RNA polymerase proceeds through a DNA-scrunching mechanism. *Science* **314**, 1144-7 (2006).
182. Blanchard, S. C., Gonzalez, R. L., Kim, H. D., Chu, S. & Puglisi, J. D. tRNA selection and kinetic proofreading in translation. *Nat Struct Mol Biol* **11**, 1008-14 (2004).
183. Lang, M. J., Fordyce, P. M. & Block, S. M. Combined optical trapping and single-molecule fluorescence. *Journal of Biology* **2**, 6 (2003).
184. Tarsa, P. B. et al. Detecting force-induced molecular transitions with fluorescence resonant energy transfer. *Angew Chem Int Ed Engl* **46**, 1999-2001 (2007).
185. Liphardt, J., Onoa, B., Smith, S. B., Tinoco, I. & Bustamante, C. Reversible unfolding of single RNA molecules by mechanical force. *Science* **292**, 733-737 (2001).
186. Woodside, M. T. et al. Direct measurement of the full, sequence-dependent folding landscape of a nucleic acid. *Science* **314**, 1001-4 (2006).
187. Meiners, J. C. & Quake, S. R. Femtonewton force spectroscopy of single extended DNA molecules. *Physical Review Letters* **84**, 5014-5017 (2000).
188. Rasnik, I., McKinney, S. A. & Ha, T. Nonblinking and long-lasting single-molecule fluorescence imaging. *Nat Methods* **3**, 891-3 (2006).
189. McKinney, S. A., Joo, C. & Ha, T. Analysis of Single-Molecule FRET Trajectories Using Hidden Markov Modeling. *Biophys J* **91**, 1941-51 (2006).
190. Bustamante, C., Marko, J. F., Siggia, E. D. & Smith, S. Entropic Elasticity of Lambda-Phage DNA. *Science* **265**, 1599-1600 (1994).
191. Yu, J., Ha, T. & Schulten, K. Conformational model of the Holliday junction transition deduced from molecular dynamics simulations. *Nucleic Acids Res* **32**, 6683-95 (2004).
192. Van Duyne, G. D. A structural view of cre-loxp site-specific recombination. *Annu Rev Biophys Biomol Struct* **30**, 87-104 (2001).
193. Peterman, E. J., Gittes, F. & Schmidt, C. F. Laser-induced heating in optical traps. *Biophys J* **84**, 1308-16 (2003).
194. McKinney, S. A., Declais, A. C., Lilley, D. M. J. & Ha, T. Structural dynamics of individual Holliday junctions. *Nature Structural Biology* **10**, 93-97 (2003).
195. Joo, C., McKinney, S. A., Lilley, D. M. J. & Ha, T. Exploring rare conformational species and ionic effects in DNA holliday junctions using single-molecule spectroscopy. *J Mol Biol* **341**, 739-751 (2004).
196. Ha, T. et al. Initiation and reinitiation of DNA unwinding by the Escherichia coli Rep helicase. *Nature* **419**, 638-641 (2002).

197. Ishijima, A. et al. Simultaneous Observation of Individual ATPase and Mechanical Events By a Single Myosin Molecule During Interaction With Actin. *Cell* **92**, 161-171 (1998).
198. Shroff, H. et al. Biocompatible force sensor with optical readout and dimensions of 6 nm3. *Nano Lett* **5**, 1509-14 (2005).
199. Gore, J. et al. Mechanochemical analysis of DNA gyrase using rotor bead tracking. *Nature* **439**, 100-4 (2006).
200. Lee, J. B. et al. DNA primase acts as a molecular brake in DNA replication. *Nature* **439**, 621-4 (2006).
201. Idiris, A., Alam, M. T. & Ikai, A. Spring mechanics of alpha-helical polypeptide. *Protein Eng* **13**, 763-70 (2000).
202. Afrin, R., Takahashi, I., Shiga, K. & Ikai, A. Tensile mechanics of alanine-based helical polypeptide: force spectroscopy versus computer simulations. *Biophys J* **96**, 1105-14 (2009).
203. Lantz, M. A. et al. Stretching the alpha-helix: a direct measure of the hydrogen-bond energy of a single-peptide molecule. *Chemical Physics Letters* **315**, 61-68 (1999).
204. Kageshima, M. et al. Insight into conformational changes of a single alpha-helix peptide molecule through stiffness measurements. *Chemical Physics Letters* **343**, 77-82 (2001).
205. Brinkley, M. A Brief Survey of Methods for Preparing Protein Conjugates with Dyes, Haptens, and Cross-Linking Reagents. *Bioconjugate Chemistry* **3**, 2-13 (1992).
206. Cecconi, C., Shank, E. A., Marqusee, S. & Bustamante, C. DNA molecular handles for single-molecule protein-folding studies by optical tweezers. *Methods Mol Biol* **749**, 255-71.
207. Jaalouk, D. E. & Lammerding, J. Mechanotransduction gone awry. *Nat Rev Mol Cell Biol* **10**, 63-73 (2009).
208. Smith, A.-S. Physics challenged by cells. *Nat Phys* **6**, 726-729 (2010).
209. Engler, A. J., Sen, S., Sweeney, H. L. & Discher, D. E. Matrix Elasticity Directs Stem Cell Lineage Specification. *Cell* **126**, 677-689 (2006).
210. Becker, N. et al. Molecular nanosprings in spider capture-silk threads. *Nat Mater* **2**, 278-83 (2003).
211. Gadella Jr, T. W. J., Jovin, T. M. & Clegg, R. M. Fluorescence lifetime imaging microscopy (FLIM): Spatial resolution of microstructures on the nanosecond time scale. *Biophysical Chemistry* **48**, 221-239 (1993).
212. Evers, T. H., van Dongen, E. M., Faesen, A. C., Meijer, E. W. & Merkx, M. Quantitative understanding of the energy transfer between fluorescent proteins connected via flexible peptide linkers. *Biochemistry* **45**, 13183-92 (2006).
213. Lamboy, J. A., Kim, H., Lee, K. S., Ha, T. & Komives, E. A. Visualization of the nanospring dynamics of the IkappaBalpha ankyrin repeat domain in real time. *Proc Natl Acad Sci U S A* **108**, 10178-83 (2011).
214. Ferreiro, D. U. et al. Stabilizing IkappaBalpha by "consensus" design. *J Mol Biol* **365**, 1201-16 (2007).
215. Lee, G. et al. Nanospring behaviour of ankyrin repeats. *Nature* **440**, 246-9 (2006).

216. Li, L., Wetzel, S., Pluckthun, A. & Fernandez, J. M. Stepwise unfolding of ankyrin repeats in a single protein revealed by atomic force microscopy. *Biophys J* **90**, L30-2 (2006).

217. Seelig, J. et al. Nanoparticle-induced fluorescence lifetime modification as nanoscopic ruler: Demonstration at the single molecule level. *Nano Letters* **7**, 685-689 (2007).

218. Doose, S., Neuweiler, H. & Sauer, M. Fluorescence quenching by photoinduced electron transfer: a reporter for conformational dynamics of macromolecules. *Chemphyschem* **10**, 1389-98 (2009).

219. Michalet, X., Weiss, S. & Jager, M. Single-molecule fluorescence studies of protein folding and conformational dynamics. *Chem Rev* **106**, 1785-813 (2006).

220. Yang, H. et al. Protein conformational dynamics probed by single-molecule electron transfer. *Science* **302**, 262-6 (2003).

221. Zhu, P., Clamme, J. P. & Deniz, A. A. Fluorescence quenching by TEMPO: a sub-30 A single-molecule ruler. *Biophys J* **89**, L37-9 (2005).

222. Chattopadhyay, K., Elson, E. L. & Frieden, C. The kinetics of conformational fluctuations in an unfolded protein measured by fluorescence methods. *Proc Natl Acad Sci U S A* **102**, 2385-9 (2005).

223. Doose, S., Neuweiler, H., Barsch, H. & Sauer, M. Probing polyproline structure and dynamics by photoinduced electron transfer provides evidence for deviations from a regular polyproline type II helix. *Proc Natl Acad Sci U S A* **104**, 17400-5 (2007).

224. Neuweiler, H., Doose, S. & Sauer, M. A microscopic view of miniprotein folding: enhanced folding efficiency through formation of an intermediate. *Proc Natl Acad Sci U S A* **102**, 16650-5 (2005).

225. Meller, A. & Di Fiori, N. The Effect of Dye-Dye Interactions on the Spatial Resolution of Single-Molecule FRET Measurements in Nucleic Acids. *Biophysical Journal* **98**, 2265-2272 (2010).

226. Hwang, H., Kim, H. & Myong, S. Protein induced fluorescence enhancement as a single molecule assay with short distance sensitivity. *Proc Natl Acad Sci U S A* **108**, 7414-8 (2011).

227. Kunzelmann, S. & Webb, M. R. A Fluorescent, Reagentless Biosensor for ADP Based on Tetramethylrhodamine-Labeled ParM. *Acs Chemical Biology* **5**, 415-425 (2010).

228. Packard, B. Z., Toptygin, D. D., Komoriya, A. & Brand, L. Profluorescent protease substrates: intramolecular dimers described by the exciton model. *Proc Natl Acad Sci U S A* **93**, 11640-5 (1996).

229. Blackman, M. J. et al. Structural and biochemical characterization of a fluorogenic rhodamine-labeled malarial protease substrate. *Biochemistry* **41**, 12244-12252 (2002).

230. Okoh, M. P., Hunter, J. L., Corrie, J. E. T. & Webb, M. R. A biosensor for inorganic phosphate using a rhodamine-labeled phosphate binding protein. *Biochemistry* **45**, 14764-14771 (2006).

231. Hamman, B. D. et al. Tetramethylrhodamine dimer formation as a spectroscopic probe of the conformation of Escherichia coli ribosomal protein L7/L12 dimers. *Journal of Biological Chemistry* **271**, 7568-7573 (1996).

232. Bernacchi, S. & Mely, Y. Exciton interaction in molecular beacons: a sensitive sensor for short range modifications of the nucleic acid structure. *Nucleic Acids Res* **29**, E62-2 (2001).

233. Rosenfeld, S. S., Xing, J., Jefferson, G. M., Cheung, H. C. & King, P. H. Measuring kinesin's first step. *Journal of Biological Chemistry* **277**, 36731-36739 (2002).

234. Toprak, E., Yildiz, A., Hoffman, M. T., Rosenfeld, S. S. & Selvin, P. R. Why kinesin is so processive. *Proceedings of the National Academy of Sciences of the United States of America* **106**, 12717-12722 (2009).

235. Zhuang, X. et al. Fluorescence quenching: A tool for single-molecule protein-folding study. *Proc Natl Acad Sci U S A* **97**, 14241-4 (2000).

236. Kellermayer, M. S. Z., Grama, L. & Somogyi, B. Global configuration of single titin molecules observed through chain-associated rhodamine dimers. *Proc Natl Acad Sci U S A* **98**, 14362-14367 (2001).

237. van den Ent, F., Moller-Jensen, J., Amos, L. A., Gerdes, K. & Lowe, J. F-actin-like filaments formed by plasmid segregation protein ParM. *Embo Journal* **21**, 6935-6943 (2002).

238. Jain, A. et al. Probing cellular protein complexes using single-molecule pull-down. *Nature* **473**, 484-U322 (2011).

239. Rasnik, I., McKinney, S. A. & Ha, T. Nonblinking and longlasting single-molecule fluorescence imaging. *Nature Methods* **3**, 891-893 (2006).

240. Zhuang, X. Single-molecule RNA science. *Annu Rev Biophys Biomol Struct* **34**, 399-414 (2005).

241. Ha, T. Structural dynamics and processing of nucleic acids revealed by single-molecule spectroscopy. *Biochemistry* **43**, 4055-63 (2004).

242. Herbert, K. M., Greenleaf, W. J. & Block, S. M. Single-molecule studies of RNA polymerase: motoring along. *Annu Rev Biochem* **77**, 149-76 (2008).

243. Ajtai, K. et al. Stereospecific reaction of muscle fiber proteins with the 5' or 6' isomer of (iodoacetamido)tetramethylrhodamine. *Biochemistry* **31**, 12431-40 (1992).

244. McKinney, S. A., Declais, A. C., Lilley, D. M. J. & Ha, T. Structural dynamics of individual Holliday junctions. *Nature Structural Biology* **10**, 93-97 (2003).

245. Lee, J. Y., Okumus, B., Kim, D. S. & Ha, T. J. Extreme conformational diversity in human telomeric DNA. *Proceedings of the National Academy of Sciences of the United States of America* **102**, 18938-18943 (2005).

246. Jena, P. V. et al. G-Quadruplex DNA Bound by a Synthetic Ligand is Highly Dynamic. *Journal of the American Chemical Society* **131**, 12522-12523 (2009).

247. Hadden, J. M., Convery, M. A., Declais, A. C., Lilley, D. M. & Phillips, S. E. Crystal structure of the Holliday junction resolving enzyme T7 endonuclease I. *Nat Struct Biol* **8**, 62-7 (2001).

248. Lilley, D. M. & White, M. F. The junction-resolving enzymes. *Nat Rev Mol Cell Biol* **2**, 433-43 (2001).

249. Hadden, J. M., Declais, A. C., Carr, S. B., Lilley, D. M. & Phillips, S. E. The structural basis of Holliday junction resolution by T7 endonuclease I. *Nature* **449**, 621-4 (2007).

250. Hadden, J. M., Declais, A. C., Phillips, S. E. & Lilley, D. M. Metal ions bound at the active site of the junction-resolving enzyme T7 endonuclease I. *EMBO J* **21**, 3505-15 (2002).
251. Declais, A. C. et al. The complex between a four-way DNA junction and T7 endonuclease I. *EMBO J* **22**, 1398-409 (2003).
252. Guan, C. & Kumar, S. A single catalytic domain of the junction-resolving enzyme T7 endonuclease I is a non-specific nicking endonuclease. *Nucleic Acids Res* **33**, 6225-34 (2005).
253. Karymov, M., Daniel, D., Sankey, O. F. & Lyubchenko, Y. L. Holliday junction dynamics and branch migration: single-molecule analysis. *Proc Natl Acad Sci U S A* **102**, 8186-91 (2005).
254. Amit, R., Gileadi, O. & Stavans, J. Direct observation of RuvAB-catalyzed branch migration of single Holliday junctions. *Proc Natl Acad Sci U S A* **101**, 11605-10 (2004).
255. Norman, D. G., Grainger, R. J., Uhrin, D. & Lilley, D. M. Location of cyanine-3 on double-stranded DNA: importance for fluorescence resonance energy transfer studies. *Biochemistry* **39**, 6317-24 (2000).
256. Iqbal, A., Wang, L., Thompson, K. C., Lilley, D. M. & Norman, D. G. The structure of cyanine 5 terminally attached to double-stranded DNA: implications for FRET studies. *Biochemistry* **47**, 7857-62 (2008).
257. Ouellet, J., Schorr, S., Iqbal, A., Wilson, T. J. & Lilley, D. M. Orientation of cyanine fluorophores terminally attached to DNA via long, flexible tethers. *Biophys J* **101**, 1148-54 (2011).
258. Ha, T., Enderle, T., Chemla, S., Selvin, R. & Weiss, S. Single Molecule Dynamics Studied by Polarization Modulation. *Phys Rev Lett* **77**, 3979-3982 (1996).